Quantitative analysis of atomic displacements in iron/iron oxide core-shell nanoparticles and their effect on high-resolution scanning transmission electron microscopy imaging

Shuayl Alotaibi

Doctor of Philosophy

University of York

School of Physics, Engineering and Technology

September 2023

Abstract

The main purpose of this project is to investigate the impact of atomic level displacement fields on the oxide shell of iron/iron oxide shell NPs (Fe@Fe_3O_4). This effect could play an important role for the reactivity of these NPs because their atomic structure is influenced by strain, which is essential for their applications in areas such as in biomedicines, environmental remediation, data storage or catalysis.

To systematically study this impact, finite element (FEM) simulations (COMSOL Multiphysics® programme) were utilized to obtain a realistic 3D displacement field which was then applied to 3D atomistic oxide shell models. Quantitative TEM/STEM simulations (QSTEM) were used to simulate the impact of such strain on image formation.

The results reveal that the strain has a significant effect on high-resolution scanning transmission electron microscopy (HRSTEM) imaging. The image intensities of Fe(II) atomic columns in the strained model show a reversal in the intensity distribution in comparison to the unstrained case. This is expressed by a decrease of column by column intensity variation from the core/shell interface towards the outer edge of the domain in the presence of strain whereas for the unstrained/relaxed case the column by column intensity from the core/shell interface towards the outer edge of the domain is increasing. The results also reveal that diffusion in the NPs depends on their size. For example, the displacement field mapping results reveal a relatively higher lattice strain in small (<20 nm) NPs which is distributed across the oxide lattice, inducing lattice diffusion, while for large NPs (>34 nm) strain is concentrated around the grain boundaries (GBs), which could be related to enhance GB diffusion.

Contents

1 Introduction and Background **26**

1.1 Introduction 26

1.1.1 Effect of strain on Z-contrast imaging 29

1.2 Using TEM for strain analysis 30

1.2.1 Strain analysis methods 31

1.3 Structure of iron oxide 35

1.4 Conclusion 36

2 Diffusion in Nanoparticles **37**

2.1 Introduction 37

2.2 Diffusion Mechanism 38

2.2.1 Lattice transport 38

2.2.2 Gorski effect 43

2.3 Grain Boundaries 44

2.3.1 Diffusion along the grain boundary 46

2.4 Oxidation of metal oxides 48

3 Experimental **54**

3.1 Introduction 54

3.2 Cluster source 54

3.3 Electron microscopy 56

3.3.1 Scanning transmission electron microscope 59
3.3.2 Image formation 62
3.3.3 Bright-field image and dark-field image 63
3.3.4 Annular dark-field (ADF) image 64
3.3.5 Thermal diffuse scattering 65

4 Methodology 66

4.1 Introduction 66
4.2 Experimental Z-contrast images 67
4.3 3D oxide shell model (truncated pyramid structure) 72
4.4 Finite element method (FEM) simulation 74
4.4.1 Condition for Displacement Field Model 77
4.4.2 Finite Element Simulations 80
4.4.3 Application of displacement field to the Fe_3O_4 structure 86
4.5 Simulation approach 89

5 Displacement field impact on the STEM images 92

5.1 Introduction 92
5.2 Results for Model I and II 93
5.2.1 Intensity profiles for Model I 93
5.2.2 Intensity profiles for Model II 99
5.3 Comparing simulated and experimental Z-contrast images 103
5.4 Displacement fields for Model I and II 108

6 Conclusion and future work 121

6.1 Conclusion 121
6.2 Future work 123

A Aberration-correction in STEM 124

B Elastic and inelastic electron scattering **127**

C Contrast mechanisms **131**

D Convolution of Functions ⊗ **138**

E Methodology appendix **139**

E.1 Characteristics of the experimental STEM images 139

E.2 3D oxide shell model (truncated pyramid structure) for Model I (15 nm) 142

E.3 Geometric Structure of Model I (15 nm) 143

F Image computing **145**

F.1 Image simulation 147

F.2 Image simulation method 148

F.3 Multi-slice method 148

G Image simulation results **152**

G.1 Model II 152

G.2 Model III 153

G.3 Model IV 154

H Intensity profile for Model III and Model IV **155**

H.1 Model III 155

H.2 Model IV 158

I Displacement filed mapping **161**

I.1 Model I 161

I.2 Model II 162

I.3 Model III 163

I.4 Model IV 165

List of Figures

1.1 Surface area of Fe NP increasing with decreasing NP diameter. NPs below 20 nm have large surface area. For cubic shape, density is 7.87 g/cm^3. 27

1.2 Schematic comparison of the structure of cubic (A), truncated (B), and spherical (C) metal/metal oxide NPs and the difference in grain boundary density and structure. The white dashed lines represent the grain boundaries. The number of grain boundaries depends on the size of the individual region and domain. 28

1.3 Fe_3O_4 atomic structure. Atomic positions - unstrained (A) and strained (B). Blue: Fe, Red: O. 30

1.4 Crystal structures of (A) haematite [1], (B) maghemite [2], (C) magnetite [3] and (D) Wustite [4]. Blue: Fe, Red: O. 35

2.1 Diagram shows the different diffusion mechanism types; (1) direct exchange mechanism, (2) ring mechanism, (3) vacancy mechanism, (4) interstitial mechanism, (5) interstitialcy mechanism and (6) crowdion mechanism [5]. 39

2.2 The vacancy mechanism. The red atoms are the ones with the potential to go to the vacant sites. There is a higher chance of a jump happening at these atoms than at others due to the surrounding vacancy and defect. Atoms that are potentially close to a defect are shown in red. Atoms with no defect are blue. 39

2.3 The interstitial mechanism. Number 3 represents the solute atom that might jump to 4. 1 and 2 are solvent atoms. 41

2.4 Schematic showing two planes separated by distanceλ. Number of atoms n_1 and n_2 are in each plane. Fluxes J_1 and J_2 of atoms moving between the two planes [6]. 41

2.5 Impact of lattice spacing λ on diffusivity D for the Fe-O system (using Eq. 2.14). 43

2.7 Schematic shows the type of the GBs. (A,B) are tilt and twist, respectively. (C) shows dislocation space D_s as in Eq. 2.19 [7, 8]. . . . 45

2.6 Schematic shows grain boundary axis for two grains (grain A and grain B) as x_A, y_A, z_A and x_B, y_B, z_B. **n** is norm of the grain boundary and **o** is rotation axis. θ is the rotation angle [9]. 45

2.8 The Fisher model. The notation shown in the figure is as follows: D_1,D_2 is the lattice diffusivity, D_{gb} is the diffusion in the grain boundary, and δ is the width of the grain boundary and d_y is the lateral grain boundary [7, 10]. 46

2.9 Initial stages of oxidation between the oxygen and metal, as in (A) and (B). An intermediate layer (grey region) forms between the oxygen and the metal forms subsequently (C). J: mass flux. Red: oxygen, blue: metal. 48

2.10 Plot [11] shows the potential energy of the metal ion at the end of the metal / oxide layer interface. S_1 and S_2 are the top of the potential barriers. Q_1 and Q_2 are interstitial positions. P is the position of the ion. W_i is the energy difference between the interstitial positions and the ion. U is extra activation energy for ion to overcome the top of the potential barriers. 50

2.11 Graph of estimated growth rate of iron oxide. Calculated using Eq.2.28 51

3.1 Cluster source components. The first component is the aggregation chamber. The second part is the quadrupole mass filter. The third part is the deposition chamber. Figure adapted from [12]. 55

3.2 (A) representing the TEM, red representing the DF scattered electron. The purple line is representing the BF scattered electron.(B) representing STEM, green line shows the ADF detectors at β angle. The purple line is representing the BF detectors at θ angle [13]. . . . 57

3.3 Summary of the electron beam detected by STEM. If the beam is scattered at low angle, the BF detector will detect the beam. However, if the electron beam is scattered at a high angle, it is a DF detector that will collect it. If the electron is scattered at a higher angle, the HAADF detector will detect the scattered electron. The angles in the simulation are 0–40 mard for BF detector, 90–200 & 110–180 mrad for HAADF detectors. 58

3.4 The instrument component of the STEM. When the transmitted beam scatter at small angle, BF detector will detect the electron beam as shown in black line. When the electron is scattered at high angle, the ADF detector will detect the electron as shown in red line [14]. 60

3.5 The diffraction of the beam when it is coherent. The discs overlap, leading to interference between the direct beam and scattered beam [14]. 63

3.6 (A)image is a bright-field STEM image of a Fe/Fe oxide core-shell structure, whereas the (B) image is a HAADF STEM image of a Fe/Fe oxide core-shell structure. 64

4.1 Workflow describing the procedure for the quantitative analyses of atomistic strain in iron/iron oxide core-shell NPs. Based on experimental images, which were evaluated with respect to the atomistic strain, a model geometry of a NP is generated and proposed strain fields applied to an atomistic model of the NP. Using QSTEM [15] Z-contrast images are then calculated for these structures and subsequent strain analyses performed and compared to the experimental data. 66

4.2 HAADF image C_s corrections of a cubic 15 nm core/shell Fe/Fe oxide nanoparticle with a 3 nm oxide shell. Voltage = 200 (kV), detector angle = 110-180 (mrad), dE = 0.8 (eV). 68

4.3 HAADF image C_s corrections 21 nm core/shell Fe/Fe oxide nanoparticle with a 3 nm oxide shell. Voltage = 100 (kV), detector angle = 90-200 (mrad), dE = 0.3 (eV). 68

4.4 HAADF image C_s corrections 27 nm core/shell Fe/Fe oxide nanoparticle with a 3 nm oxide shell. Voltage = 100 (kV), detector angle = 90-200 (mrad), dE = 0.3 (eV). 69

4.5 HAADF image C_s corrections 34 nm core/shell Fe/Fe oxide nanoparticle with a 3 nm oxide shell. Voltage = 100 (kV), detector angle = 90-200 (mrad), dE = 0.3 (eV). 69

4.6 An idealised representation of the components of an oxidised cubic iron/iron oxide NP: (A) exploded view, (B) assembled. Red: iron, blue: oxygen. 70

4.7 An oxide shell segment (region of interest) indicated for the 15 nm NP to be used for the strain simulation. 71

4.8 2D Schematic of the core base and oxide shell of the cubic NPs. . . . 71

4.9 Oxide shell segment chosen from the STEM image, as indicated in the red line in Fig. 4.7. 71

4.10 Truncation angles for the oxide segment model vs. the truncation length. 73

4.11 Oxide shell for the 15 nm oxide NP with a magnetite crystal structure. A relaxed (45°). 74

4.12 The oxide shell dimension. The triangle properties were used to calculate the model. 75

4.13 Schematic represents the cubic structure of four truncated pyramids. The schematic is a presentation of the oxide layers at $\theta = \beta = 45^o$. Figure produced from COMSOL Multiphysics® software. 75

4.14 (A) 45° geometric structure model. The angles are $\theta = 45^o$ and $\beta = 45^o$. The drawing depicts the core-shell structure of the oxide model. This demonstration displays four oxide shells.(B)non-45° case before applying external stress. The angles are $\theta = 47.49^o$ and $\beta = 42.51^o$. . . 76

4.15 A)The condition applied to the model. The described displacement condition was applied to the four facets. (B) The condition applied to the model. The conditions of the fixed condition applied to bottom facet. Figure produced from COMSOL Multiphysics® software. . . . 79

4.16 Screenshot from COMSOL Multiphysics® software showing the input parameter of equation 4.6. 79

4.17 The displacement profile shows how the model deforms at $\alpha = 4.78^o$. The colour bar shows the displacement needed for a 45° angle formation. The top length is 14.5 nm **before** the displacement and the thickness is 3 nm. 80

4.18 The displacement profile shows how the model deforms at $\alpha = 9.56^o$. The colour bar shows the displacement needed for 45° angle formation. The top length is 14 nm **before** the displacement and the thickness is 3 nm. 80

4.19 The displacement profile shows how the model deforms at $\alpha = 14.34^o$. The colour bar shows the displacement needed for 45° angle formation. The top length is 13.5 nm **before** the displacement and the thickness is 3 nm. 81

4.20 The displacement profile shows how the model deforms at $\alpha = 19.12^o$. The colour bar shows the displacement needed for 45° angle formation. The top length is 13 nm **before** the displacement and the thickness is 3 nm. 81

4.21 Line graph of the displacement magnitude (nm) of the model top facet. 81

4.22 The surface of continuum strain profile of the ZZ component (1). Differences in angle ($\beta = -\theta$) values between the model without displacement and the model with displacement. 83

4.23 The 2D surface plane cut from the centre of the 3D model. The image was produced using COMSOL Multiphysics® software. 83

4.24 (A) Strain tensor, ZZ component, of line profile as shown in Fig. 4.25A. (B)Strain tensor, ZZ component, of line profile as shown in Fig. 4.25B. Angles here is the $\theta = \beta$. 84

4.25 1D depiction of the 3D model's cut line in COMSOL Multiphysics ® software. (A) is from the top and the (B) is from the centre. 85

4.26 comparison of the 1D strain tensor of the ZZ component for 15 nm, model 21.5 nm, model 27 nm, and model 34 nm. 85

4.27 Angle before and after applying the displacement field: $\theta \approx 45^o$ and $\beta \approx 45^o$. Red: iron atoms, blue: oxygen atoms. 87

4.28 Model's angle before applying the displacement field: $\theta \approx 47.49^o$ and $\beta \approx 42.51^o$. Angle after applying the displacement field: $\theta \approx 45^o$ and $\beta \approx 45^o$. Red: iron atoms, blue: oxygen atoms. 87

4.29 Model's angle before applying the displacement field: $\theta \approx 50.19^o$ and $\beta \approx 39.81^o$. Angle after applying the displacement field: $\theta \approx 45^o$ and $\beta \approx 45^o$. Red: iron atoms, blue: oxygen atoms. 88

4.30 Model's angle before applying the displacement field: $\theta \approx 53.31^o$ and $\beta \approx 36.87^o$. Angle after applying the displacement field: $\theta \approx 45^o$ and $\beta \approx 45^o$.Red: iron atoms, blue: oxygen atoms. 88

4.31 Model's angle before applying the displacement field: $\theta \approx 56.31^o$ and $\beta \approx 33.69^o$. Angle after applying the displacement field: $\theta \approx 45^o$ and $\beta \approx 45^o$. Red: iron atoms, blue: oxygen atoms. 88

4.32 Multislice simulated Z-contrast images for model 15 nm of Fe_3O_4. Fe^{2+} columns correlate to high-intensity maxima, while Fe^{3+} columns correspond to low-intensity maxima.The angles diffidence are state in each image as $\beta = -\theta$. The 1st columns (A,B,C,D,E) are dark field (DF) images. The 2nd column (F,G,H,I,J) are false-colored of DF images. The 3rd column (K,L,M,N,O) are corresponding the bright field images (BF). 90

4.33 Plot depicts the angle differences (α and β as in Table 4.3) used to generate the model in relation to the displacement magnitude. 91

5.1 Multislice (QSTEM) simulated normalised Z-contrast images obtained for a truncated pyramid geometry of Fe_3O_4 for different. Fe^{2+} columns correlate to high- intensity maxima, while Fe^{3+} columns correspond to lower intensity maxima between the Fe^{2+} columns. (A) represents the unstrained case, (B) corresponds to a 0.5 nm edge displacement, (C) 1 nm, (D) 1.5 nm, and (E) 2 nm. Coloured arrows show the line profile positions. 94

5.2 Line profiles of simulations in Fig. 5.1 in y-axis direction. (A) shows the unstrained model, with (B-E) showing the results for the strained model. The truncation angle values for $\beta = -\theta$ are given in line with those provided in Fig. 4.33(see Chapter4). The black arrows point towards shoulders of the maxima. The dashed line indicates the peak positions according to the unstrained model. 95

5.3 Intensity profiles taken in the x-direction for Model I, as shown by the magenta, brown, purple, and green arrows in Fig. 5.1. The black dashed line indicates the peak positions according to the unstrained model. The zero angle is the non-displaced column. The angles difference are stated in each image in terms of $\beta = -\theta$. 97

5.4 (A) Model of the top segment of a cubic NPs' oxide shell with two selected columns at the top and bottom of the segment (Fe: blue, O: red). (B) Impact of the truncation angle on column intensities in the simulated images for the top and bottom column selected in (A). Insert shows schematic of the truncation angle impact on d_{trunc}. . . . 98

5.5 Multislice (QSTEM) simulated normalised Z-contrast images of Fe_3O_4 for Model II. Fe^{2+} columns correlate to high- intensity maxima, while Fe^{3+} columns correspond to low-intensity maxima. The angles difference are stated in each image as $\beta = -\theta$. (A) represents the unstrained case, (B) corresponds to a 0.5 nm edge displacement, (C) 1 nm, (D) 1.5 nm, and (E) 2 nm. Coloured arrows show the line profile positions. 99

5.6 Line profile taken in y-direction for Model II. (A) shows the result for the unstrained model, while B-E show the strained cases. The angle difference is stated in each plot as $\beta = -\theta$. Black arrows indicate shoulders on the maxima. The dashed lines mark the centre and position of the peripheral peaks for the unstrained case. 100

5.7 Intensity profiles in x-direction, as indicated in Fig. 5.5. The dashed lines mark the centre and position of the peripheral peaks for the unstrained case. The zero angle is the non-displaced column. The angles difference are stated in each image in terms of $\beta = -\theta$. 101

5.8 Comparison of line profiles in y-direction for Model I, Model II, Model III and Model IV for the unstrained and maximum strained cases. (A, B) unstrained and strained case for Model I. (C, D, E and F) unstrained and strained case for Model III and Model IV, respectively (Since the centre of the model shows only three maxima in intensity (as in Figs. H.2 and H.5), this line profile is 1 nm off-center because of the model's cutting angle). (G, H) unstrained and strained case for Model II. The results show a "reversal" of peak intensity distribution in both cases but more pronounced for the smaller domain (Model I). 102

5.9 (A) Normalised Cs-corrected HAADF image of a 15 nm cubic core/shell Fe/Fe oxide nanoparticle exhibiting a 3 nm-thick oxide shell. Blue circles represent columns near the core-shell boundary, while the red circles represent columns close to the surface of the oxide shell. (B,C) The images show the average of three columns, as indicated by the blue, red arrows close to the core shell and top oxide shell, respectively. (D)The line profiles of images of the average of three columns (B,C) in black and magenta plots. 104

5.10 (A) Cs-corrected HAADF images of a 21.5-nm-cubic core/shell Fe/Fe oxide nanoparticle exhibiting a 3 nm-thick oxide shell. The blue circles represent single columns that were determined to be closest to the core shell, while the red circles represent other columns close to the oxide shell. (B,C) The images show the average of three columns, as indicated by the blue and red arrows close to the core shell and top oxide shell, respectively. (D)The line profiles of images of the average of three columns (B,C) in black and magenta plots. 105

5.11 HAADF image of a 21.5 nm core/shell iron oxide nanoparticle exhibiting a 3 nm-thick oxide shell(A). The y-direction is indicated by the blue plot (B), and the x-direction by the red plot (C). The arrows in the HAADF image indicate the positions and directions of the line profile. 105

5.12 Comparison of the simulated and experimental image line profiles. (I, J) simulated images of (model 21.5 nm). I is the non-displaced model and J is the displaced model with edge displacement of 0.5 nm. (A, B, C, D) line profile in the x-direction for experimental image (as in blue plot in Fig. 5.11.) and simulated image (as in red arrows in I,J). (E,F,G,H) line profile in y-axis for experimental image (as in red plot in Fig. 5.11.) and simulated image (as in magenta arrows in I,J). . . 106

5.13 HAADF image of a cubic 21.5 nm core/shell Fe/Fe oxide nanoparticle with a 3 nm oxide shell. Two FFT images were selected, as represented by the green and red squares in the HADF image. The FFT images were filtered out to reduce the image noise by using the imfilter function native to MATLAB. The FFT image in the green square in HAADF image shows elongation vertical orientation peaks compared to the red square in HAADF image which could indicate present of the compression in the oxide shell. 107

5.14 Atomic distribution of Fe^{2+} atom positions for Model I. (A) 2D plot of Fe^{2+} atom positions (blue open circle), a reference point (the original point, filled blue circle), a base lattice vector in the R_1 (x)-direction (green arrow), and a base lattice vector in the R_2 (y)-direction (red arrow). (B, C) identify the neighbouring Fe^{2+} atom positions close to the reference point. (B) Fe^{2+} ions positions along the R_1 (x)-direction. (C) Fe^{2+} atom positions along the R_2 (y- direction). Some atoms near the right boundary, as in (B), and near the top boundary, as in (C), were not picked up because there are no neighbouring atoms along these boundaries. 109

5.15 Multislice simulated Z-contrast image for colour mapping image (A) of Model I. The Fe^{2+} columns correlate to high-intensity maxima, while the Fe^{3+} columns correspond to low-intensity maxima. (B) The Fe^{2+} atom positions (red dots) overlap the simulated image to identify the Fe^{2+} in the image. (C, D) displacement field mapping along the R_1 (along the x-axis) and R_2 direction (along the y-axis) based on the Fe^{2+} atom positions displayed in Fig. 5.14(B, C). 110

5.16 (A) 2D displacement mapping of model 15 nm in the R_1 direction along the x-axis. (B) strain profile in R_1 direction. Data were obtained from two-line profiles, as indicated by the arrows in the 2D displacement mapping. 111

5.17 (A) 2D displacement mapping of model 15 nm in the R_2 direction along the y-axis. (B) strain profile in R_2 direction as indicated by the black arrow in (A). (C) strain profile in R_2 direction as indicated by the magenta arrow in (A). 112

5.18 Line profile plot of model 15 nm(Model I). Two line profiles were determined for different displacement fields applied to the model, as shown in Table5.1. The displacement field mappings of the model at 2.5^o, 5°, and 8° angles are shown Fig. I.1.The directional orientation of the strain line profiles is denoted by the arrows depicted in Fig. 5.16A. (A) Data is obtained from line profile close to the edge as indicted by the solid black arrow in Fig. 5.16A. (B) Data obtained from profile at the centre of the model as indicated by the magenta arrow in Fig. 5.16A. 113

5.19 Line profile plot for model 15 nm. Two line profiles were conducted for different displacement fields applied to the model, as shown in Table5.1. The displacement field mappings for the model at angles of 2.5^o, 5° and 8° are shown in Fig. I.1. The directional orientation of the strain line profiles is indicated by the arrows depicted in Fig. 5.17. (A) Data obtained from line profile close to the edge as indicted by the solid black arrows in Fig. 5.17. (B) Data obtained from profile at the centre of the model as indicated by the magenta arrow in Fig. 5.17. 115

5.20 2D displacement mapping of model 34 nm in the R_1 direction along the x-axis. (B) strain profile in R_1 direction. Data were obtained from two-line profiles, as indicated by the arrows in the 2D displacement mapping. 116

5.21 (A)2D displacement mapping of model 34 nm in the R_2 direction along the y-axis. (B) strain profile in R_2 direction as indicated by the black arrow in (A). (C) strain profile in R_2 direction as indicated by the magenta arrow in (A). 117

5.22 Line profile plot of Model II. Two line profiles were determined for the different displacement fields applied to the model, as shown in Table5.2. (A) Data obtained from line profile close to the edge, as indicted by the solid black arrow in the displacement field mapping in R_1, as shown in Fig. 5.20A. (B) Data obtained from at the centre of the model, as indicated by the magenta arrow in the displacement field mapping in R_2, as seen in Fig. 5.21A. The directional orientation of the strain line profiles is indicated by the arrows. The displacement field mappings of the model at angles of 2.5^o, 5°, and 8° are shown in Fig. I.2.(Appendix I). 119

5.23 Comparing the strain profile in the R_1 direction in (A) and (B), and the R_2 direction in (C) and (D) for different-sized models. The comparison is made between the different-sized models for the 11° angle. The data obtained from the line profile close to the edge is indicted by the solid black arrow and magenta arrow in Fig. 5.16, 5.20A, I.3D, and I.5D, and the data obtained from line profile from taken from the left and right is indicted by the solid black arrow and magenta arrow in Figs.5.17, 5.21A,I.3H, and I.5H. 120

A.1 Schematic of electromagnetic lenses [16]. 124

A.2 Electron trajectory in an electromagnetic lens and a perfect lens. (A) Schematic of the corrected probe after adding an aberration corrector. (B) schematic of uncorrected probe[17, 18]. 125

B.1 Summary of elastic and inelastic electron signals resulting from an electron's interaction with matter in TEM. The elastic scattered at higher angle and inelastic scattered close angle to optical axis. 127

B.2 How the electron beam interacts with the nucleus in the electron cloud.128

B.3 Electron scattered impacted by the the detector angle. (A) BF detector angle for 0-40 mard and (B) ADF angle detector for 110-180 mrad and (C) ADF detector for 90-200 mrad. These angels are based on the instrument that was used to take the STEM images. Using Eq.(eq. B.2) to calculate the scattered electron vs. the angles. 130

C.1 The effects of different mass thicknesses in the specimen. On the left is bright-field imaging of a test sample of Au NPs on C. On the right is a diagram showing the mechanism for how the beam interacts in different mass thicknesses in the specimen [17]. 132

C.2 Plane waves which pass through the crystal will experience phase modulation[19]. 133

E.1 HAADF image of a core/shell Fe/Fe oxide nanoparticle. The top facet of the oxide shell is 21.5nm. The thickness of the oxide shell is 3 nm. 139

E.2 The oxide shell chosen from the STEM image, as indicated in the red line in the STEM image. 140

E.3 HAADF image of a core/shell Fe/Fe oxide nanoparticle. The top facet of the oxide shell is 27 nm. The thickness of the oxide shell is 3nm. 140

E.4 The oxide shell chosen from the STEM image, as indicated in the red line in the STEM image. 140

E.5 HAADF image of a core/shell Fe/Fe oxide nanoparticle. The top facet of the oxide shell is 34 nm. The thickness of the oxide shell is 3nm. 141

E.6 The oxide shell chosen from the STEM image, as indicated in the red line in the STEM image. 141

E.7 Oxide shell of Fe_3O_4. $\theta \approx 47.49$ and $\beta \approx 42.51$, and thickness is 3 nm. 142

E.8 Oxide shell of Fe_3O_4. $\theta \approx 50.19$ and $\beta \approx 39.81$, and thickness is 3 nm. 142

E.9 Oxide shell of Fe_3O_4. $\theta \approx 53.13$ and $\beta \approx 36.87$, and thickness is 3 nm. 142

E.10 Oxide shell of Fe_3O_4. $\theta \approx 56.31$ and $\beta \approx 33.69$, and thickness is 3 nm. 143

E.11 non- 45° case before applying external stress. The angles are $\theta = 50.19^o$ and $\beta = 39.81^o$. 143

E.12 non- 45° case before applying external stress. The angles are $\theta = 53.13^o$ and $\beta = 36.87^o$. 144

E.13 non- 45° case before applying external stress. The angles are $\theta = 56.31^o$ and $\beta = 33.69^o$. 144

F.1 HAADF image of a core/shell Fe/Fe oxide nanoparticle. 147

F.2 FFT of image in Fig. F.1. 147

F.3 The process of electron waves passing through a specimen (left) and sliced into many thin slices (right). 149

F.4 The process of the multi-slice method. $\psi_p$is the wave function transmitted (t) through the slice. 151

G.1 Multislice simulated Z-contrast images for model 34 nm of Fe_3O_4. Fe^{2+} columns correlate to high-intensity maxima, while Fe^{3+} columns correspond to low-intensity maxima.The angles diffidence are state in each image as $\beta = -\theta$. The 1st column(A,B,C,D,E) is dark field (DF) image. The 2nd column (F,G,H,I,J) is false-colored of DF image. The 3rd column (K,L,M,N,O)is the bright filed(BF). 152

G.2 Multislice simulated Z-contrast images for model 21.5 nm of Fe_3O_4. Fe^{2+} columns correlate to high-intensity maxima, while Fe^{3+} columns correspond to low-intensity maxima.The angles diffidence are state in each image as $\beta = -\theta$. The 1st column(A,B,C,D,E) is dark field (DF) image. The 2nd column (F,G,H,I,J) is false-colored of DF image. The 3rd column (K,L,M,N,O)is the bright filed(BF). 153

G.3 Multislice simulated Z-contrast images for model 27 nm of Fe_3O_4. Fe^{2+} columns correlate to high-intensity maxima, while Fe^{3+} columns correspond to low-intensity maxima.The angles diffidence are state in each image as $\beta = -\theta$. The 1st column(A,B,C,D,E) is dark field (DF) image. The 2nd column (F,G,H,I,J) is false-colored of DF image. The 3rd column (K,L,M,N,O)is the bright filed(BF). 154

H.1 Multislice simulated Z-contrast images of Fe_3O_4 for 21.5 nm model. Fe^{2+} columns correlate to high-intensity maxima, while Fe^{3+} columns correspond to low-intensity maxima. The angles diffidence are state in each image as $\beta = -\theta$. (A) is non-displaced, (B) = 0.5 nm displacement, (C) is 1 nm displacement, (D) is 1.5 nm displacement and (E) is 2 nm displacement. The arrows direction is representing the line profile direction. The image simulation is a colored mapping of the DF images. 155

H.2 Line profile taken in y-axis direction as in red arrow in Fig. H.1. (A) shows the non-displaced model, while the other four line profile (show displaced model as shown in Table 4.3 (see chapter 4). The angles diffidence are stated in each plot as $\beta = -\theta$ as in Fig. 4.33 (see chapter 4). The black arrows point towards the shoulders of the maxima. The dashed line separates the model without displacement from the model with displacement. 156

H.3 Four intensity profiles were taken in x-axis direction as shown in magenta, brown, purple and green arrows in Fig. H.1. The black dished line separate the non displaced column from displaced column. The zero angle is non-displaced column. The angles diffidence are state in each image as $\beta = -\theta$. 157

H.4 Multislice simulated Z-contrast images of Fe_3O_4 for 27 nm model. Fe^{2+} columns correlate to high-intensity maxima, while Fe^{3+} columns correspond to low-intensity maxima.The angles diffidence are state in each image as $\beta = -\theta$. (A) is non-displaced, (B) = 0.5 nm displacement, (C) is 1 nm displacement, (D) is 1.5 nm displacement and (E) is 2 nm displacement. The arrows direction is representing the line profile direction. The image simulation is a colored mapping of the DF images. 158

H.5 Line profile taken in y-axis direction as in red arrow in Fig. H.4. (A) shows the non-displaced model, while the other four line profile (show displaced model as shown in Table 4.3 (see chapter 4). The angles diffidence are state in each plot as $\beta = -\theta$ as in Fig. 4.33 (see chapter 4). The black arrows point towards the shoulders of the maxima. The dashed line separates the model without displacement from the model with displacement. 159

H.6 Four intensity profiles were taken in x-axis direction as shown in magenta, brown, purple and green arrows in Fig. H.4. The black dished line separate the non displaced column from displaced column. The zero angle is non-displaced column. The angles diffidence are state in each image as $\beta = -\theta$. 160

I.1 Displacement field mapping of model 15 nm. The displacement field mapping in R_1 direction is in (A,C,E,G) with 2.5^o, 5°, 8° and 11° angles, respectively. Displacement field in R_2 direction is in (B,D,F,H) with 2.5^o, 5°, 8° and 11° angles, respectively. 161

I.2 Displacement field mapping of model 34 nm. The displacement field mapping in R_1 direction is in (A,C,E,G) with 2.5^o, 5°, 8° and 11° angles, respectively. Displacement field in R_2 direction is in (B,D,F,H) with 2.5^o, 5°, 8° and 11° angles, respectively. 162

I.3 Displacement field mapping of model 21.5 nm. (A,C,E,G) with 2.5^o, 5°, 8° and 11° angles, respectively represent the displacement field mapping in R_1 direction. (B,D,F,H) with 2.5^o, 5°, 8° and 11° angles, respectively, display the displacement field in R_2 direction. 163

I.4 Line profile plot of model 21.5 nm. Two line profiles were conducted for different displacement field values applied to the model, as shown in Table I.1. (A) and (B): Data obtained from a line profile close to the edge and centre, as indicated by the solid black arrows and magenta arrows, respectively in the displacement field mapping in R_1, as shown in Fig. I.3 (A,B,C,D). Data obtained from a line profile in the displacement field mapping in R_2 are in (C) and (D). (C) line profile from the left to the right as in the black arrows and (D) line profile from the centre as in magenta arrows as in Fig. I.3 (E,F,G,H). 164

I.5 Displacement field mapping of model 27 nm. (A,B,C,D) with 2.5^o, 5°, 8° and 11° angles, respectively represent the displacement field mapping in R_1 direction. (E,F,G,H) with 2.5^o, 5°, 8° and 11° angles, respectively, display the displacement field in R_2 direction. 165

I.6 Line profile plot of model 27 nm. Two line profiles were conducted for different displacement field values applied to the model, as shown in Table I.2. (A) and (B): Data obtained from a line profile close to the edge and centre, as indicated by the solid black arrows and magenta arrows, respectively in the displacement field mapping in R_1, as shown in Fig. I.5 (A,B,C,D). Data obtained from a line profile in the displacement field mapping in R_2 are in (C) and (D). (C) line profile from the left to the right as in the black arrows and (D) line profile from the centre as in magenta arrows as in Fig. I.5 (E,F,G,H). 166

List of Tables

1.1 General properties of four forms of iron oxide [20]. 36

4.1 Lattice parameters of Fe_3O_4 (magnetite) structure [21]. 72

4.2 shows the parameter used in the ''Nanocarver" code. 72

4.3 shows the parameter used for 15 nm model. 76

4.4 Model mechanical properties of Fe_3O_4 used in COMSOL Multiphysics® software. 77

4.5 Shows the parameters used for the 21.5 nm model. 85

4.6 Shows the parameters used for the 27 nm model. 86

4.7 Shows the parameters used for the 34 nm model. 86

4.8 simulation parameter used in QSTEM for the model of 15 nm. 89

4.9 simulation parameter used in QSTEM for models of 21.5 nm, 27nm and 34 nm size length. 89

5.1 Displacement fields and parameters used for Model I. 114

5.2 Displacement fields and parameters used for the 34 nm model. 117

I.1 displacement field and parameter used for 21.5 nm model. 163

I.2 displacement field and parameter used for 27 nm model. 165

Acknowledgements

The successful completion and finalisation of this research endeavour would be very challenging without the assistance and collaboration of numerous individuals. I would like to express my gratitude to Dr. Toby Bird and Dr. Sitki Aktas for their invaluable help and guidance. I express my gratitude to Dr. Demie Kepaptsoglou and Dr. Leonardo Lari for providing the experimental STEM images obtained at SuperSTEM and York Nanocentre, respectively.

I would like to express my gratitude to my supervisors, Dr. Andrew Pratt and Prof. Roland Kröger, for their valuable support and advice during the course of this research project. In particular, I am deeply grateful to Prof. Roland, since his assistance and direction were important in enabling me to successfully complete this project and present it in its final form.

I want to express my gratitude to the special individuals in my life, my wife (Asma), and my two daughters (Sara and Shaden). Thank you for your support.

To Asma, my wife.

To my daughters, Sara and Shaden.

To unborn baby.

Declaration

I declare that this project is based on research conducted at the University of York, England, School of Physics, Engineering, and Technology. This project has not been submitted to any other Universities, included this University for a degree or other qualification. All sources are acknowledged as References.

Acronyms

NPs nanoparticles

SGAS sputter-gas-aggregation sources

EM Electron microscopy

VLM visible light microscope

TEM transmission electron microscopy

CBED convergent-beam electron diffraction

STEM scanning transmission electron microscopy

GB grain boundary

TPs triple junctions

HR-TEM high-resolution transmission electron microscopy

HR-STEM high-resolution scanning transmission electron microscopy

HAADF high-angle annular dark field

CM Cabrera-Mott

DF dark field

BF bright field

FFT fast fourier transform

QSTEM quantitative TEM/STEM Simulations

FEM finite element simulation

GPA geometrical phase analysis

PP Peak Pairs

PF Peak Finding

TDS thermal diffuse scattering

Chapter 1

Introduction and Background

1.1 Introduction

Metal oxide nanoparticles (NPs) have attracted a huge amount of attention due to their applications in, for example, healthcare and the environment. In environmental remediation, metal oxide NPs act as sorbents and can target specific industrial contaminations that can then be magnetically separated [22]. In biomedical applications, iron oxide NPs can be used for targeted drug delivery in the human body or to treat cancer through metal nanoparticle hypothermia [23]. Many other applications exist, for example, data storage [24] and catalysis [25].

Nanoparticles (NPs) are materials that have very interesting and often dissimilar properties compared to their bulk equivalents in terms of their oxidation and diffusion mechanisms. This is because the NPs' reactivity differs very often from that of the bulk material. For example, NPs have a large number of their atoms and molecules effectively located on their surfaces (large surface area-to-volume ratio), which leaves unsaturated chemical bonds (dangling bonds), increasing the possibility of a high energy surface (a large surface energy resulting in an increased interaction with the environment, such as with oxygen in the air) [26]. Figure 1.1 shows the surface area (SA) of Fe versus the particle diameter for cubic particles. Equation 1.1 shows that the surface area dramatically decreases with increasing NP diameter. Hence, metal particles with diameters below 20 nm show increased reactivity with oxygen [27].

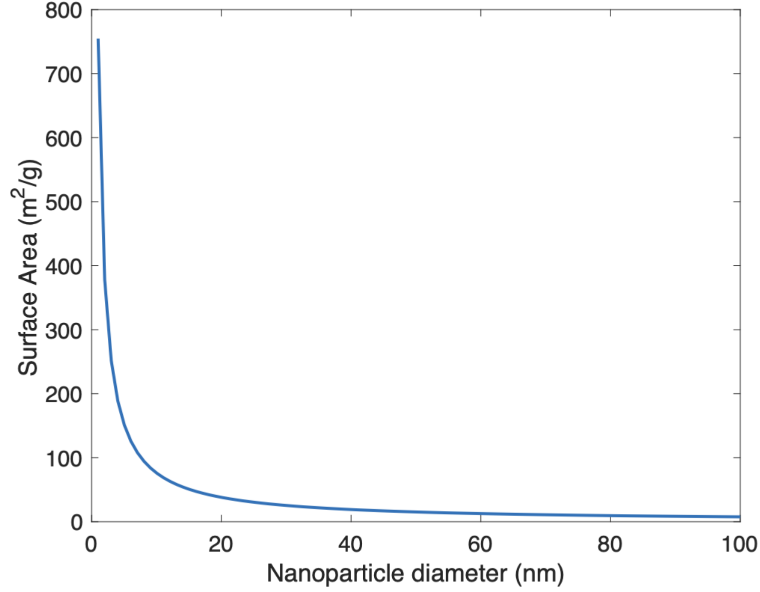

Fig. 1.1: Surface area of Fe NP increasing with decreasing NP diameter. NPs below 20 nm have large surface area. For cubic shape, density is 7.87 g/cm^3.

$$\text{SA} = \frac{6}{\text{sizes} \times \text{density}} \tag{1.1}$$

In addition to the size of the NPs, which influences the oxidation and diffusion mechanisms, the geometry of the NPs also plays a role in these processes. For example, cubic NPs' oxidation behaviour is different from that of truncated and spherical NPs [28]. This is due to the fact that ideal cubic NPs contain mostly monocrystalline side faces, as shown in Fig. 1.2. The diffusion in cubic NPs (oxidation rate) is slower than in other shapes, such as spherical, which have polycrystalline side faces [28]. Due to the different crystalline side faces in these geometries, the grain boundary and lattice diffusion have an effect on how these geometries behave during oxidation [28] (see Chapter 2). This has also been shown in ref.[29], the increased anisotropy of atomic order in strained magnetite is expected to affect the magnetic spin orientation. Hence, a better understanding of the impact of oxidation related stress on this local atomic order is important to determine the role of this stress for the magnetic properties[29].

In addition to their size, surface crystallographic defects, resulting in irregular surface atom arrangements, and the presence of vacancies, inducing lattice strain,

can also lead to unsaturated bonds and increased reactivity, whether the vacancies are located at grain boundaries or within the lattice domain [26]. Consequently, the strain present in the oxidation shell of NPs influences their oxidation. In a previous publication, it was demonstrated that the oxide shell reveals a large variety of strains associated with the oxide/oxide boundaries [30]. NPs typically show high reactivities, which tells us that their diffusion rates, as well as oxidation rates, can differ considerably from those of the same bulk material [30].

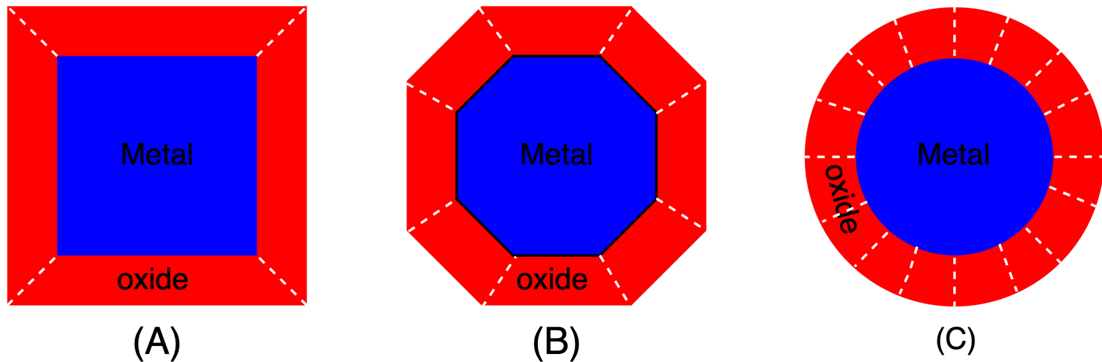

Fig. 1.2: Schematic comparison of the structure of cubic (A), truncated (B), and spherical (C) metal/metal oxide NPs and the difference in grain boundary density and structure. The white dashed lines represent the grain boundaries. The number of grain boundaries depends on the size of the individual region and domain.

Consequently, a quantification of strain helps us to understand the oxidation mechanism in metal oxide NPs and reveals whether lattice or grain boundary diffusion is dominant [30]. Therefore, knowledge of the impact of strain in nanoparticles on the contrast variations in high annular angular dark field (HAADF) images is required. This is because the HAADF image method provides detailed 2D information on atomic column positions and allows for a direct interpretation of image contrast in terms of variations in iron atom densities (oxygen scatters only weakly and hence its contribution can be neglected) in the beam direction [31]. This requires the development of realistic atomistic models for image simulations to acquire knowledge regarding the impact of strain in the oxide shell on the resulting HAADF image.

This project investigates the oxide shell of cubic iron-based magnetic NPs, which are produced by cluster-source deposition. This measurement will be carried out by

employing a custom MATLAB® [32] code to comprehend the influence of displacement on simulated STEM images and establish a systematic correlation between volumetric displacement and STEM image intensity. This can be accomplished by applying a realistic displacement field that is estimated using finite element simulation (COMSOL Multiphysics® program [33]) to a 3D atomistic oxide shell model, and the resulting model will be utilised to generate simulated STEM images using quantitative TEM/STEM Simulations (QSTEM) [15]. The outcome of these simulations will then be compared to data extracted from experimental images.

1.1.1 Effect of strain on Z-contrast imaging

Since the strain investigation is experimentally achieved by analysing Z-contrast images, it is important to understand the effect of the strain on image formation. Previous studies show that strain, caused by point or extended defects, has a significant impact on the contrast in Z-contrast images due to the dependence of the electron scattering on the local atomic arrangements [34, 35]. The simulation output of annular dark-field (ADF) images, for example, reveals contrast related to dislocation regions [36]. In addition, the impact of the cut-off angles of the HAADF has not been studied here but it can be expected that changing the detector setting will have an impact on the absolute signal related to Bragg and diffuse scattering. However, the overall dependence of e.g. column intensities and positions should not be significantly affected by the choice of detector [37, 38]. Another factor that influences the image contrast is the thickness of the sample. As the electron beam propagates within the crystal along the zone axis (for a crystal oriented with a given zone axis parallel to the beam), the angular distribution of the electrons exiting the sample is affected by the local arrangements of the atoms [37].

Apart from the intensity maxima positions related to the atomic column also their intensities are affected by the strain-related displacement of atoms [34, 37]. Figure 1.3 shows a schematic that shows how atomic positions are shifted due to the application of a strain-field. Figure1.3(A) represents the model with no displacement and Fig. 1.3(B) the same model after the application of external stress to the side facets.

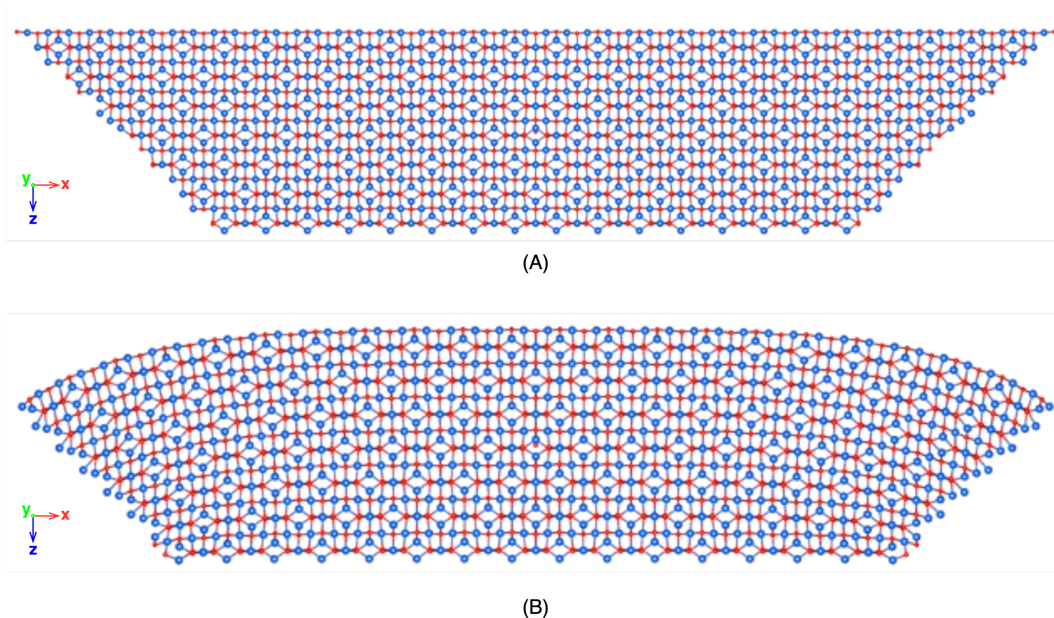

Fig. 1.3: Fe_3O_4 atomic structure. Atomic positions - unstrained (A) and strained (B). Blue: Fe, Red: O.

1.2 Using TEM for strain analysis

To better comprehend the strain associated with the image, it is necessary to describe the methods and context used to measure the strain in STEM images. Strain relates to a shift within a specimen upon the exertion of stress (force per area) with respect to a stress-free reference position [39]. Strain in a crystalline specimen often arises due to the specimen formation itself often leading to structural defects and/or deformation [31]. Strain measurements are important for many material composites, semiconducting devices and catalytic materials because deformation in these materials can affect their physical and mechanical properties. Mechanical properties in semiconductor devices, for example, can vary and affect the response to external forces and hence the deformation behaviour under tensile or compressive stress. This deformation can e.g. affect the associated band structure and hence the electronic properties [40] by e.g. a strain-induced overlap of the d band orbital which affect the electronic properties of surface metal of the NPs (e.g. Pd) [41]. Also, by manipulation of the electronic structure at the surface of the NPs, the catalytic performance of core-shell NPs can be altered by e.g. changing the thickness of the

NPs' shell. This change of the thickness can be influenced by the strain present in the nanocrystal [41]. Aside from this, metal/oxide NP strain measurements can help to understand whether the oxidation mechanism in the metal oxide NPs facilitates the oxide formation throughout the lattice or the grain boundaries, which can also affect the magnetic moment and hence susceptibility in the presence of an external magnetic field.

1.2.1 Strain analysis methods

There are a number of techniques that can be used to measure the strain in the crystals. For example, X-ray diffraction, Raman spectroscopy, and Transmission Electron Microscopy (TEM) can be used for this purpose. X-ray diffraction and Raman spectroscopy allow for strain measurement of about 1×10^{-5} and 1×10^{-4} respectively. However, these techniques are limited to spatial resolutions of ≈ 500 nm due to their wavelength limitation [42, 43] (See Eqs. 3.1 and 3.2 in Chapter 3 section 3.3). Measuring strain on materials with extensions below 500 nm is challenging, and atomic resolution cannot be achieved by these methods [44]. Therefore, techniques with this sort of resolution cannot be applied to nanoparticle (NP) materials if atomic resolution is required. On the other hand, TEM has the ability to image the atomic column positions in the specimen and hence to provide access to information on atomic level atomic displacements [42]. A more detailed discussion of the TEM image formation is presented in Chapter 3. However, an additional technique is required to obtain quantitative information from the image, such as lattice misfit, lattice parameter, and strain [45]. This restriction is caused by the fact that the contrast in the HRTEM image is not directly interpretable due to the peak not always representing the atomic column. For example, distortion effects, aberration effects, etc. could affect the maxima (peak) positions. However, the HAADF STEM image is a technique that can provide information about the chemical contrast in the image. Atomic number and strain will both affect the column intensities and column positions measured. In this context strain will affect the atomic arrangement within the individual columns and hence it is expected to significantly impact the column intensities in the Z-contrast images (More details about STEM images in Chapter 3) [31, 46]. Based on this limitation, peak finding and geometrical phase

analysis (GPA) can be introduced to overcome this issue.

Strain measurement from a HRTEM image can be achieved using two techniques. The first, real lattice, approach directly uses the maxima or peak positions in the image. The position of the atomic column is then measured using peak finding (PF) algorithm. The second approach is the analysis of lattice fringe spacing distribution in the Fourier space by by applying a filter (mask) around the Bragg spots in the fast Fourier Transformation (FFT). This technique is called geometrical phase analysis (GPA) [47]. The image contrast in TEM, in most cases, shows maxima and minima related to the positions of the atomic columns in the crystal. It is a function of thickness and defocus. Overall, the peak finding technique relies on TEM image contrast to measure the strain [48].

An early approach using the PF method was developed by Bierwolf [49] to study the strain in semiconductor materials. He filtered out the frequencies in the Fourier fast transform (FFT) image to cut off the high spatial frequencies that give rise to fine intensity. He then transferred the image back to real space [49]. Next, the obtained the column positions (position of maxima) using a patterning to obtain the contrast in the image. However, the filtering applied by Bierwolf was frequently far away from the central position of the maxima (e.g. due to noise), leading to large errors in the resulting strain fields [45, 49].

Another approach was introduced by Jouneau et al. [50] to overcome the error of defining the intensity maxima in the image, in which they performed the PF method without the use of any filtering. Instead they used the Fourier space filter in the image to determine the positions of the atomic columns, measured the intensity profile of the real image and then determined the centre of mass of the intensity. A reference domain was identified from a defect-free area in the image with respect to column spacing, which were then used to calculate the displacement. The disadvantage of this method is that it depends heavily on image resolution and noise [45, 50]. Seitz et al. [51] applied an algorithm to minimize the error associated with finding the centre of maximum intensity in the direct image. The first algorithm determined the intensity maxima because they wanted to create a pattering that would subsequently be used to determine the distance between the intensity maxima. The second algorithm calculated the spread between each maximum. This maximum

represents the image points or "atomic columns positions." Finally, noise quantification was achieved from an unstrained region to be used as a reference region [51]. This method's development mainly focused on identifying the intensity maxima in the image and then using these maxima to calculate the distance between the pixel positions in the image. Another method to determine the lattice site positions is the centre of mass [45]. This is achieved by defining the pixel position using a circle shape in the image and the intensity of the image divided by the sum of the image intensity [45]. However, the circle shape must be close to the real position of an atom in the image. Also, the radius of the circle plays a role in the calculation [45].

Another method proposed to calculate the maxima of the contrast in the image to calculate the centre of mass about the intensity maxima regions. Stenkamp and Jäger calculate the centre of mass from the area around the intensity maxima in the image [52]. They calculate the intensities using the Laplacian operator, which points to atomic positions. The one-dimensional profile method was proposed by Seitz et al. [51]. The profile across the image's maximum intensities is repeatedly taken and averaged. The intensity maxima are then calculated using an appropriate 2D function for intensity distribution to create a grid over the intensity maxima in the image that leads to the identification of the maxima positions [45].

The other technique used to measure strain is GPA. The GPA method uses masks around Bragg spots in the Fourier space of the image, after which the inverse to the Fourier transform is determined to obtain the real space of the image. The reflection spot in the FFT image is related to the two dimensional unit cell of the crystals [48, 31]. The technique uses an algorithm of a complex image which is in the Fourier space and real space. The GPA procedure consists of an asymmetric mask/filter applied at the centre of the Bragg's spot in the Fourier space image. The mask in the Fourier space will average and smooth the real space information when the image is reconstructed [45]. The result shows a complex image that gives information about relative local displacement which corresponds to the lattice fringes that are linked to the Bragg's spots. The derivative of the displacement is then taken to obtain the strain [39].

The Peak Pairs (PP) is a real space approach that was introduced to overcome certain limitations to the PF method. For example, the PF does not apply to area of

interest that contain defects such as interfaces and dislocations. The PP approach uses the filtering to reduce the noise. This filter could be the Wiener filter which could improve the resolution by a factor of 2-4. A Wiener filter is one of the linear filters which can be applied to an image in order to reduce the frequency at the edges and other parts of the image. The PP uses the image fringes instead of a dot pattern by applying a mask around one of two Bragg's points in Fourier transform image then apply the inverse Fourier transform to obtain the real space image. If the mask is very small, it is possible to remove information from the image, while a large mask can introduce noise into the images. The strain field determination in PP is achieved by interpolating all the image peaks. However, this is considered a limitation because, outside this area, the strain field close to the border of the image is not valid [39].

The PF and GPA are noise sensitive. Reducing the signal-to-noise ratio may result in a loss of information in the image. In the PF, the noise could include an intensity maximum, which could affect the displacement calculation, while the GPA, which deals with the Bragg spot getting filtered out, can result in the removal of information from the image [39]. GPA uses two reflection points in the Fourier space to construct the distortion field. The reference area in the PF can be chosen precisely as in the GPA method. For example, the reference area in GPA could have an error due to averaging in the Fourier space image information, which could impact the selection of the Bragg's reflections position. GPA is simple to use for measuring a region of interest that has a defect or dislocation [45, 39].

The implementation of the PP technique in this project offers it a highly appealing strategy. The displacement mapping approach was applied to the simulated image by identifying the peaks maxima in the simulated image and filtering the real space image. Additionally, the atomic columns in the images were identified and a displacement mapping procedure was conducted on the thesis images. For a more comprehensive explanation of the approach utilised for the implementation of displacement mapping in the images, see Chapter 5.

1.3 Structure of iron oxide

Iron oxide is one of the most common chemical species on earth. Iron, as a pure element, is rarely found on the earth's surface [53]. However, the crust contains other forms of iron such as magnetite (Fe_3O_4), maghemite (γ-Fe_2O_3), and haematite (α-Fe_2O_3) and Wustite [54].

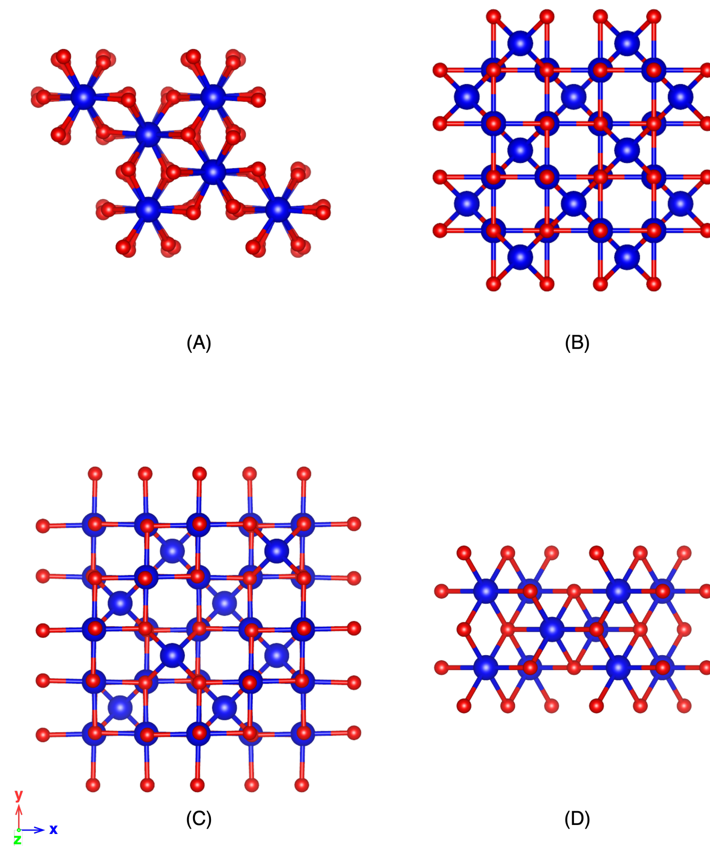

Fig. 1.4: Crystal structures of (A) haematite [1], (B) maghemite [2], (C) magnetite [3] and (D) Wustite [4]. Blue: Fe, Red: O.

Iron oxide structures can be described as close-packed planes that consist of oxygen anions with cations (iron ions) in either octahedrally or tetrahedrally arranged interstitial sites. For example, haematite (α-Fe_2O_3) (Fig. 1.4 A) has oxygen atoms arranged in a hexagonal close-packed structure, while Fe^{3+}occupies an octahedral site arrangement. Maghemite,γ-Fe_2O_3 (Fig. 1.4 B) and magnetite (Fe_3O_4) (Fig. 1.4 C), however, both have a cubic close-packed arrangement. The oxygen atoms form a face-centred cubic structure. In the case of magnetite (Fe_3O_4), the structure is

an inverse spinel structure which means the Fe^{3+} is either occupying octahedral or tetrahedral sites, while the Fe^{2+} ccupies octahedral sites. Maghemite, on the other hand, has a spinel structure (γ-Fe_2O_3) with has a trivalent state and cubic unit cell. The final common form of iron oxide is wustite (FeO), which has a fundamental structure identical in arrangement to that of NaCl, i.e., face-centered cubic. Figure 1.4 shows the structures of the various iron oxides; the primary forms and their proprieties are listed in Table 1.1 below [20].

Table 1.1: General properties of four forms of iron oxide [20].

Name	Haematite	Magnetite	Maghemite	Wustite
Formula	α -Fe_2O_3	Fe_3O_4	γ -Fe_3O_3	FeO
Crystirophy system	Hexagonal/ Rhombohedral	Cubic	Cubic / Tetragonal	Cubic
Packed	ABAB[001]	ABCABC [111]	ABCABC [111]	ABAB[001]
Density (gcm^{-3})	5.26	5.18	4.87	$5.9-5.99$
Colours	Red	Black	Reddish-Brown	Black
Hardness	$6\frac{1}{2}$	$5\frac{1}{2}$	5	5
Type of Magnetism	Weakly ferromagnetic or antiferromagnetic	Ferrimagnetic	Ferrimagnetic	Antiferromagnetic
Melting Point (C^o)	1350	$1583-1597$		1377
Boiling Point(C^o)		2623		2512
Heat of Fusion		138.16		31.4
Heat of Decomposition	461.4	605	457.6	529.6
Heat of Vaporisation		298 at 2623 C^o		230.3 at 2517 C^o

1.4 Conclusion

The theory underlying this investigation and the experimental and preparation methods are presented in the theory and experimental chapters, respectively. Applying a realistic displacement profile and 3D atomistic oxide shell model are addressed in methodology chapter as well as the COMSOL Multiphysics® program, as presented in the Finite element method (FEM) simulation. The results and discussion of the outcome will be given in the chapter on the displacement field's impact on the STEM images.

Chapter 2

Diffusion in Nanoparticles

2.1 Introduction

Strain relates to the atomic displacement caused by a stress field in reference to the unstrained relaxed state. It can be found in a variety of forms in nanoparticles (NPs). It leads to a corresponding displacement of atoms from their relaxed unstrained positions within the crystal lattice (if crystalline solids are considered). During the growth of crystalline NPs strain can induce the formation of grain interfaces, point defects or dislocations. As a result, the atomic arrangement inside the crystal will be disturbed, causing a strain around the defect affected area [31, 55]. This plays a central role in ion diffusion in the NPs because increasing the lattice strain leads to an increase in the diffusion coefficient of NPs [55]. Lattice strain generally affects the activation energy for the atomic diffusion due to the local variation of atomic spacing it induces. In case of increased spacing it increases mobility of ions and atoms and hence leads to increase diffusivity [55]. The effects of the Gorski effect are yet another illustration. Pratt et al. [30] demonstrates that the Gorski effect contributes to the enhancement of diffusivity as a result of strain gradients [30]. The iron oxide shell of cube NPs was the subject of their investigation. The oxide shell of Fe-base NP diffuses more readily due to strain-induced lattice diffusion [30]. However, the presence of grain boundaries also facilitates diffusion in NPs due to the fact that grain boundaries are crystal structural defects that enable ion transition through them [7, 10, 56].

This chapter will provide a theoretical conceptual framework for the project, for example, an overall description of diffusion, grain boundaries, and oxidation mechanisms, including the formation of metal oxide, it will provide fundamental details about how atoms move in matter.

2.2 Diffusion Mechanism

Diffusion is the phenomenon of atomic mass movement through some medium caused by a concentration gradient of the diffusing species. In metals, for example, this movement occurs along a so-called diffusion path, which could be a grain boundary, free surface entry or a dislocation. This movement could occur due to the motion associated with thermal activity among atoms or due to concentration gradients [57, 7].

2.2.1 Lattice transport

Fick's law describe the movement of atomic mass based on a concentration gradient $\frac{\partial c}{\partial x}$, with movement from regions of high concentration to low concentration [6, 5].

$$J = -D\frac{\partial c}{\partial x} \tag{2.1}$$

where J is the mass flux, which is the rate of mass transfer per unit area, D is the diffusion coefficient. The negative sign of the right hand side in Eq. 2.1 indicates the gradient change from high concentration to low concentration, c is the concentration difference, and x is the diffusion space in the x direction. Equation 2.1 shows Fick's first law for diffusion in one dimension. Equation 2.2 is also an expression of Fick's first law, but in this latter instance generalizes to three dimensions.

$$J = -D\ \nabla c \tag{2.2}$$

Equations 2.1 and 2.2 show the diffusion in terms of direction; Fick's second law, however, considers diffusion as a function of time t

$$\frac{\partial c}{\partial t} = D\ \frac{\partial^2 c}{\partial x^2} \tag{2.3}$$

Diffusion in a solid, more specifically in a crystal, can be categorized by three types of mechanisms: vacancy, interstitial and interstitialcy as defined in Fig. 2.1 [58, 5].By analyzing some of these mechanisms in, it might be noted that it is difficult for the direct exchange mechanism and ring mechanism to occur. The reason for this is that ions are close to each other and mutually repel, though to form a "site" or space into which ions can move requires a very strong force. On the other hand, other mechanisms, such as the vacancy mechanism, interstitial mechanism, and interstitialcy mechanism, allow for far less restricted movement as a fact of their proposed mechanisms, namely that there are already vacancies present which allow for interchange between atoms and for defect points [5, 58].

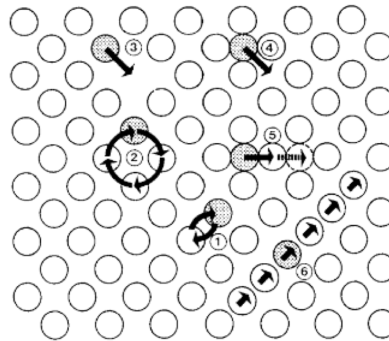

Fig. 2.1: Diagram shows the different diffusion mechanism types; (1) direct exchange mechanism, (2) ring mechanism, (3) vacancy mechanism, (4) interstitial mechanism, (5) interstitialcy mechanism and (6) crowdion mechanism [5].

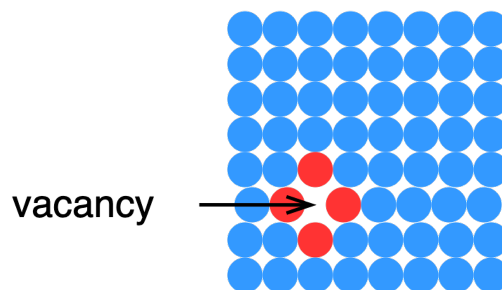

Fig. 2.2: The vacancy mechanism. The red atoms are the ones with the potential to go to the vacant sites. There is a higher chance of a jump happening at these atoms than at others due to the surrounding vacancy and defect. Atoms that are potentially close to a defect are shown in red. Atoms with no defect are blue.

As mentioned above, vacancy diffusion allows for relatively unrestricted atomic

movement. The presence of a vacancy allows for this movement, and the atom can jump, which means it can exceed the required activation energy to move from one vacancy to a neighboring vacancy, as shown in Fig. 2.2 [58, 6].

It is possible to describe the diffusion in this mechanism as follows. The atom will need enough energy in order to allow a jump. This energy must be higher than the associated activation energy, so the probability of the atom being able to jump can be expressed via the Arrhenius equation:

$$P_j = k \ \exp\left(-\frac{E_m}{k_B T}\right) \tag{2.4}$$

where k is the number of atoms attempting to jump; E_m is the activation energy for the displacement of an atom; T is temperature; and k_b is the Boltzmann constant (1.38×10^{-23} $J \setminus K$). In order for the atom to jump, it must have a neighbouring vacancy site, the probability of which can be expressed from thermal fluctuations, as follows

$$P = z \ \exp\left(-\frac{Q_v}{k_B T}\right) \tag{2.5}$$

where z is the coordination number and Q_v is activation energy for vacancy formation.

The product of Eq. 2.4 and Eq. 2.5, and by considering the area (a) over which diffusion occurs as equal to the diffusion coefficient in the vacancy mechanism, D, yields

$$D = a^2 \ z \ k \ \exp\left(-\frac{E_m}{k_B T}\right) \exp\left(-\frac{-Q_v}{k_B T}\right) = a^2 \ z \ k \ \exp\left(-\frac{E_m + Q_v}{k_B T}\right) \tag{2.6}$$

So Eq. 2.6 can be re-written as follows

$$D = D_o \ \exp\left(-\frac{Q_D}{k_B T}\right) \tag{2.7}$$

where D_o is the pre-exponential component ($a^2 \ z \ k \ \exp$) and Q_D is the activation energy required for the diffusion to occur, which is equal to ($E_m + Q_v$) [6].

Interstitial diffusion is generally related to a higher mobility of ions and atoms in lattices. This is particularly relevant for atoms/ions with small radii which more easily pass through the lattice without occupying lattice positions. E.g. for oxygen a

48 pm atomic radius is found in comparison to a value of 156 pm for Fe [59, 60].Hence replacing an iron atom by oxygen is less likely than forming interstitial defects[6]. In fact, after the solute atom jumps, it will return to it equilibrium position. Figure 2.3 shows the associated mechanism [6, 61].

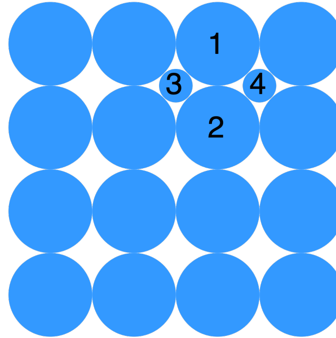

Fig. 2.3: The interstitial mechanism. Number 3 represents the solute atom that might jump to 4. 1 and 2 are solvent atoms.

Since the atoms move randomly in this mechanism, it is possible to say that the flux of the atom depends on the concentration gradient. Atom diffusion in crystal lattices follows a 3D random walk process [6]. Consider, two atomic planes as in Fig. 2.4. The distance between the two planes is λ and n_1 and n_2 are number of atoms. J_1 and J_2 flux atoms per unit area.

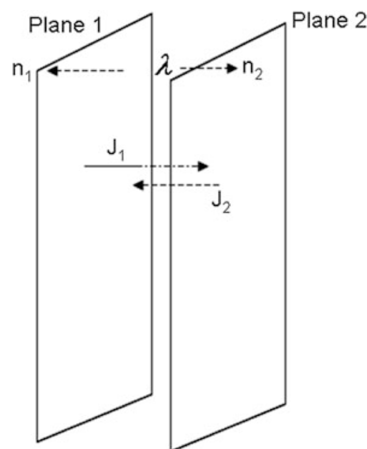

Fig. 2.4: Schematic showing two planes separated by distanceλ. Number of atoms n_1 and n_2 are in each plane. Fluxes J_1 and J_2 of atoms moving between the two planes [6].

The number of atoms that jump out of plane 1 in the interval $\delta\ t$ to plane 2 can

be expressed in Eq. 2.8 and the number of the atoms that jump out of plane 2 to plane 1 as in Eq. 2.9

$$J_1 = \frac{1}{2}\ n_1\ \Gamma_1\ \delta\ t \tag{2.8}$$

$$J_2 = \frac{1}{2}\ n_2\ \Gamma_2\ \delta\ t \tag{2.9}$$

where Γ_1 and Γ_2 are number of jump frequencies which is the number of jumps per second. It is worth noting that the jumps from each direction between the planes are half of the total number which is possible to say that net flux J from plane 1 to plane 2 is given in unit time as follow

$$J = -\frac{1}{2}\ \lambda^2\ \Gamma\ \frac{\partial c}{\partial x} \tag{2.10}$$

Equation 2.10 is equivalent to Fick's first law if:

$$D = \frac{1}{2}\lambda^2\Gamma \tag{2.11}$$

Above Eq.2.11 is valid for atoms diffusing in a random walk manner between two planes. However, if we consider atoms diffusing in a three-dimensions space, it is possible to rewrite Eq.2.11 as follow

$$D = \frac{1}{6}\lambda^2\Gamma \tag{2.12}$$

where λ^2 is the squared distance that the atom takes to jump and Γ is the number of atoms that jump per unit time, which can be expressed as follows for interstitial diffusion:

$$\Gamma = v_o\ z\ \exp\left(-\frac{\Delta G_m}{KT}\right) \tag{2.13}$$

where v_o is the vibrational frequency; z is the number of interstitial sites that the atom can jump to; and $\Delta G_m = \Delta H^i_m - \Delta S^i_m$ is the free energy that the atom needs to effect a jump, which is known as the Gibbs energy. By replacing Eq. 2.13 in Eq.2.12 , the diffusion coefficient in the interstitial mechanism can be expressed as

$$D = \frac{\lambda^2\ v_o\ z}{6}\ \exp\left(\frac{\Delta S^i_m}{K}\right)\exp\left(-\frac{\Delta H^i_m}{KT}\right) \tag{2.14}$$

The impact of the λ change over the D can be estimated for the Fe oxide system by using the realistic value of ΔG_m which is $-6.6kJ \cdot mol$ metal^{-1} [62]. Using Eq.

2.14 to estimate lattice spacing λ impacts on D for FeO system can be shown in Fig. 2.5.The ionic movement rate (v) or frequency for an ion to move to a neighbouring lattice site is of the order of 10^{13} s^{-1}. This shows that an increase of lattice spacing increases diffusivity and vice versa. Boltzmann constant (k_B) is 1.38×10^{-23}, and temperature (T) is $300K$ [28, 11]. The estimation indicates that the increase in lattice spacing will definitely increase the D.

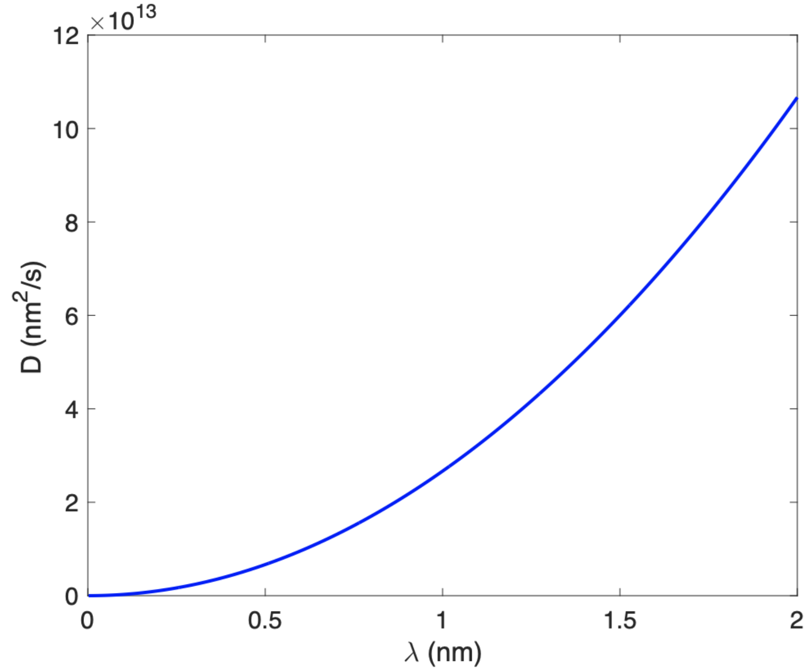

Fig. 2.5: Impact of lattice spacing λ on diffusivity D for the Fe-O system (using Eq. 2.14).

2.2.2 Gorski effect

The Gorski effect considers the impact of lattice strain gradients on particle diffusion in crystal lattices. It takes into account the local change of strain energy which introduces an additional term into the diffusion equation [63, 64, 5]. When the ion diffuses in the crystal, it will cause a lattice to expand; hence, it causes bending in the sample [7]. The diffusion relaxation (after effect) time τ_R in the metal as follows [5].

$$D_B = \frac{1}{\Phi \ \tau_R} \left(\frac{d}{\pi} \right)^2 \tag{2.15}$$

whereas d the dimension of the bending, Φ is thermodynamic factor.

Gorski effect also can describe the diffusion induced by the strain [30].

$$D_B = \frac{D}{k_B T} \frac{\partial}{\partial x} \left[\frac{dU}{dx} c(x,t) \right] \tag{2.16}$$

whereas D is diffusion coefficient and strain energy $U(x)$ is

$$U(x) = \frac{1}{2} \Omega_o E \varepsilon_{11}^2(x) \tag{2.17}$$

whereas Ω_o primitive unit cell volume, E is Young modulus of the oxide. $\varepsilon_{11}^2(x)$ is strain component.

Combine Eqs. 2.16 and Fick's second law 2.3, the impact of the Gorski effect can enhance the diffusion by strain gradients in the system as follows [30]

$$\frac{\partial c(t,x)}{\partial t} = D \frac{\partial^2 c(t,x)}{\partial x^2} + \frac{D}{k_B T} \frac{\partial}{\partial x} \left[\frac{dU}{dx} c(x,t) \right] \tag{2.18}$$

2.3 Grain Boundaries

In a solid polycrystalline structure, there are granular regions, or small crystal regions, which are separated by boundaries called grain boundaries (GBs). The GBs can be considered transition regions in a polycrystalline structure due to variations in atomic arrangement at the interface between two adjacent grains [57, 7, 9].

The grain boundary can be described by identifying the rotation of the grain axis as $\circ = [h_o k_o l_o]$ and the angle $\theta[h_o k_o l_o](h_{nA} k_{nA} l_{nA})$ as in Fig. 2.6. The grain itself can be identified by the orientation of its Miller index plane to the boundary plane [9]. GBs can be subdivided into three categories based on the relationship between the normal **n** of the grain boundary and its rotation axis **o**: 1) Tilt GB, where **n** is perpendicular to **o** ($\mathbf{o} \perp \mathbf{n}$). 2) Twist GB, where **n** is parallel to **o** ($\mathbf{o} \parallel \mathbf{n}$) and 3) Mixture GB, which is any GB where **n** and **o** are neither perpendicular nor parallel to each other,as in Fig.2.7 [9, 7].

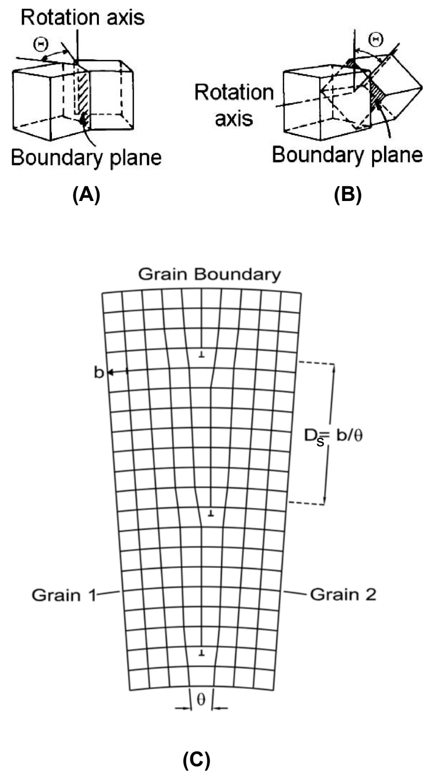

Fig. 2.7: Schematic shows the type of the GBs. (A,B) are tilt and twist, respectively. (C) shows dislocation space D_s as in Eq. 2.19 [7, 8].

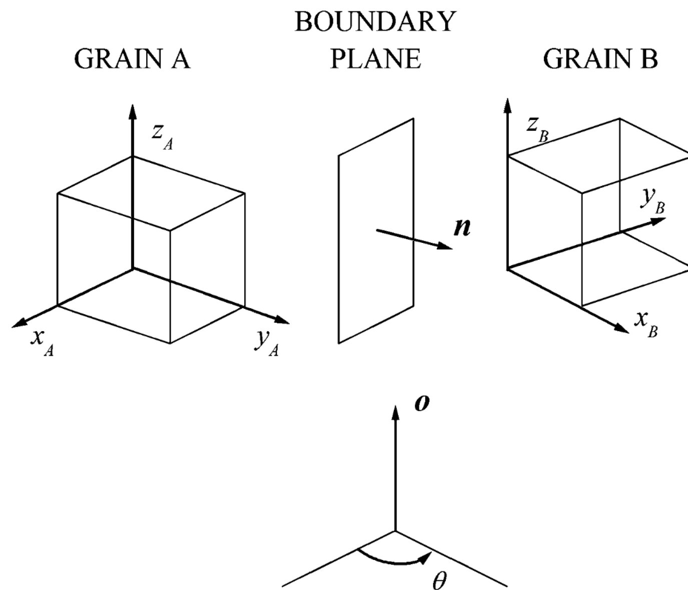

Fig. 2.6: Schematic shows grain boundary axis for two grains (grain A and grain B) as x_A, y_A, z_A and x_B, y_B, z_B. **n** is norm of the grain boundary and **o** is rotation axis. θ is the rotation angle [9].

In terms of the atomic structure of the GB, the misorientation that occurs between adjoining grains can be expressed as an angular mismatch. This degree could be either a high angle degree or a low angle degree. The angle of the grain boundary is related to the size of Burgers b vector and the dislocation space, D_s, as shown in the following expression [9, 57]:

$$sin\left(\frac{\theta}{2}\right) = \frac{|b|}{2D_s} \tag{2.19}$$

for low angles,

$$sin\left(\frac{\theta}{2}\right) = \frac{\theta}{2} \tag{2.20}$$

It is worth noting that should the orientation exceed $10^o - 15^o$, it would be difficult to identify dislocation. The reason for this is that D_s is much smaller than the dislocation core, which results in overlap and hence difficulty in identifying dislocation in these circumstances [7, 9].

2.3.1 Diffusion along the grain boundary

One of the mechanism that helps the diffusion in metal oxide is GB diffusion, which is due to the fact that the path will have an equilibrium concentration of irregular orientations in the crystal [7, 10, 56].

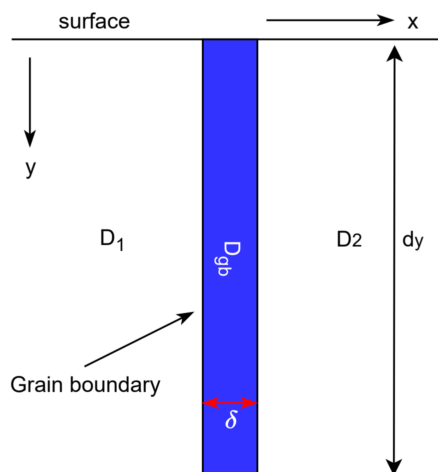

Fig. 2.8: The Fisher model. The notation shown in the figure is as follows: D_1,D_2 is the lattice diffusivity, D_{gb} is the diffusion in the grain boundary, and δ is the width of the grain boundary and d_y is the lateral grain boundary [7, 10].

The diffusion occurs in the GB due to the fact that there are either foreign atom layers, diffusing atoms present at the surface of the same material, or self-diffusion. The atoms will diffuse through these channels from the core to the surface due to the concentration difference in the system as outward diffusion [30], whereas the atoms will diffuse through these channels from the surface into the specimen either directly into the grain (as lattice diffusion) or via the GB interface, which can be expanded by Fisher model and is illustrated in Fig. 2.8 [9, 61].

The Fisher model considers that the concentration changes along the x-y symmetry plane (if the faces are normal to the x and y axes, which means face in the z plane = 0). So, concentration change J_z will be equal zero along the z axis. There will be self-diffusion along the x and y axes, which can be described as follows [61]:

$$\frac{\partial c_b}{\partial t} = \frac{1}{1 d_y \delta}\left[\delta\left(J_y - J_y - \frac{\partial J_y}{\partial y}dy\right) - 2dyJ_x\right] \tag{2.21}$$

$$\frac{\partial c_b}{\partial t} = \frac{-\partial J_y}{\partial y} - \frac{2}{\delta}J_x \tag{2.22}$$

Whereas $\frac{\partial c_b}{\partial t}$ is concentration change in the GBs. J_x is the flux, it is not at the grain boundary, which can be used by Eq. 2.1 which is the lattice diffusion in Fick's first law. However, the flux in J_y is the grain boundary diffusion, which can be written as Fick's first law.

$$J_y = -D_{gb}\frac{\partial c_b}{\partial y} \tag{2.23}$$

By substituting Eq. 2.1 and Eq. 2.23 into Eq. 2.22, we can describe the diffusion in the grain boundary by using Fisher model as follow for concentration in x and y axis $c(x, y, c_b)$

$$\frac{\partial c_b}{\partial t} = -D_{gb}\frac{\partial^2 c_b}{\partial y^2} + \frac{2D}{\delta}\left(\frac{\partial c}{\partial x}\right)_{x=\frac{\delta}{2}} \tag{2.24}$$

And the diffusion outside the gain boundary can be described by Eq. 2.1. If $|x| \geq \frac{\delta}{2}$, Eq. 2.1 will be dominant, and if the $x < \frac{\delta}{2}$, Eq.2.24 will be dominant.

The rate of diffusion in the GBs is generally observed to be higher compared to lattice diffusion. However, the lattice diffusion could be dominant for the small

NPs if there is a significant presence of vacancies within the lattice. The presence of vacancy defects in small NPs can be attributed to the strain induced within these NPs. Thus, it can possibly deduced that the concentration gradient in smaller NPs is higher, resulting in the dominance of lattice diffusion for these NPs [30].

2.4 Oxidation of metal oxides

At elevated temperature, certain metal oxides such as FeO will further oxidize since they are thermodynamically not stable. This can also occur during prolonged exposure to air [65, 66, 67].

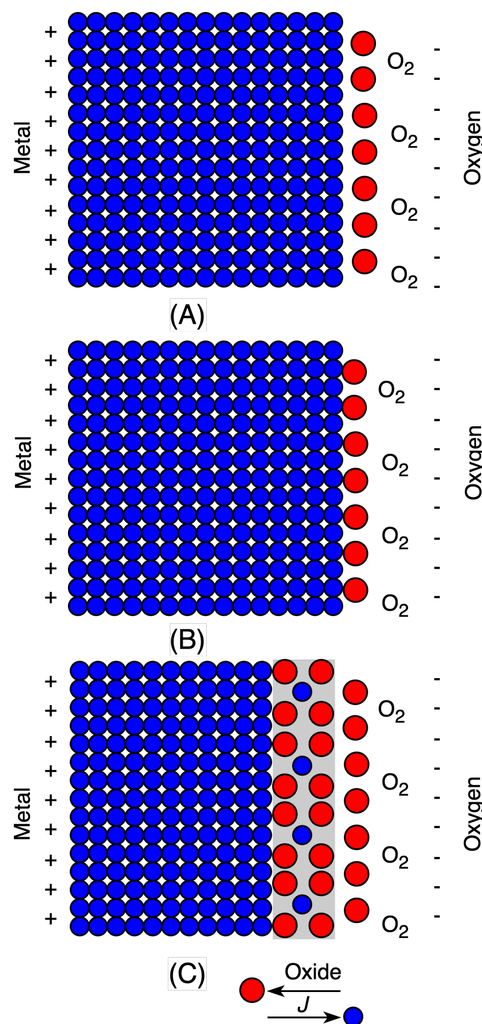

Fig. 2.9: Initial stages of oxidation between the oxygen and metal, as in (A) and (B). An intermediate layer (grey region) forms between the oxygen and the metal forms subsequently (C). J: mass flux. Red: oxygen, blue: metal.

At first, when Fe NP atoms interact with oxygen, for example, a very thin layer of oxide will form on their surfaces at room temperature. Then, the oxide layer will start to grow thicker due to diffusion of the Fe atoms in an outward direction [53]. After initial oxidation has occurred, an interference layer (oxidation area) will form, as shown in Fig. 2.9.

This layer will have an associated electric field resulting from the positive charge on the metal ions, which act as an anode, and the negative charge on the oxygen atoms, which act as a cathode. The mass flux of the metal will be towards the oxygen, and vice versa. The oxidation rate exponentially decreases with time due to the activation energy, until the oxide layer becomes around 20 to 100 Å[11, 68]; in fact, this turns out not to be the case, with oxidation continuing until the NP is fully oxidized, as demonstrated by Pratt et al. [30]. They showed that cubic iron NPs fully oxidize on a much shorter time scale due to the presence of strain at surface of cubic NPs. Not only this, but it was also possible to say that the oxidation process could be influenced by the very structure of the NPs themselves. For example, Pratt et al. also determined the oxidation rate for cubic iron NPs that changed over time to spherical iron oxide NPs [30]. They also noticed that these iron oxide NPs showed the Kirkendall effect void in the centre. This is because the iron and oxygen atoms have different diffusion rates [67, 30, 69].

The oxidation mechanism can be explained by Cabrera – Mott (CM) model and Wagner. According to the Cabrera – Mott (CM) model, the oxidation layer will have an associated electric field resulting from the positive charge on the metal ions, which act as an anode, and the negative charge on the oxygen atoms, which act as a cathode. The flux of the metal ions will be towards the oxygen, and flux of oxygen ions will be towards to the metal surface. The electron will flux through the oxidation layer due to the potential barrier between the metal / oxide interface and oxygen / gas interface. In the CM model, the oxidation layer has a limitation when it reaches an equilibrium point, which is around 2 nm to 10 nm because the electric field at the thick oxidation layer will not be strong hence the metal ion cannot cross the oxidation layer [70, 11, 68].

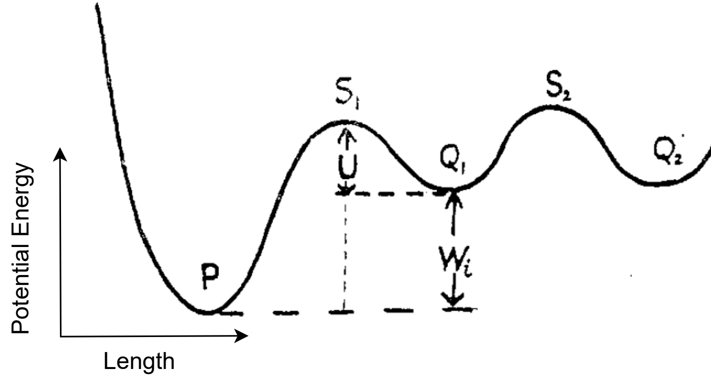

Fig. 2.10: Plot [11] shows the potential energy of the metal ion at the end of the metal / oxide layer interface. S_1 and S_2 are the top of the potential barriers. Q_1 and Q_2 are interstitial positions. P is the position of the ion. W_i is the energy difference between the interstitial positions and the ion. U is extra activation energy for ion to overcome the top of the potential barriers.

The CM model of oxidation can be explained as follows. In order to move an ion from one interstitial site to the next neighboring site as in Fig. 2.10, it has to overcome the potential barrier $W = W_i + U$ (W_i is the energy difference between the interstitial positions and the ion. U is extra activation energy for ion to reach the first interstital position [11]). The probability, P,for this ion to overcome this barrier to jump to next interstitial site can be expressed as

$$P = \exp \frac{-W}{k_B T} \tag{2.25}$$

k_B is the Boltzmann constant and T is temperature. However, in the presence of the electrical field, the potential barrier W will decrease:

$$P = \exp\left(-\frac{W}{k_B T}\right) \exp\left(\frac{q\ a'\ E}{k_B T}\right) \tag{2.26}$$

where q is the charge for each ion, E is the electrical field in oxide layer ($E = \frac{\Delta\Phi}{X}$), where $\Delta\Phi$ is Mott potential and X is oxide layer thickness. $W = W_i + U$ (energy require for initial jump) and a' is the distance between the ion position and the top of the potential barrier. If multiplying Eq.2.26 the ionic jumped frequency, v, the jump rate for ions with respect to Q_1 as in Fig. 2.10, is shown as

$$P(t) = v\ \exp\left(-\frac{W}{k_B T}\right) \exp\left(\frac{q\ a'\ \Delta\Phi}{X k_B T}\right) \tag{2.27}$$

From Eq. 2.27, the growth of the oxidation layer is given by:

$$\frac{dX}{dt} = N'\Omega\ v\ \exp\left(-\frac{W}{k_B T}\right)\exp\left(\frac{q\ a'\ \Delta\Phi}{X k_B T}\right) \tag{2.28}$$

where N' is the number of ions per unit area. Ω is the volume of oxide per metal ion.

An estimation of the growth rate of Fe oxide using Eq. 2.28 shown in Fig. 2.11. The parameters used to calculate the graph in Fig. 2.11 are as follows: The potential barrier $W = 2.5$J for the ion to jump from one interstitial site to the next neighbouring site, the volume of oxide per metal ion, $\Omega = 7.094 \times 10^{29}\text{m}^3$,the number of atoms per unit area, $N' = 2.44 \times 10^{19} \times 1 \times 10^{-4}$ atoms/m^2, the ionic jumped frequency $v = 2 \times 10^{13}$ s^{-1}, electron charge $q = 1.60218 \times 10^{-19}$ Coulomb, Boltzmann constant $k_B = 1.38 \times 10^{-23}$, temperature, $T = 300K$, Mott potential $\Delta\Phi = \frac{\Delta\Phi_0}{X}$ [28, 11].

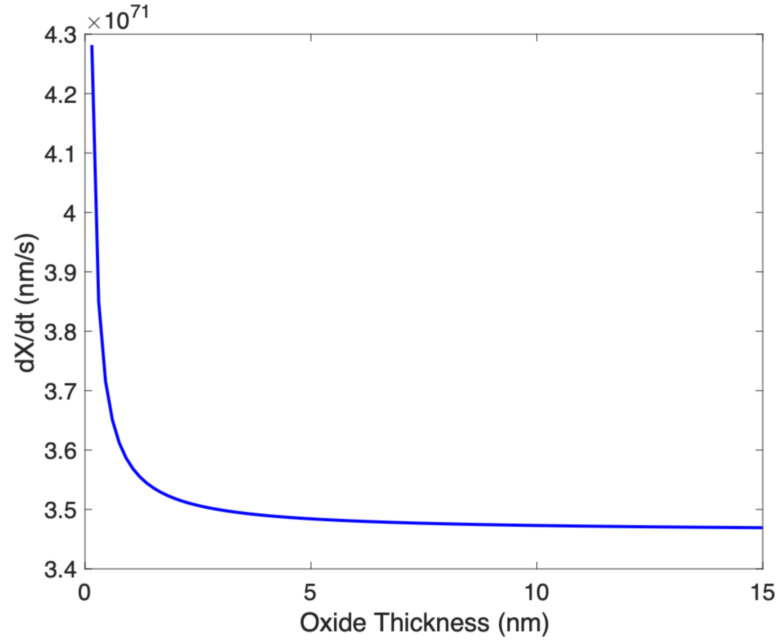

Fig. 2.11: Graph of estimated growth rate of iron oxide. Calculated using Eq.2.28

From Eq. 2.28, as a result it follows that as the oxidation thickness X increases, the rate of oxidation $\frac{dX}{dt}$ will decrease. Also, it is worth noting that in the presence of a strong field, the motion of the ion will be in one direction(field direction). Thus, every ion's escape from the metal will not recombine with the metal again because the strong field pulls the ion across the oxide layer [11, 71, 72]. However, the CM

theory is limited to the oxidation of thin films, which leads to Wagner's theory of oxidation that describe the oxidation of thick film [73].

Wagner considered that the oxidation in the metal is limited to a certain rate because it depends on the diffusion within the film, which is limited by the thickness of the film. Other factors, such as the reaction with oxygen and the temperature of the metals, might have an impact on the oxidation rate. Based on these factors, it is possible to predict and control the effect of the oxidation in the metals [74]. However, if the theory implies these factors, it is possible to argue that the rate of oxidation is related to the parabolic kinetics process, which can be described by using the following equation [73].

$$\frac{dX}{dt} = \frac{k_p}{2X} \tag{2.29}$$

where is X is the thickness, k_p is the parabolic rate constant which is the rate of the growth [73]. Equation 2.29 can be solved by differentiation, it is as follows:

$$X^2 = k_p\ t \tag{2.30}$$

whereas t is time.

Equation 2.30 shows the parabolic increase in thickness over time. Whether the oxidation is impacted by ionisation that is produced during the reaction in the metal oxide with the present temperature, the oxidation will continue, which indicates that the oxidation layer may continue until the NP is fully oxidised, as demonstrated by Pratt et al. [30]. They presented that cubic Fe NPs were fully oxidized due to the presence of strain at the surface of cubic NPs. Not only this, but it is also possible to say that the oxidation process could be influenced by the very structure of the NPs themselves. For example, Pratt et al. also determined the oxidation rate for cubic Fe NPs that changed over time to spherical Fe oxide NPs [30].

They also noticed that the Fe oxide NPs showed the Kirkendall effect void in the centre. This effect is due to the concentration of the Fe core NP decreased from the centre to the surface of the Fe particle during the oxidation process. This indicates that Fe diffusion is outward to the surface of the Fe oxide NP [75] and O diffusion is inward to the centre of the Fe oxide. As a result, there is a different rate of diffusion

between Fe and O [67, 30, 69].

Chapter 3

Experimental

3.1 Introduction

The nanoparticles (NPs) were synthesised by a technique called cluster source. The cluster source provides advantages by allowing for the control of physical features of the NPs, such as the size and shape of the NPs [76]. The aberration-corrected STEM is used to analyse and characterise these NPs, providing details about the structure of NPs and performing strain analysis using Z-contrast imaging with HAADF because the STEM contrast with a high spatial resolution image can be used to perform strain analysis of these NPs. This is because the contrast in the STEM image indicates the atomic columns' position in the specimen [17, 31]. The working principles behind cluster source deposition and STEM imaging are discussed in this section. The discussion briefly summarises the cluster source component mechanism. In addition, a brief comparison is made between TEM and STEM. The chapter introduces a discussion of scanning transmission electron microscope(STEM). Image formation in STEM is covered as well.

3.2 Cluster source

Chemical, biological, physical, and gas-phase methods have all been developed to synthesise NPs. Although these methods have the potential to synthesise a wide range of NPs, their application has thus far been limited. For instance, in order to

examine the images of these NPs for strain analysis, the NPs must be of a very high quality and have a low level of contamination by substances like ligand. Although the NPs can be made relatively cheaply and with some degree of efficiency using the chemical processes of solo-gel and dendrimer template, the NPs themselves are in a hydrosol state. Although the use of bacteria in the biological method for NP growth is a natural one, the difficulty in precisely controlling the size of the NPs results is a significant disadvantage of this approach. The physical technique creates the NPs as a powder, which requires a soluble form by attaching ligands to powder, and this can have an effect on the image quality. Finally, gas-phase methods such as sputter-gas-aggregation sources (SGAS) produce NPs under high vacuum in the gas-phase. The key benefit of SGAS is that the NPs can be controlled, despite the fact that the amount of NPs produced is lower than with other approaches. For example, the shape and size of the NPs can be easily controlled in this process; additionally, this method can be utilised to make core shell NPs as well[76].

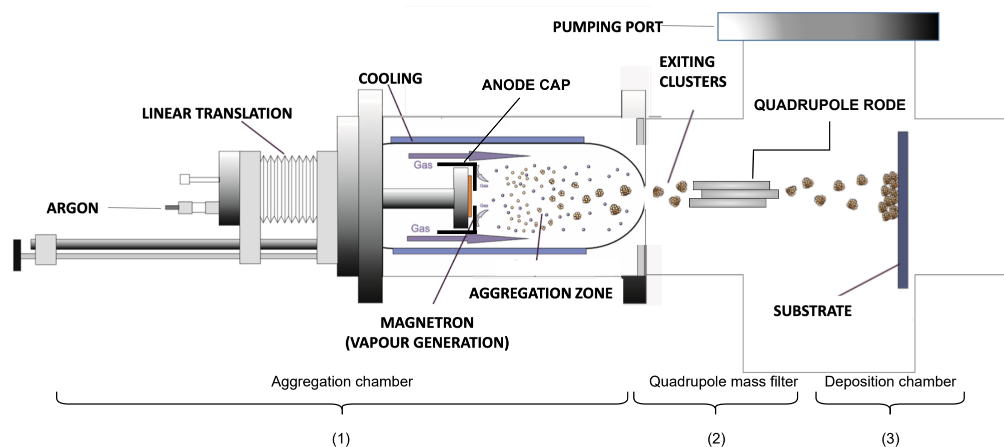

Fig. 3.1: Cluster source components. The first component is the aggregation chamber. The second part is the quadrupole mass filter. The third part is the deposition chamber. Figure adapted from [12].

The SGAS approach involves the use of three main chambers (see Fig. 3.1). The first is the aggregation chamber (sometimes called the cluster production region) where the NPs are produced. In this section, an inlet introduces a gas (e.g., Ar or He) into the system. A sputter head is located in this part which works by introducing Ar around a target disc (in our case a Fe target) which is subjected to

an electric current. The target disc acts as a cathode and the outer cap (see Fig. 3.1) serves as an anode. Hence, the Ar atoms are ionised and accelerated towards the target disc surface. As a result, the particles from the target surface will be vaporised and accelerated towards a substrate. The collision between the Fe atoms and the ionised Ar creates significant kinetic energy that facilitates cluster production of the Fe atoms. The magnet is present behind the target disc which maintains the plasma in the system. The released atoms flow to the aggregation region by two inlets. Here, the size of the NPs can be controlled because the length of the aggregation region allows time for collisions between particles, resulting in more and larger-sized cluster particles. However, other factors can also control this property such as the pressure of the carrier gas (He), the pressure of the supporting gas, and the sputtering power[77, 78]. The second component of the SGAS is a quadrupole mass filter for size selection and potentially a core/shell chamber where the particles are coated (hence the core/shell designation). Here the selection process is based on the mass-to-charge ratio of the cluster which can be selected by the quadrupole electric field. It is possible to set the desired mass value for ions to transmit them to the ion detector plant [78].

A prerequisite for the shell growth is that the temperature of the shell material needs to be lower than the evaporation temperature of the core [77, 78]. Also, the TEM grid is located in this part of the SGAS to allow further analysis of the sample [78, 79]. Figure 3.1 illustrates the cluster source components.

3.3 Electron microscopy

Electron microscopy (EM) was introduced to overcome the resolution limitation associated with the visible light microscope (VLM). EM uses the electron beam as the illumination source, whereas the VLM uses the light as the illumination source with wavelengths between 400 nm and 700 nm. The advantage of the electron beam wavelength over the light wavelength is the ability to image a small subject approximately 1.2Å to 3Å, compared to the VLM which is limited to 300 nm. The

distance, d, between the lattice plane can be viewed as follows

$$d = \frac{1.2\lambda}{\sin\theta} \tag{3.1}$$

Where d is the distance between the lattice plane and λ is the wavelength of the electron which can be calculated as follows

$$\lambda = \frac{h}{\sqrt{2m_0E\left(1 + \frac{E}{2E_0}\right)}} \tag{3.2}$$

Where h is Planck's constant, E is the electron's kinetic energy, E_0 is rest energy, and m_o is the electron's rest mass. Meanwhile, $\sin(\theta)$ is the semiangle of the lens/aperture[80, 81]. As shown in Eqs. 3.1 and 3.2, the relationship between the wavelength and the distance is a correlated relationship which means if the wavelength is particularly large, this affects the ability to image a small subject.

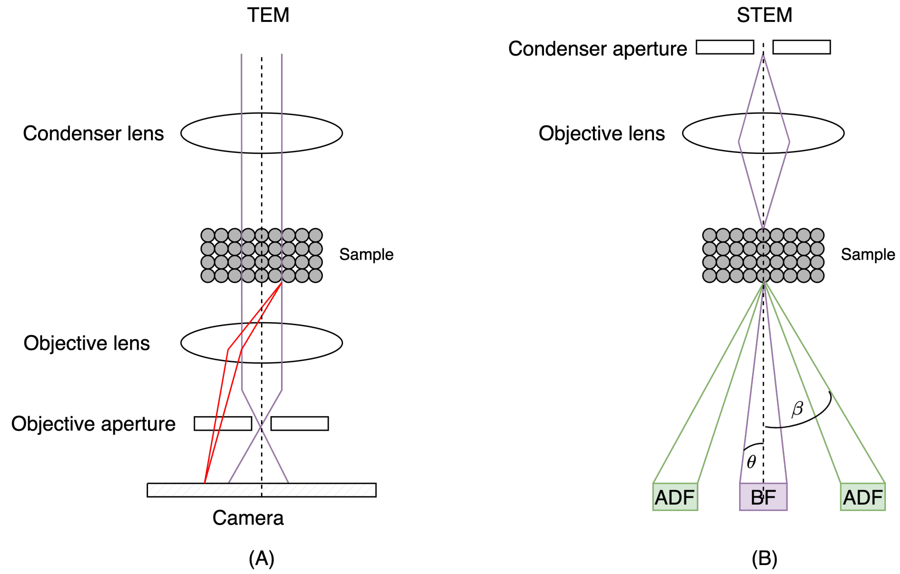

Fig. 3.2: (A) representing the TEM, red representing the DF scattered electron. The purple line is representing the BF scattered electron.(B) representing STEM, green line shows the ADF detectors at β angle. The purple line is representing the BF detectors at θ angle [13].

There are many varieties of EM, such as the transmission electron microscope (TEM) and the scanning transmission electron microscope (STEM). Figure 3.2 presents a brief illustration comparing the two instruments. Because the experimental images utilised in the project are predominantly from STEM, the primary

focus will be on the STEM instrument. However, the instrument structures between the TEM and STEM differ regarding the condenser lens (CLs) objective lens (OLs) positions. Another differences between STEM and TEM concerns the detector. STEM uses detectors that collect scattered electrons, such as the HAADF detector[82].

Furthermore, a STEM with high-angle annular dark-field (HAADF) detectors can provide information about the chemical contrast in the image since the intensity in the image is directly related to the thickness and atomic number of the scattered atoms.

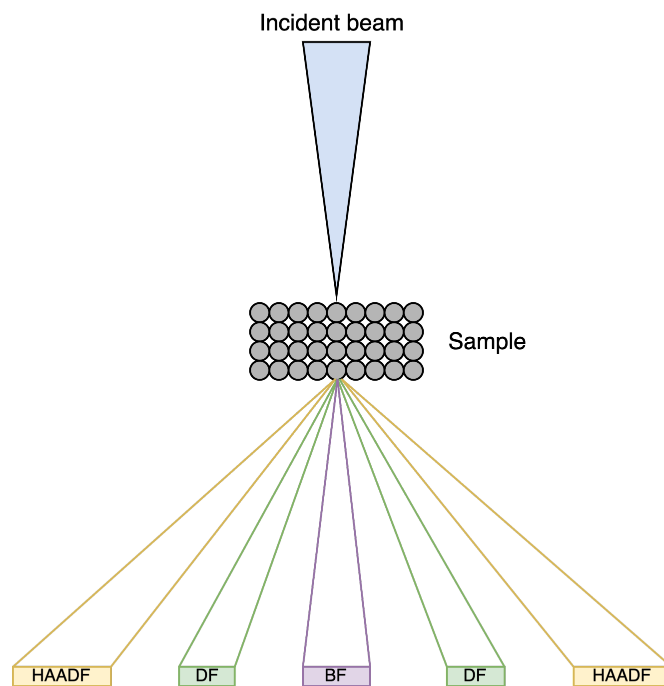

Fig. 3.3: Summary of the electron beam detected by STEM. If the beam is scattered at low angle, the BF detector will detect the beam. However, if the electron beam is scattered at a high angle, it is a DF detector that will collect it. If the electron is scattered at a higher angle, the HAADF detector will detect the scattered electron. The angles in the simulation are 0–40 mard for BF detector, 90–200 & 110–180 mrad for HAADF detectors.

The atomic column positions are shown as to the high intensity regions in HAADF imaging [31]. Hence, the projection of the atomic columns in HAADF – STEM is presented in the image as bright spots, which depends upon two factors:

the atomic number (Z) and how many atoms are along the atomic columns and contribute to the scattering [46].

STEM offers the ability to control how many electrons can contribute to the image. For example, in the HAADF image, the electron makes a greater contribution to the image because the angle in this mode is large due to the use of the annular (ring shape) detector. The ADF-STEM detector collects the most electrons scattered from the sample because the STEM does not use the lens to form the images; the lens is used in STEM to form the probe, which means the ADF image does not have any effect on the image such as aberrations [83]. Figure 3.3 illustrates the electron beam detected in STEM. HRTEM images cannot be directly interpreted due to the coherent nature of the probe electrons, leading to interference related contrast, which requires simulating the electron wave propagation through the electrostatic potential distribution of the atomic cores in the specimen. In contrast, STEM provides directly interpretable images since the electron incoherence does not lead to thickness-dependent interference of the scattered electrons, which can be explained as follows

$$I\left(R_0\right) = \mid P\left(R_0\right) \mid \otimes\, 0\left(R_0\right) \tag{3.3}$$

where I (R_0) is the intensity distribution of the probe and $0(R_0)$ (object function) is the inverse FT with respect to the spatial frequency. The equation explains the probe's interaction with the real space intensity position P(R_0)[14]. This means that the intensity distortion is the in the image resulting from convolution of the probe with the objective function ($\otimes$ means the multiply and integrate [17] see Appendix D) with the real space intensity position P(R_0)[14].

3.3.1 Scanning transmission electron microscope

STEM is an electron microscopy technique. It was first introduced on 1966 by Crewe [46]. STEM uses a sub-atomic scale electron probe around sub-1.0Å[84] to scan a thin specimen and to produce an image of it by detecting the scattered and unscattered electrons post specimen. The sample needs to be thinner than approx. 100 nm (depending on composition and density) to allow electrons to pass through

for detection [85]. Magnetic lenses are used to create a sub-atomically thin probe by converging the electrons emitted from the electron gun. Figure 3.4 provides a schematic of a STEM [14].

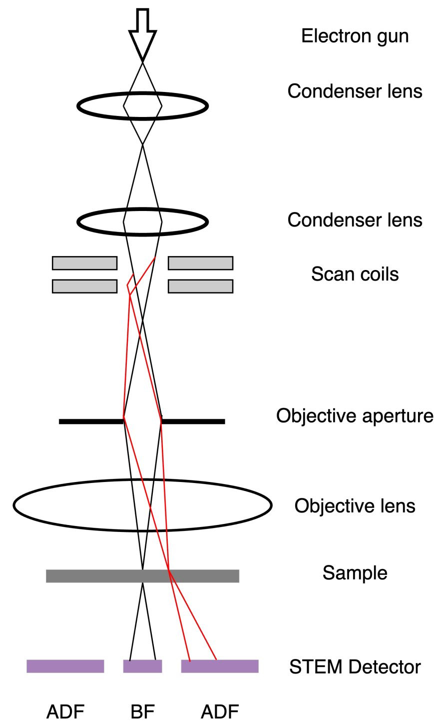

Fig. 3.4: The instrument component of the STEM. When the transmitted beam scatter at small angle, BF detector will detect the electron beam as shown in black line. When the electron is scattered at high angle, the ADF detector will detect the electron as shown in red line [14].

STEM components

The principal components of a STEM are shown in Fig.3.4. The electron beam is produced by the field emission gun, which releases highly intense beams from a small tip. The calculation of the probe current may be derived from the brightness B, which is determined by the current density per unit area and the solid angle α that the beam subtends. This relationship is expressed in the following equation

$$d = \sqrt{\frac{0.4j}{B\alpha^2}} \tag{3.4}$$

Where d is the probe diameter and j is the probe current can expressed as

$$j = \frac{en_i}{\Delta t} \tag{3.5}$$

where n_i is number of the electron per unit area (Δt) that is controlled by the condenser aperture. Rewriting Eq.3.4, the probe current expressed as

$$j = \frac{B\pi^2\alpha^2 d^2}{4} \tag{3.6}$$

From Eqs. (3.6, 3.5), it is possible to say that to obtain a smaller probe, the current should be lower. Therefore, a high brightness of the electron source is necessary to get reasonable current, which means that the brightness and the condenser aperture in STEM play a role in determining the probe size [14, 46].

Next, beam passes through the condenser lens (CL). The CL allows to create a concentrated probe which scans the specimen using deflection coils[46]. The objective lens (OL) is positioned above the specimen in STEM configuration. It concentrates the probe onto the sample[83]. The magnetic lenses facilitate the focusing of the electrons along the optical axis [14]. In a first step the electron beam emitted from the source is focused by the condenser lens CL_1 which creates a crossover that leads to a large demagnification of the electron source[85]. The lenses impose aberrations due to the fact that are electromagnetic lenses. The electron that passes through the lenses will experience a magnetic force (Lorentz force) that deflects the electron trajectory, as shown in Appendix A Fig. A.2. When the electron enters a magnetic field $\vec{b}$ with velocity $\vec{v}$, the electron will be under force $\vec{F}$ (the Lorentz force) which can be expressed as

$$\vec{F} = -e \cdot \vec{v} \times \vec{b} \tag{3.7}$$

From Eq. 3.7 the force, velocity and magnetic field are a cross product vector, so $\vec{F}$ is perpendicular to $\vec{b}$ and $\vec{v}$. This confirms that the electron direction will be influenced by this force $\vec{F}$ [17, 19]. For details about Cs-correction in STEM see Appendix A.

The probe interacts with the thin sample, creating a convergent-beam electron diffraction (CBED) pattern in the back focal plane of the OL. The annular or high

annular angular dark field detector (ADF, HAADF, respectively) collect the electrons scattered away from the optical axis whereas the bright field (BF) detector collects those electrons undergoing no or minimal scattering. The probe position as set by the scan coils is synchronised with the corresponding electron current measured by the respective detector giving rise to the resulting dark field or bright field HRSTEM image [46, 86, 87].

3.3.2 Image formation

The process of image formation in STEM can generally be subdivided into several stages. The first stage is the generation of the probe which, as previously mentioned, is required to be subatomic in extension (1 Å or less). This probe is scanned by deflection coils in x- and y- direction across the sample, which scatters the electrons by the electrostatic potential of the atomic cores. The second stage is characterised by the formation of a CBED pattern in the back focal plane of the objective lens created by the proble/sample interaction. In a third stage scattered signal is detected by bright-field, an annual or high angular annual dark field detector (ADF or HAADF). At this stage, it is possible to control the image mode, namely bright field or dark field making use of the different scattering angles related the respective scattering processes in the sample. Using electrons scattered at a low angle around (e.g. 0-40 mrad) with respect to the optical axis, a bright-field STEM image can be obtained. For electrons transmitted at a larger angle around (e.g. 40 mrad onward)with respect to the optical axis an ADF image can be obtained. At higher angles an HAADF detector (e.g. 70 mrad onward) allows the recording of Z-contrast images. Generally, electrons passing through the sample lose energy due to inelastic scattering. This energy loss is related to chemical information which can be recorded using electron energy loss spectroscopy (EELS). X-rays emitted by the sample due to the interaction with the primary probe electrons give rise to the possibility to use an energy dispersive X-ray (EDX) detector. The energy loss and emitted X-rays can be used for element and plasmon analysis [14, 46].

3.3.3 Bright-field image and dark-field image

In the BF image in STEM, the detector only picks up the direct beam. The electron beam is scattered along the optical axis. Therefore, using a small detection angle close to the optical axis can lead to a bright-field image in STEM because there is a triple overlap region close to the optical axis. It is a direct beam (0) and two other beams are scattered from the sample $(g, -g)$. The overlapping leads to an intensity which the detector uses to produce an image, as shown in Fig. 3.5. Bright-field image intensity can be found using the following equation[14]

$$I_{BF}(R_0) = 1 + 4 \mid \alpha V_g \mid \cos(2\pi g \cdot R_0 - \angle V_g) \sin\chi(g) \tag{3.8}$$

Where V_g is Fourier component of the specimen potential for gth, R_0 is the probe position, g is beam scattering, αVg is the weak phase object, and $sin\chi(g)$ is the phase shift of the scattered beam.

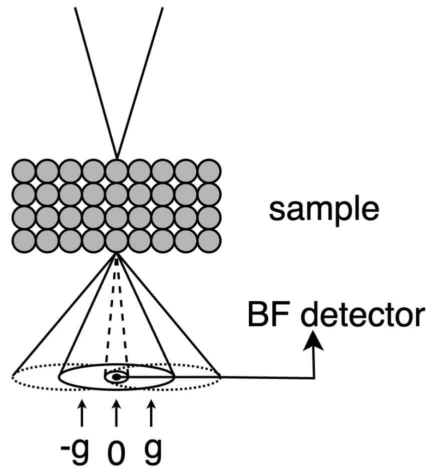

Fig. 3.5: The diffraction of the beam when it is coherent. The discs overlap, leading to interference between the direct beam and scattered beam [14].

The phase contrast in bright-field images in STEM is given by phase shift $sin\chi$. However, the phase contrast transfer function is limited by lens aberration. As previously mentioned, the image contrast results from interference between overlapping scattered beams and direct beams. However, the overlap occurs if the radius of the scattering illumination is larger than the magnitude of the scattered rays (g) [17, 14].

3.3.4 Annular dark-field (ADF) image

Crewe et al. first used the annular dark-field (ADF) detector in 1980. The technique uses a sensitive ring-shaped detector to detect electrons scattered through a region consisting of an angular range. The inner radius is between 10 mrad and 100 mrad and the outer radius is several hundred mrad. The detector is positioned at the centre of the optical axis. In the middle of the detector, there is a hole in the position of the BF detector. It is possible to add another detector close to the ADF detector to collect more scattered beams at an even higher angle. By adding this feature to the microscope , a new image mode can be obtained called high-angle dark-field (HA) ADF (or Z-contrast) images[17, 14]. The HAADF-STEM is a technique that is used to provide information not only about the structure of a specimen at the atomic level but also about the compositional analysis of that specimen[46, 88].

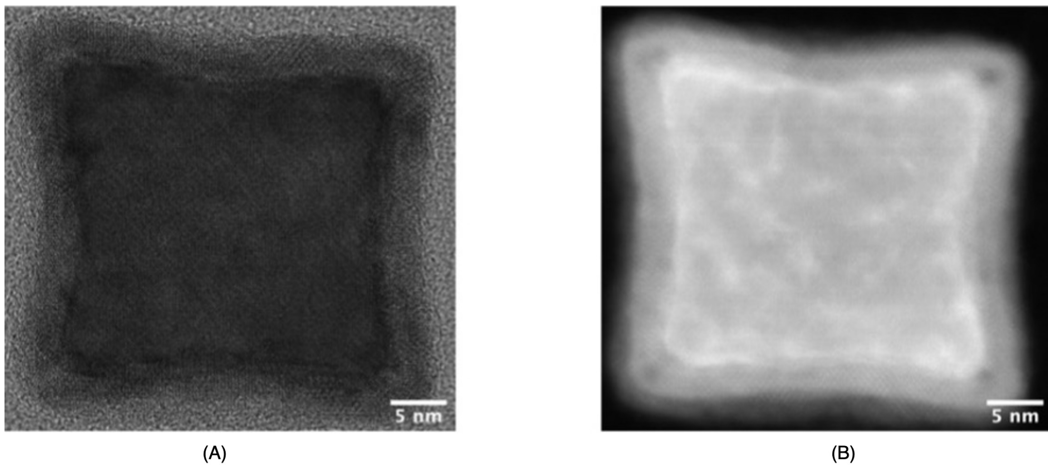

Fig. 3.6: (A)image is a bright-field STEM image of a Fe/Fe oxide core-shell structure, whereas the (B) image is a HAADF STEM image of a Fe/Fe oxide core-shell structure.

The projection of the atomic columns in HAADF-STEM is presented in the image as bright spots which depends upon two factors: the atomic number (Z) and how many atoms there are along the atomic columns. There are three stages in the formation of a HAADF STEM image. The first stage is incident probe formation; in the second the probe should propagate within the sample; and the third is scattering beam collection via the detector, depending on whether the bright-field STEM image angle should be small. In contrast, if it is dark-field STEM image, the angle should

be large [88]. Figure 3.6 shows a bright-field image and a HAADF image.

3.3.5 Thermal diffuse scattering

The atoms at room temperature will be vibrating, which is an effect shown in the microscope images. So, the image contrast will be effected by thermal diffuse scattering (TDS) or thermal vibration in the crystal lattice [89]. The origin of the TDS arises from the interaction between the probe and the phonons present in the sample, resulting in the dominance of the thermal diffuse scattering (TDS) image in terms of image contrast[14]. Thermal lattice vibrations occur when the ADF detector collects inelastic scattering electrons at the collecting angle, and, as a result, Bragg's beam intensity will be weaker and another intensity will occur as diffuse intensity, which is called TDS [90]. The TDS wave causes an intensity effect on the image because the TDS wave is produced at the individual atomic position, which causes a vibration that affects the beam at this position [91].

One approach to simulate a TDS effect involves the utilisation of the frozen phonon technique. This technique entails the introduction of dynamic thermal vibrations to each phase of the slice inside the multislice method. The introduction of additional motion will result in the displacement of atoms from their respective equilibrium locations. The approach will replicate the TDS findings, which are crucial for the modelling of STEM images. This is because the method reveals the correlation of atomic displacements among neighbouring atoms. As a consequence of employing this methodology, the atoms inside the model will no longer exhibit periodicity [88, 92].

Chapter 4

Methodology

4.1 Introduction

The project methodological approach consists of several steps: developing a three-dimensional atomistic oxide shell of Fe_3O_4 NP model, generating a realistic three-dimensional displacement field, applying the displacement field to 3D atomistic oxide shell, simulating the model, and analysing the results with respect to the impact of strain on column intensities and positions to extract the effective displacement fields. This schematic is shown in Fig. 4.1.

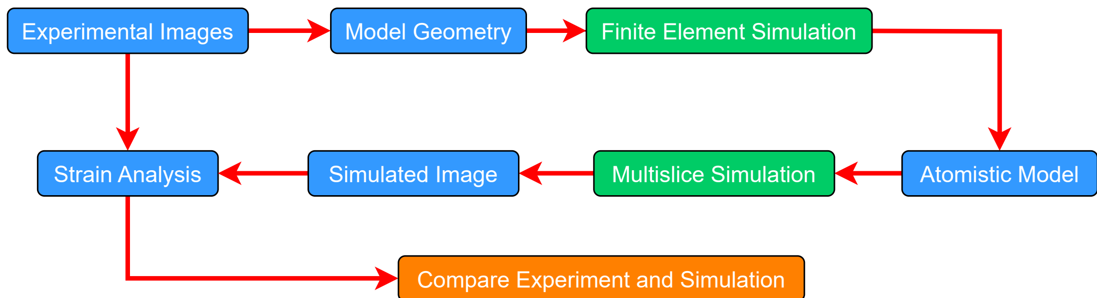

Fig. 4.1: Workflow describing the procedure for the quantitative analyses of atomistic strain in iron/iron oxide core-shell NPs. Based on experimental images, which were evaluated with respect to the atomistic strain, a model geometry of a NP is generated and proposed strain fields applied to an atomistic model of the NP. Using QSTEM [15] Z-contrast images are then calculated for these structures and subsequent strain analyses performed and compared to the experimental data.

This chapter explains how to utilise characteristics of the experimental image such as the geometry, thickness and the length of the nanoparticles (NPs) to create 3D models. The displacement field will be calculated using the finite element simulation software COMSOL Multiphysics® [33]. Further, the integration of the strain field into an atomistic model of the NP will be described leading to a displacement field. Subsequently, the resulting strained NP crystal structure will be simulated using the Quantitative TEM/STEM Simulations (QSTEM) code [15].

4.2 Experimental Z-contrast images

The input model was created based on the NP dimensions identified from the experimental images recorded for cubic particles, such as the side length, thickness, and geometry of the oxide side face of cubic Fe@Fe_3O_4 NPs. The experimental data used were Z-contrast STEM images obtained using a high-angle annular dark field (HAADF) detector and aberration corrected STEM. The NPs were prepared by a cluster source, as discussed in Chapter 3. Figures 4.2 - 4.5 are Z-contrast images for NPs with lateral sizes of 15 nm, 21 nm, 27 nm and 34 nm, respectively. Independent of size the oxide thickness was found to be 3 nm for all NPs and void formation occurred at the NP corners for particles >15 nm. Furthermore, it is recognisable that with increasing size there is a concave inward flexion of the core/shell side faces. The inward flexion could be due to the decreased stability of the cubic geometry for larger NPs whereas the void formation is likely due to the increased-out diffusion of iron from the core along the grain boundaries formed by the oxide segments.

In general, the cubic Fe@Fe_3O_4 NPs consist of cubic iron core bases and six truncated pyramids which grow in size and shape upon the progression of oxidation whilst the core diminishes. Figure 4.6 shows an exploded view of an idealised representation such a NP alongside the assembled structure. Due to the complexity of the system, the model structure used for the strain application concentrates on one iron oxide shell to determine the principal influence of strain on Z-contrast images.

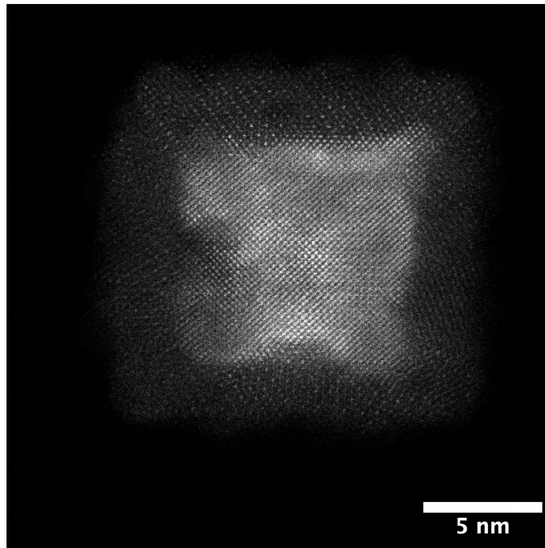

Fig. 4.2: HAADF image C_s corrections of a cubic 15 nm core/shell Fe/Fe oxide nanoparticle with a 3 nm oxide shell. Voltage = 200 (kV), detector angle = 110-180 (mrad), dE = 0.8 (eV).

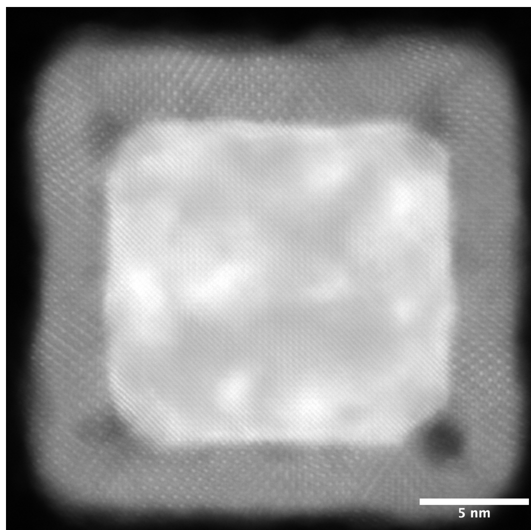

Fig. 4.3: HAADF image C_s corrections 21 nm core/shell Fe/Fe oxide nanoparticle with a 3 nm oxide shell. Voltage = 100 (kV), detector angle = 90-200 (mrad), dE = 0.3 (eV).

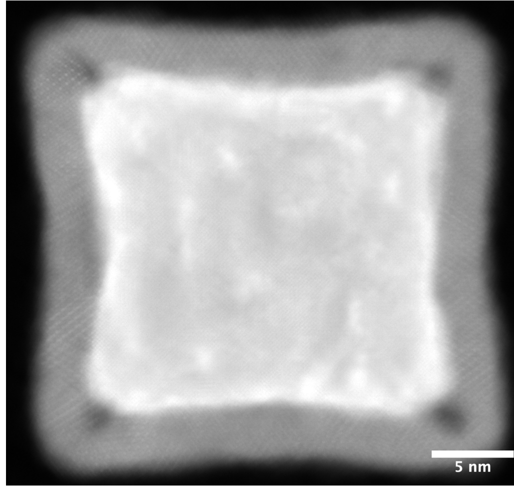

Fig. 4.4: HAADF image C_s corrections 27 nm core/shell Fe/Fe oxide nanoparticle with a 3 nm oxide shell. Voltage = 100 (kV), detector angle = 90-200 (mrad), dE = 0.3 (eV).

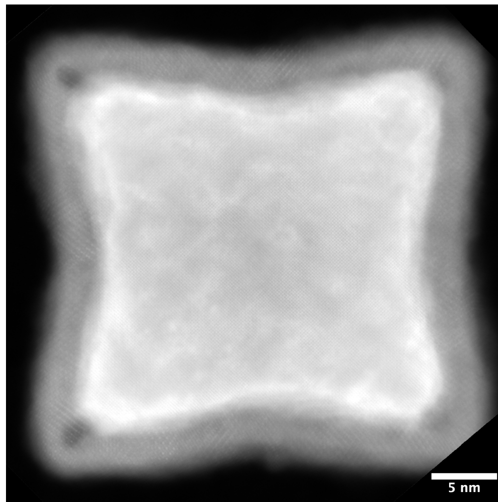

Fig. 4.5: HAADF image C_s corrections 34 nm core/shell Fe/Fe oxide nanoparticle with a 3 nm oxide shell. Voltage = 100 (kV), detector angle = 90-200 (mrad), dE = 0.3 (eV).

The oxide shell is represented by a truncated pyramid with truncation angle of 45° [93]. From the analyses of the Z-contrast images the presence of significant lattice strain in the oxide shell was found for particles below 20 nm side length. As a reason for this it is speculated that the truncation angles for the unstrained oxide domains deviate from 45° and, since the resulting gap is energetically unfavourable, this leads to a closure of this gap inducing a corresponding lattice rotation and

straining as was previously found by atomic column position analysis [30].

To obtain a realistic model of the strain induced displacement of the atomic positions in 3D a model geometry was chosen starting with an unstrained oxide domain, which would then be subjected to a stress induced due to the required rotation of the oxide side facets to achieve gap closure. For this purpose, finite element (FE) simulations were performed on this geometry using a commercial FE software package COMSOL Multiphysics® [33].

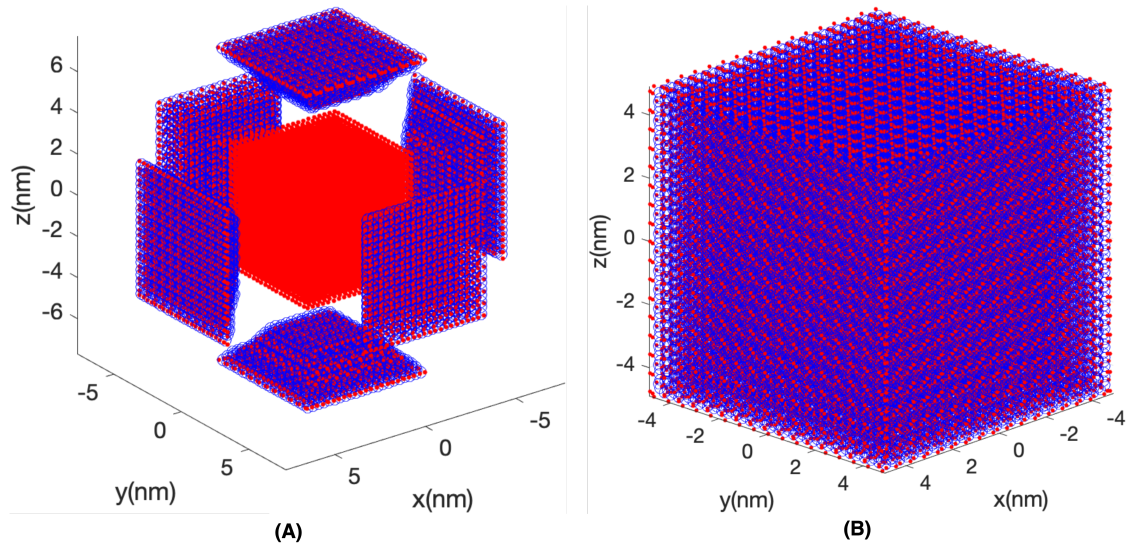

Fig. 4.6: An idealised representation of the components of an oxidised cubic iron/iron oxide NP: (A) exploded view, (B) assembled. Red: iron, blue: oxygen.

Extensions of these segments were derived from observations made in the experimental images, such as the oxide length and the core-shell interface length, and used as model parameter input for the calculation of strain distribution providing a displacement field [33] to be applied to the oxide crystal structure of the same geometry. The identification of the truncated pyramids on the STEM image is depicted in Fig. 4.7. In this instance, the top facet of the oxide shell is 15 nm and its thickness (height) is 3 nm, as shown in red. The schematic in Fig. 4.8 illustrates the core base and oxide shell of the STEM image in Fig. 4.7. Figure 4.9 shows a sketch of the red line (region of interest) in the STEM image which represents the oxide shell model. As shown in Fig. 4.9, the triangle properties were used to calculate the oxide shell dimension (see Fig. 4.7).

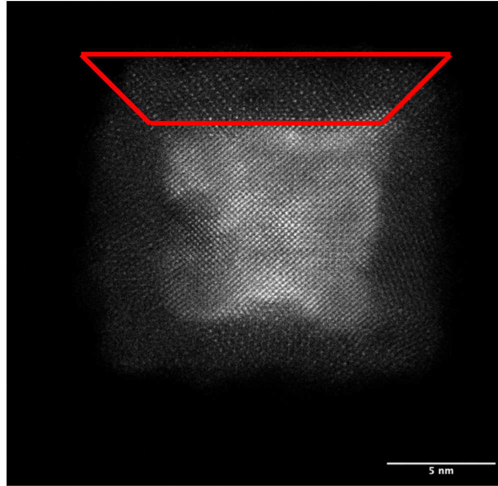

Fig. 4.7: An oxide shell segment (region of interest) indicated for the 15 nm NP to be used for the strain simulation.

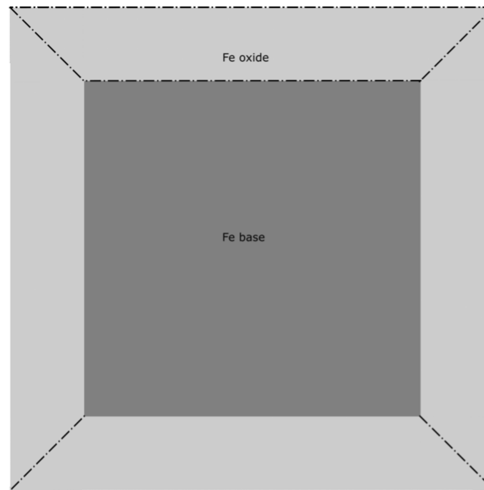

Fig. 4.8: 2D Schematic of the core base and oxide shell of the cubic NPs.

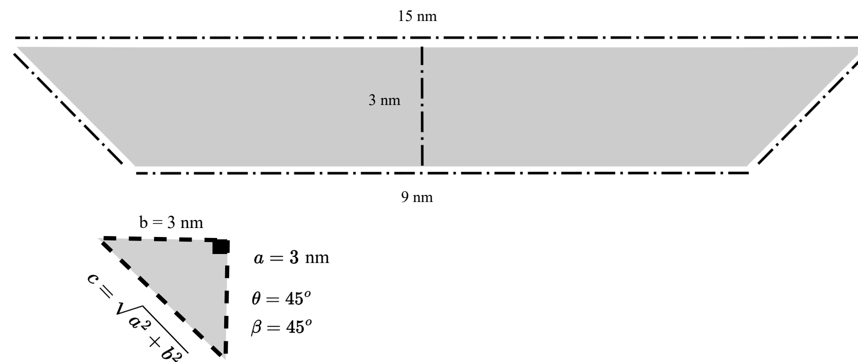

Fig. 4.9: Oxide shell segment chosen from the STEM image, as indicated in the red line in Fig. 4.7.

The remaining STEM images are shown in Appendix E in Figs E.1 - E.5, E.6. These STEM examples have lengths of 21.5 nm, 27 nm and 34 nm, respectively. The thickness of each case is 3 nm. Once the oxide shell's parameters have been determined, a 3D oxide shell can be generated in MATLAB®[32].

4.3 3D oxide shell model (truncated pyramid structure)

The 3D oxide shell model was created using a MATLAB® custom code [labelled Nanocarver [94]]. Models of crystalline NPs were generated with configurable crystal structure, shape, orientation and size. For this project the crystallographic structure of unit cell for Fe_3O_4 was used (space group Fd-3m) with characteristic parameter as shown in Table 4.1. This was used to generate the model of the crystalline oxide segment.

Table 4.1: Lattice parameters of Fe_3O_4 (magnetite) structure [21].

a = 0.83963 nm	b = 0.83963 nm	c = 0.83963 nm
$\alpha = 90^o$	$\beta = 90^o$	$\gamma = 90^o$

Table 4.2: shows the parameter used in the ''Nanocarver" code.

Model	L_t nm	L_b nm	h nm	$\approx \theta$	$\approx \beta$
1	15	9	3	45	45
2	14.5	9	3	47.49	42.51
3	14	9	3	50.19	39.81
4	13.5	9	3	53.13	36.87
5	13	9	3	56.31	33.69

Where the top L_t and bottom L_b lengths of the oxide segment correspond to the top and bottom lengths of the truncated pyramid in nm. The oxide shell's thickness h in nm. And angles defined by

$$\theta = \sin^{-1}\left(\frac{a'}{c'}\right) \tag{4.1}$$

$$\beta = \sin^{-1}\left(\frac{b'}{c'}\right) \tag{4.2}$$

whereas c' is the length of the truncated pyramid at the periphery. a' and b' are length as shown in Fig. 4.9.

To realise varying displacement fields for the model, a set oxide segment structures were created with truncation angles deviating from 45°. Stress fields on the side faces of these segments were applied such that they comply to an angle of 45° (described in section 4.4). Figure 4.10 shows the angles θ and β used to create a set of non-45° geometric structures. Figure 4.10 shows the relation between the "truncation length", namely the maximum distance between two non-45° segments and the corresponding truncation angle. For example, in the case of $\theta \approx 56.31^o$ and $\beta \approx 33.69^o$, the truncation length will be approximately 1 nm on each side. The larger this gap the higher the applied stress fields required for closing this gap.

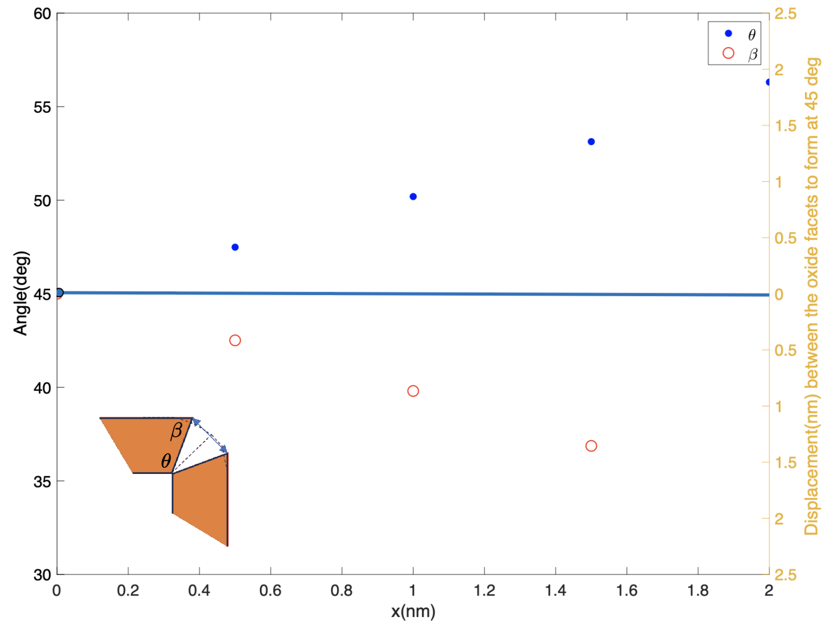

Fig. 4.10: Truncation angles for the oxide segment model vs. the truncation length.

The outcome results of the 3D oxide shell model creation is shown in Fig. 4.11(See Appendix E.2 for other non-45° structures).

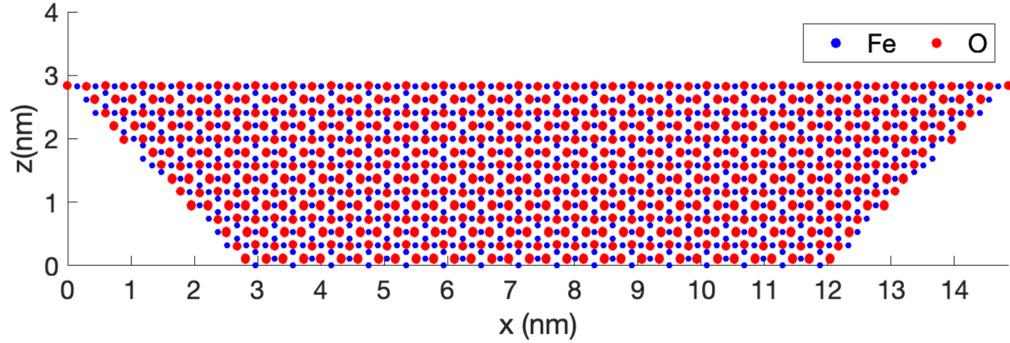

Fig. 4.11: Oxide shell for the 15 nm oxide NP with a magnetite crystal structure. A relaxed (45°).

4.4 Finite element method (FEM) simulation

COMSOL Multiphysics® [33] is a commercial software application designed to model realistic 3D strain or displacement fields. The COMSOL Multiphysics® software uses the finite element method (FEM) to address multi-physics problems such as mechanical structure problems and provides numerical solutions to various physics problems including strain[95, 96]. Complex physics problems, typically given as partial differential equations (PDEs), can be solved using the finite element method (FEM). Most physics problems can't be easily solved analytically, but they can be approximated by discretizing the equations that describe them; in this case, the PDEs used to approximate the 3D strain or displacement fields by discretized with a numerical solution that refers to the real solution[97].

COMSOL Multiphysics® is software that uses a solid mechanic module interface to investigate 2D and 3D structures[96]. The physical study variable, such as the displacement field components (u, v and w), is stationary and does not change over time[98]. As previously described the geometric structure used in the present case is a truncated pyramid composed of Fe_3O_4 representing the NP oxide shell. A sketch demonstrating the relaxed model geometry for the 15 nm case is shown in Fig. 4.12 with the top of the facet having a long side extension of 15 nm and 9 nm short side extension, and a thickness of 3 nm and a truncation angle of 45°.

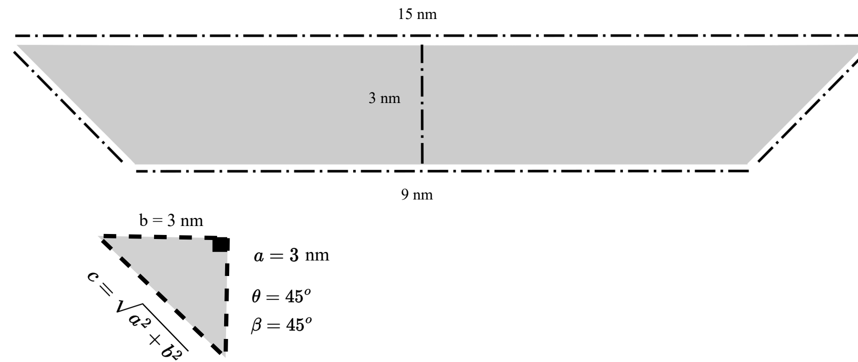

Fig. 4.12: The oxide shell dimension. The triangle properties were used to calculate the model.

To generate a realistic displacement field correlated with a model whose structure is a truncated pyramid, it is necessary to briefly describe the cubic oxide-shell geometric properties. The cubic structure consists of a central iron core and six truncated (oxide) pyramids, one of them is previously indicated in Fig. 4.12. In the ideal construction of the cubic NP, the six truncated pyramids should be at a 45-degree angle to produce a cubic structure, as seen in Figs 4.13 and 4.14A.

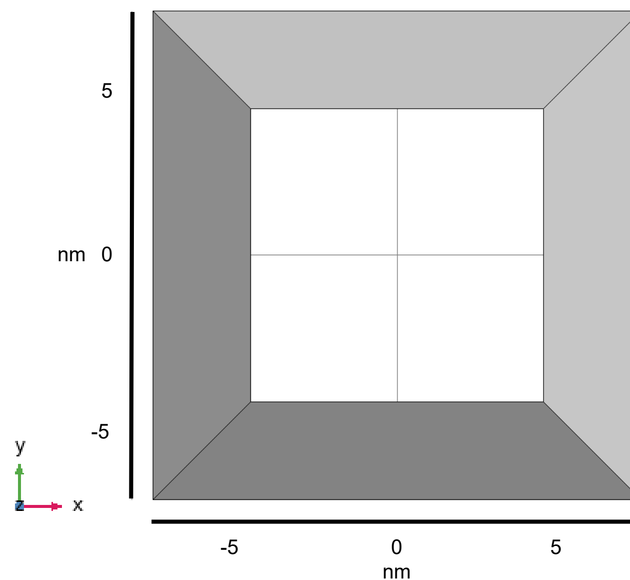

Fig. 4.13: Schematic represents the cubic structure of four truncated pyramids. The schematic is a presentation of the oxide layers at $\theta = \beta = 45^o$. Figure produced from COMSOL Multiphysics® software.

The assumption is to generate a non-45° truncated pyramid structure model as

sketched in Figs.4.14 B, E.11, E.12 and E.13 and then apply a stress field to form a side face angle of 45° as depicted in Fig. 4.14A. Physically, the stress fields are related to the energetically unstable gap configuration making it more favourable to create a 45° side facet angle and leading to strong distortions around the triple junction caused by three segments coming together to form this grain boundary[99]. Based on this assumption segments with increasing truncation angles were generated to explore the impact on the overall strain fields and hence atomic displacements and consequently Z-contrast image formation. Table 4.3 summarises the input parameters for five geometry structures used for finite element simulations.

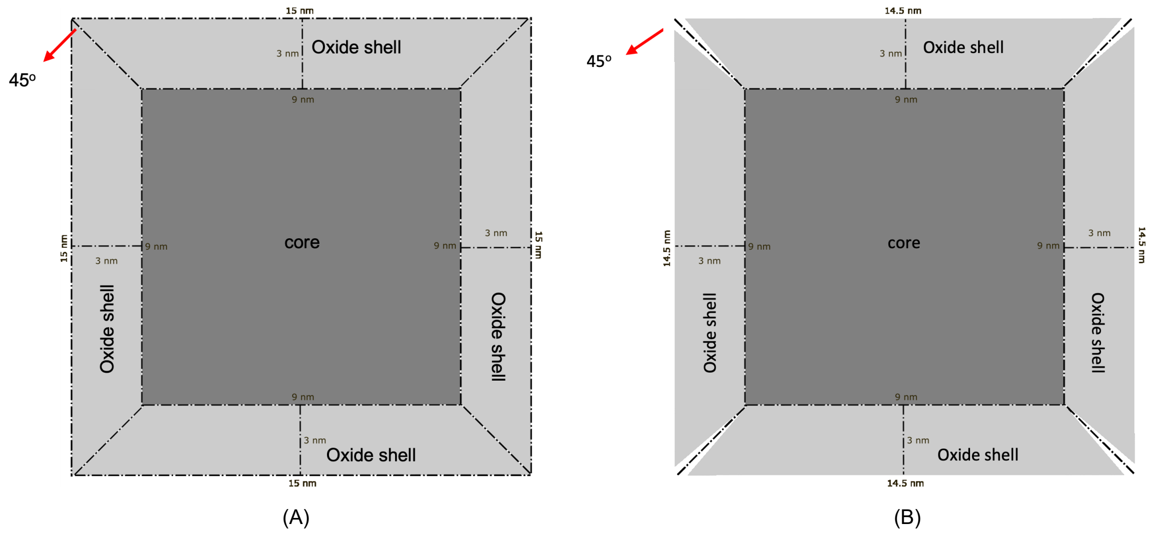

Fig. 4.14: (A) 45° geometric structure model. The angles are $\theta = 45^o$ and $\beta = 45^o$. The drawing depicts the core-shell structure of the oxide model. This demonstration displays four oxide shells.(B)non-45° case before applying external stress. The angles are $\theta = 47.49^o$ and $\beta = 42.51^o$.

Table 4.3: shows the parameter used for 15 nm model.

Model	L_t nm	L_b nm	Ratio	h nm	$\approx \theta$	$\approx \beta$	$\approx \Delta\theta$	$\approx \Delta\beta$	d nm	α
1	15	9	0.6	3	45	45	0	0	0	0
2	14.5	9	0.62	3	47.49	42.51	-2.49	2.49	0.5	4.78
3	14	9	0.64	3	50.19	39.81	-5.19	5.19	1	9.56
4	13.5	9	0.67	3	53.13	36.87	-8.13	8.13	1.5	14.34
5	13	9	0.69	3	56.31	33.69	-11.31	11.31	2	19.12

Where the top L_t and bottom L_b lengths of the oxide segment correspond to the top and bottom lengths of the truncated pyramid in nm. The oxide shell's thickness h in nm. The ratio is the ratio between the top and bottom diameters of the truncated pyramid, and the angle α applied is the angle required for the model to form 45° in the COMSOL Multiphysics® [96] software. $\Delta\theta$ and $\Delta\beta$ are the angle differences between the model without displacement and the model with displacement. d is displacement required to form a 45-degree angle (to close the gap between the oxide facets). Model mechanical properties such as Young modulus, Poisson ratio, and density, are shown in Table 4.4 [100].

Table 4.4: Model mechanical properties of Fe_3O_4 used in COMSOL Multiphysics® software.

Description	Value
Young's modulus	230.33GPa
Poisson's ratio	0.2616
density	5150kg/m^3

4.4.1 Condition for Displacement Field Model

The described displacement condition was applied to the four side faces of the model, as shown on in Fig. 4.15A. The described displacement condition has the ability to control displacement in several directions which is the reason of using it. The displacement field in this instance can be described as follows [101].

$$H\mathbf{u} = R \tag{4.3}$$

whereas H matrix in the case of the xx component as follows

$$H = \begin{bmatrix} 1 & 0 & 0 \\ 0 & 1 & 0 \\ 0 & 0 & 1 \end{bmatrix} \tag{4.4}$$

and

$$\mathbf{u} = \begin{bmatrix} u \\ v \\ w \end{bmatrix} \tag{4.5}$$

whereas **u** is displacement in u, v, w components in x, y and z directions, respectively.

$$R = \begin{bmatrix} R_x \\ R_y \\ R_z \end{bmatrix} \tag{4.6}$$

with R_x , R_y, and R_z being the components of R in x, y and z, respectively.

In the discussed case, the displacement field was applied to side facet as shown in Fig. 4.15A. To achieve this criteria, the model must be rotated and displaced around the R_z vector. As result, Eq. 4.3 can be written as follows

$$\begin{bmatrix} 1 & 0 & 0 \\ 0 & 1 & 0 \\ 0 & 0 & 1 \end{bmatrix} \begin{bmatrix} u \\ v \\ w \end{bmatrix} = \begin{bmatrix} R_x = 0 \\ R_y = 0 \\ R_z = \alpha \times |z| \end{bmatrix} \tag{4.7}$$

where is α is the angle applied to the model, and z is the spatial coordinates in the z-direction of the model before the displacement.

Equation 4.7 represents the xyz-components of the displacement in the model and its dependence on the truncation angle (α). α is the applied to the model to form 45 degree which are shown in Table 4.3. A screenshot of parameters used to calculate the rotation and displacement around $z-$direction is shown in Fig. 4.16. For the bottom facet of the oxide segment a fixed boundary condition was chosen, as indicated in Fig. 4.15B since the experimental observation indicates that no displacement is found at the oxide/core interface. For the top facet a free boundary condition was applied, reflecting the fact that the surface of the oxide segment is not experiencing constraints during the oxidation process.

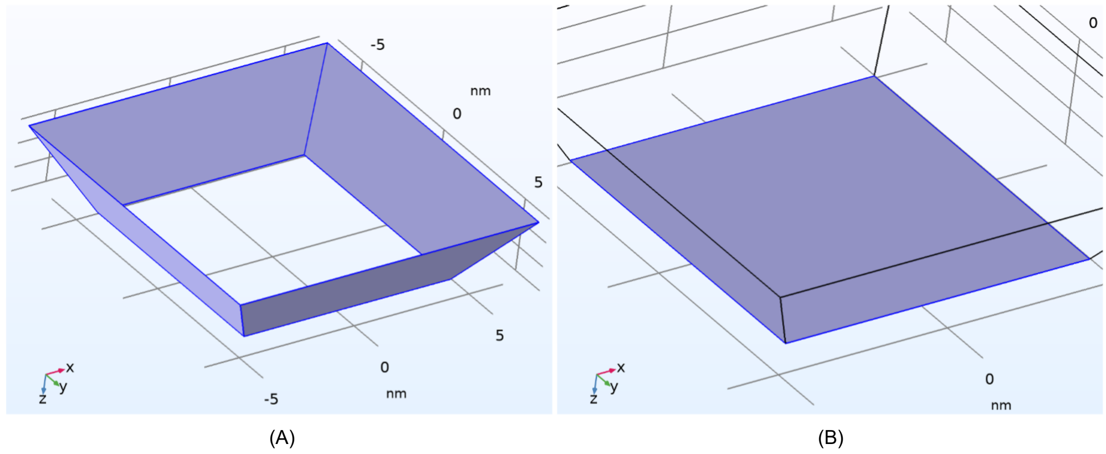

Fig. 4.15: A)The condition applied to the model. The described displacement condition was applied to the four facets. (B) The condition applied to the model. The conditions of the fixed condition applied to bottom facet. Figure produced from COMSOL Multiphysics® software.

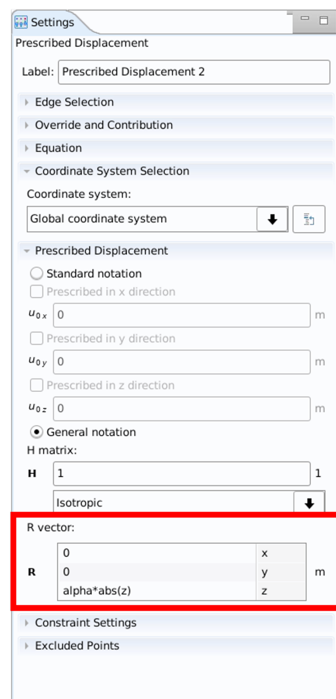

Fig. 4.16: Screenshot from COMSOL Multiphysics® software showing the input parameter of equation 4.6.

4.4.2 Finite Element Simulations

The results for the displacement fields calculated with Eq. 4.7 using the COMSOL Multiphysics®-based FES models are shown in Figs 4.17-4.20. As expected, the displacement field is maximal at the periphery while close to zero near the bottom (core-shell boundary). The displacement also increases from the bottom up to the top of the model. The colour bar shows the displacement required for 45° angle formation. The model diameter is 3 nm, the core-shell interface (bottom facet) is 9 nm, and the top length is 15 nm after applying the angle. The 1D displacement magnitude (nm) of the 3D model is shown in Fig. 4.21. The line profile was taken from the top of the model as shown in Fig. 4.25A.

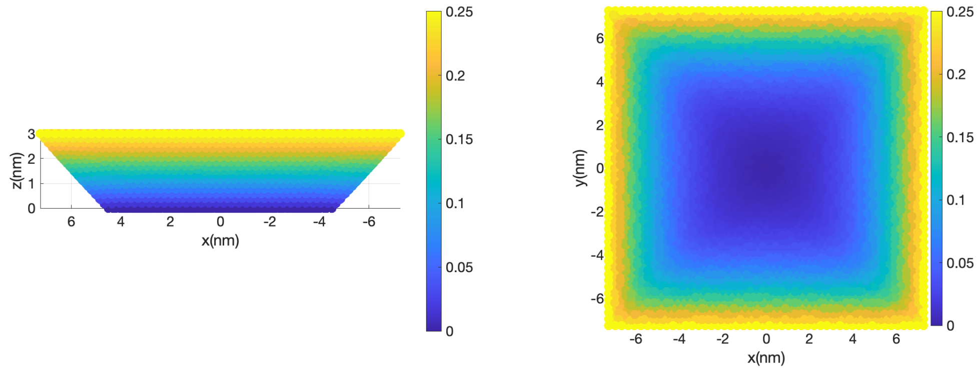

Fig. 4.17: The displacement profile shows how the model deforms at $\alpha = 4.78^o$. The colour bar shows the displacement needed for a 45° angle formation. The top length is 14.5 nm **before** the displacement and the thickness is 3 nm.

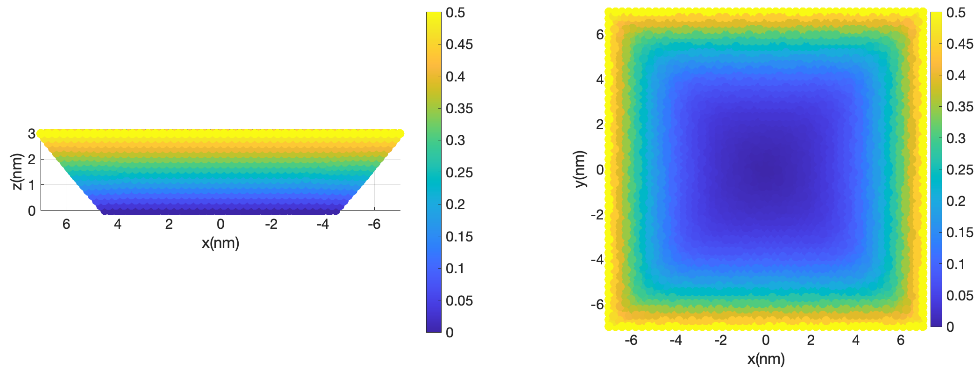

Fig. 4.18: The displacement profile shows how the model deforms at $\alpha = 9.56^o$. The colour bar shows the displacement needed for 45° angle formation. The top length is 14 nm **before** the displacement and the thickness is 3 nm.

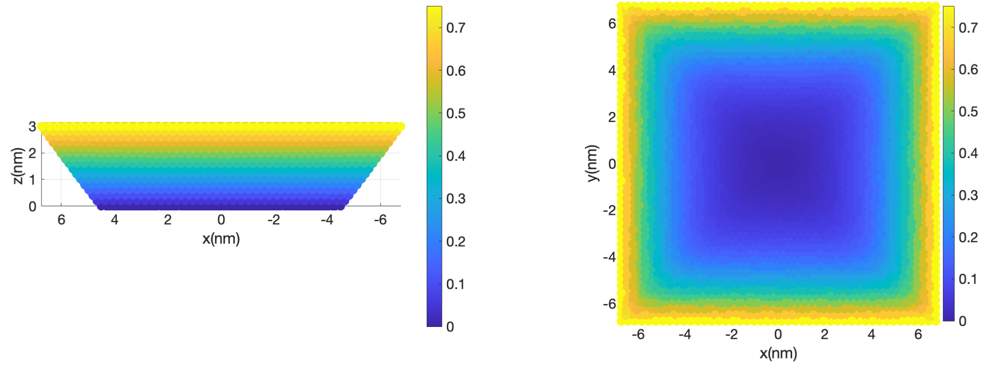

Fig. 4.19: The displacement profile shows how the model deforms at $\alpha = 14.34^o$. The colour bar shows the displacement needed for 45° angle formation. The top length is 13.5 nm **before** the displacement and the thickness is 3 nm.

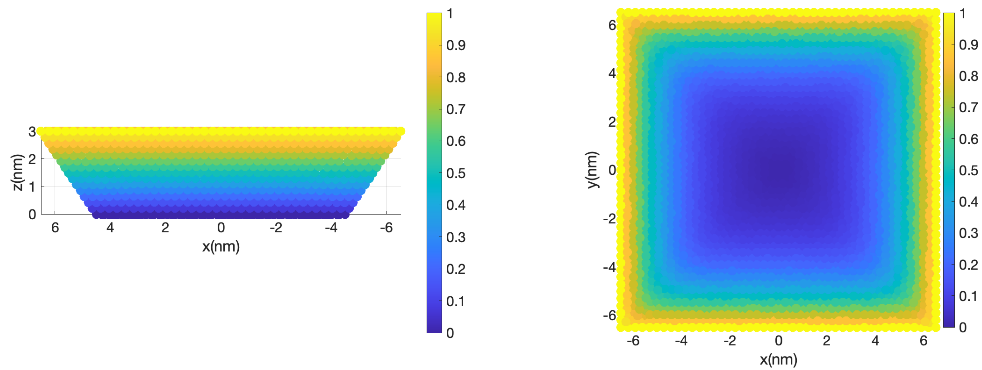

Fig. 4.20: The displacement profile shows how the model deforms at $\alpha = 19.12^o$. The colour bar shows the displacement needed for 45° angle formation. The top length is 13 nm **before** the displacement and the thickness is 3 nm.

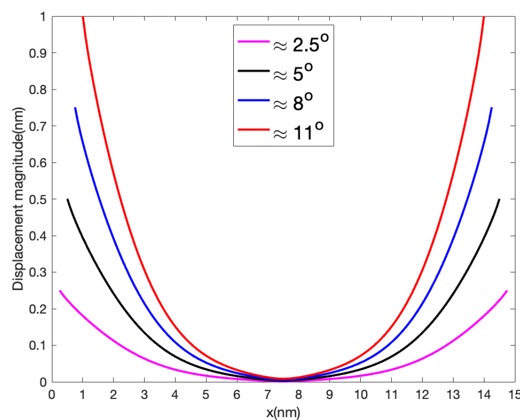

Fig. 4.21: Line graph of the displacement magnitude (nm) of the model top facet.

Aside from the displacement field results obtained from COMSOL Multiphysics® software, I also simulate the continuum strain tensor from the models. The reason for simulating the strain tensor is to visualize the strain tensor before applying it to the atomic structure of Fe_3O_4. The equation to represent the strain tensors used in COMSOL Multiphysics® software is as the follows [102, 103].

$$\varepsilon = \begin{bmatrix} \varepsilon_{xx} & \varepsilon_{xy} & \varepsilon_{xz} \\ \varepsilon_{yx} & \varepsilon_{yy} & \varepsilon_{xz} \\ \varepsilon_{zx} & \varepsilon_{zy} & \varepsilon_{zz} \end{bmatrix} \tag{4.8}$$

whereas the ε_{xx},ε_{yy} and ε_{zz} are tensor strain components which are represented by the following equations

$$\varepsilon_{xx} = \frac{\partial u_x}{\partial X} = \frac{Lx_f - Lx_o}{Lx_o} = \frac{\Delta Lx}{Lx_o} \tag{4.9}$$

$$\varepsilon_{yy} = \frac{\partial u_y}{\partial Y} = \frac{Ly_f - Ly_o}{Ly_o} = \frac{\Delta Ly}{Ly_o} \tag{4.10}$$

$$\varepsilon_{zz} = \frac{\partial u_z}{\partial Z} = \frac{Lz_f - Lz_o}{Lz_o} = \frac{\Delta Lz}{Lz_o} \tag{4.11}$$

where L_o is the original length and L_f is the final length after strain is applied, while ε_{xy}, ε_{xz} and ε_{yz} are shear strain components, which are represented by the following equations:

$$\varepsilon_{xy} = \frac{1}{2}\left[\frac{\partial u_x}{\partial X} + \frac{\partial u_y}{\partial Y}\right] \tag{4.12}$$

$$\varepsilon_{xz} = \frac{1}{2}\left[\frac{\partial u_x}{\partial X} + \frac{\partial u_z}{\partial Z}\right] \tag{4.13}$$

$$\varepsilon_{yz} = \frac{1}{2}\left[\frac{\partial u_y}{\partial Y} + \frac{\partial u_z}{\partial Z}\right] \tag{4.14}$$

The 2D strain tensor of ZZ component is shown in Fig. 4.22 for the 15 nm case. The illustration depicts the 2D surface plot of the 3D strain model for the variances of the strain value. The 2D surface plane was taken from the centre of the 3D model as in Fig. 4.23. Figure 4.22A is the lowest strain tensor, which is around 3 % and

the compression strain around 4.5 %, while the high strain value is as shown in Fig. 4.22D. The strain is around 12.6 % and compression strain is around 1.6 %.

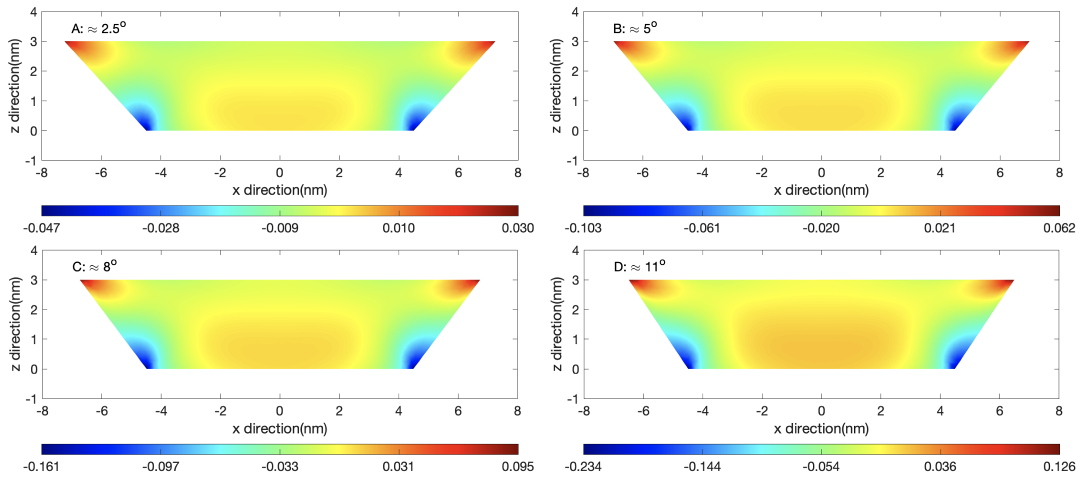

Fig. 4.22: The surface of continuum strain profile of the ZZ component (1). Differences in angle ($\beta = -\theta$) values between the model without displacement and the model with displacement.

The compression (as shown in the blue area in Fig. 4.22) results from the model bottom's fixed condition, where the interface is between the core-shell. Due to how the COMSOL Multiphysics® software generates strain, the results are infinite linear strain to the whole model. It is important to note that the red region in the 2D plot represents a region of **bending** in the model that will be evident in the simulated images (see Chapter 5).

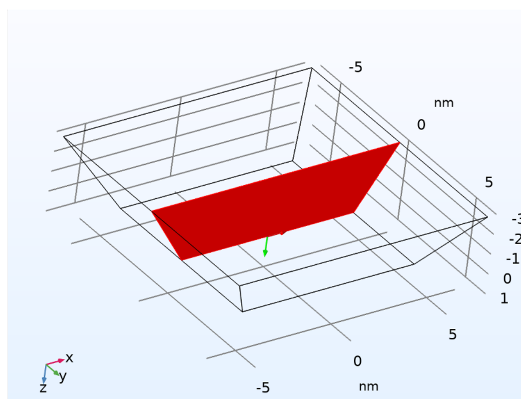

Fig. 4.23: The 2D surface plane cut from the centre of the 3D model. The image was produced using COMSOL Multiphysics® software.

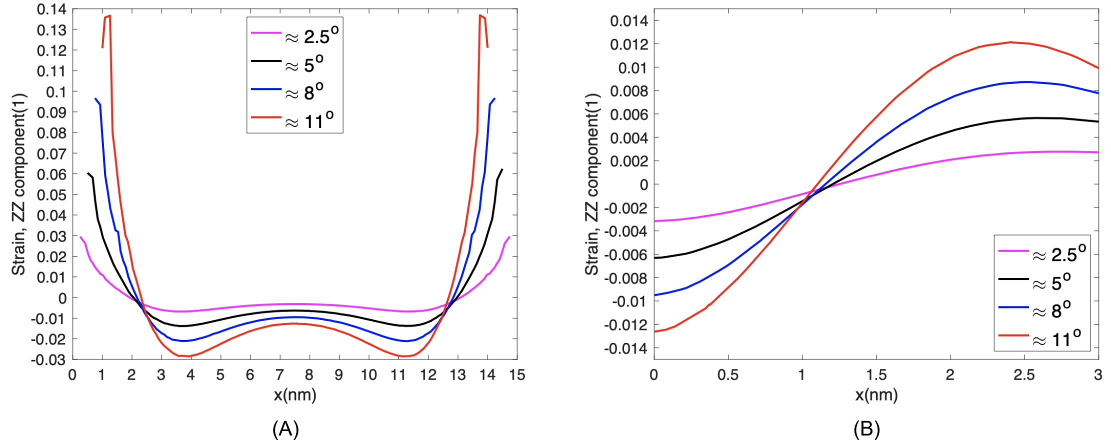

Fig. 4.24: (A) Strain tensor, ZZ component, of line profile as shown in Fig. 4.25A. (B)Strain tensor, ZZ component, of line profile as shown in Fig. 4.25B. Angles here is the $\theta = \beta$.

The 1D strain tensor of the ZZ component of the 15 nm case is depicted in Fig. 4.24B as additional evidence obtained from COMSOL Multiphysics®. As shown in Fig. 4.25B, the strain profile was measured from the centre to the top of the model. The magenta colour represents the lowest value of the displacement field (see Table 4.2), and the angle difference is $\approx 2.5^o$. The strain tensor value is around 0.1 %. In contrast, the displacement field and strain tensor are greater when the angles are around $\approx 11^o$, as indicated by the red colour. Another line profile from the top of the model as shown in Fig. 4.25 to get the strain tensor of strain tensor of the ZZ component of the 15 nm case is shown in Fig. 4.24A.

The case 15 nm is not the only one I was investigated, I looked at different sizes, for example, case 21.5 nm, case 27 nm, and case 34 nm. Tables 4.5-4.7 are showing the parameter used for COMSOL Multiphysics® software for case 21.5 nm, 27 nm and 34nm, respectively. The comparison of the 1D strain tensor of the ZZ component in all cases is depicted in Fig. 4.26. The graph depicts only models of $\approx 11^o$ cases in model 15 nm, model 21.5 nm, model 27 nm, and model 34 nm, which correspond to the highest displacement field applied to the models, as indicated in Tables 4.3,4.5,4.6 and4.7. The strain tensor in Fig. 4.26 relates to the size of the model. It is clear that the size of the model shows more relaxing area (almost free strain) in compared to the small model which will be discussed in Chapter 5.

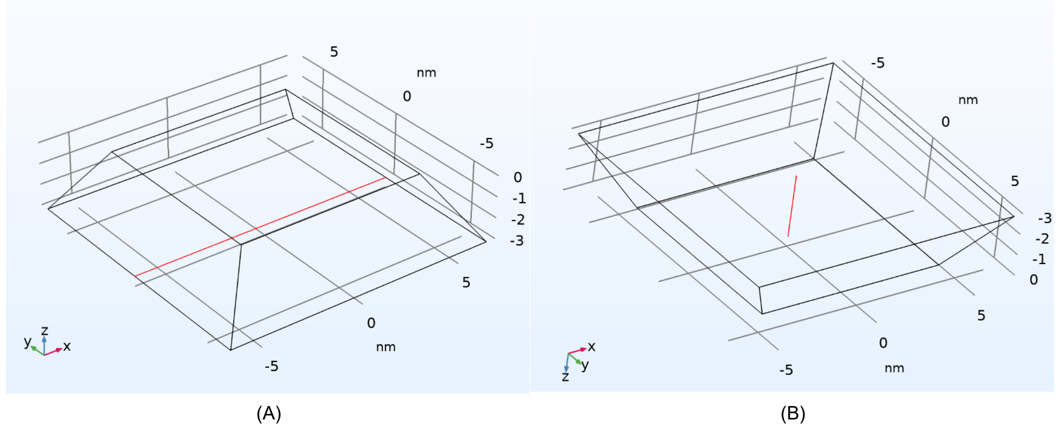

Fig. 4.25: 1D depiction of the 3D model's cut line in COMSOL Multiphysics ® software. (A) is from the top and the (B) is from the centre.

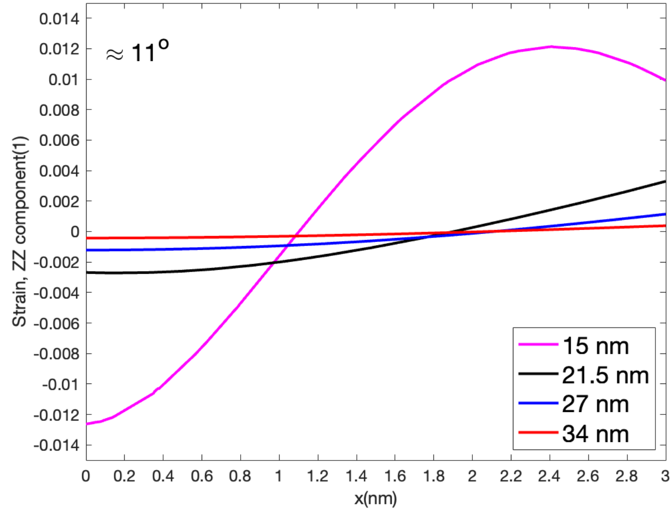

Fig. 4.26: comparison of the 1D strain tensor of the ZZ component for 15 nm, model 21.5 nm, model 27 nm, and model 34 nm.

Table 4.5: Shows the parameters used for the 21.5 nm model.

Model	L_t	L_b	Ratio	h nm	$\approx \theta$	$\approx \beta$	$\approx \Delta\theta$	$\Delta\beta$	d nm
1	21.5	15.5	0.721	3	45	45	0	0	0
2	21	15.5	0.738	3	47.49	42.51	-2.49	2.49	0.5
3	20.5	15.5	0.756	3	50.19	39.81	-5.19	5.19	1
4	20	15.5	0.775	3	53.13	36.87	-8.13	8.13	1.5
5	19.5	15.5	0.795	3	56.31	33.69	-11.31	11.31	2

Table 4.6: Shows the parameters used for the 27 nm model.

Model	L_t	L_b	Ratio	h nm	$\approx \theta$	$\approx \beta$	$\approx \Delta\theta$	$\approx \Delta\beta$	d nm
1	27	21	0.78	3	45	45	0	0	0
2	26.5	21	0.79	3	47.49	42.51	-2.49	2.49	0.5
3	26	21	0.81	3	50.19	39.81	-5.19	5.19	1
4	25.5	21	0.82	3	53.13	36.87	-8.13	8.13	1.5
5	25	21	0.84	3	56.31	33.69	-11.31	11.31	2

Table 4.7: Shows the parameters used for the 34 nm model.

Model	L_t	L_b	Ratio	h nm	$\approx \theta$	$\approx \beta$	$\approx \Delta\theta$	$\approx \Delta\beta$	d nm
1	34	28	0.824	3	45	45	0	0	0
2	33.5	28	0.836	3	47.49	42.51	-2.49	2.49	0.5
3	33	28	0.848	3	50.19	39.81	-5.19	5.19	1
4	32.4	28	0.861	3	53.13	36.87	-8.13	8.13	1.5
5	32	28	0.875	3	56.31	33.69	-11.31	11.31	2

4.4.3 Application of displacement field to the Fe_3O_4 structure

Based on the size of the experimental images, finite element simulation COMSOL Multiphysics® software [33] is used to make the displacement field. The output data (txt file format) contains information about the source data (spatial coordinate data for x, y and z) and the shift data (the vector data correlated to the spatial coordinates). Another x, y and z file contains information about the NP structure, such as the atom positions and symbols, and that file was obtained from the "Nanocarver" [94] code. The data is then interpolated using a built-in function called scatteredInterpolant [104]. The function is interpolated at each spatial coordinate with its correlated vector field and the x, y and z data. The objective is to identify the displacement field to use with the fixed atomic structure data of Fe_3O_4. Figures

4.27 - 4.31 show the displacement field applied to the Fe_3O_4 structure for the 15 nm case. The angle after applying the displacement field is 45°.

In summary, the 3D mode and 3D displacement field model were created using factors from different sizes of experimental images, such as the size of the NPs and the oxide shell. The NPs' structure and a realistic displacement field were created using MATLAB® [32] code and COMSOL Multiphysics® software. The interpretation of the displacement field vector was enforced by utilising the scatterdInterpolant function built into MATLAB® [32].

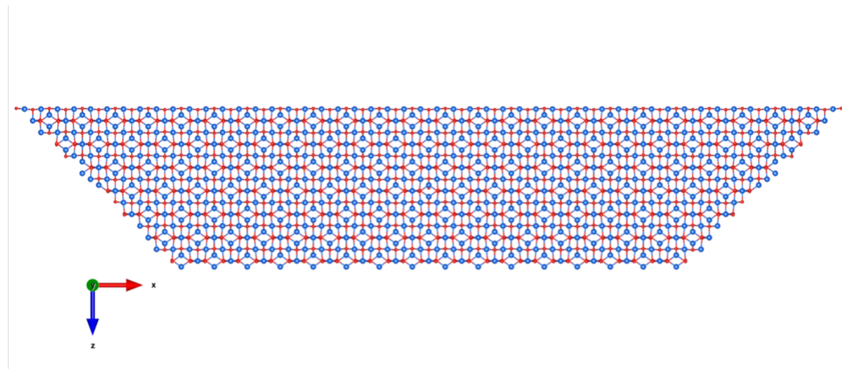

Fig. 4.27: Angle before and after applying the displacement field: $\theta \approx 45^o$ and $\beta \approx 45^o$. Red: iron atoms, blue: oxygen atoms.

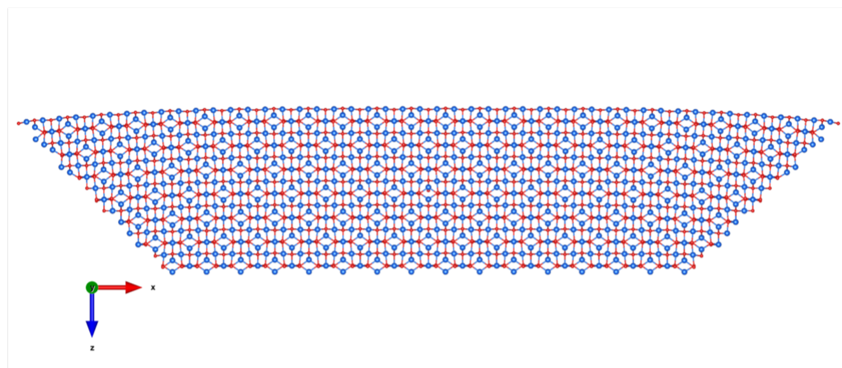

Fig. 4.28: Model's angle before applying the displacement field: $\theta \approx 47.49^o$ and $\beta \approx 42.51^o$. Angle after applying the displacement field: $\theta \approx 45^o$ and $\beta \approx 45^o$. Red: iron atoms, blue: oxygen atoms.

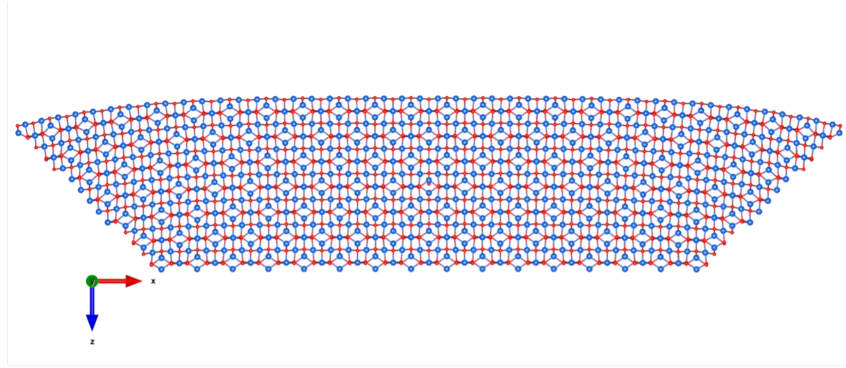

Fig. 4.29: Model's angle before applying the displacement field: $\theta \approx 50.19^o$ and $\beta \approx 39.81^o$. Angle after applying the displacement field: $\theta \approx 45^o$ and $\beta \approx 45^o$. Red: iron atoms, blue: oxygen atoms.

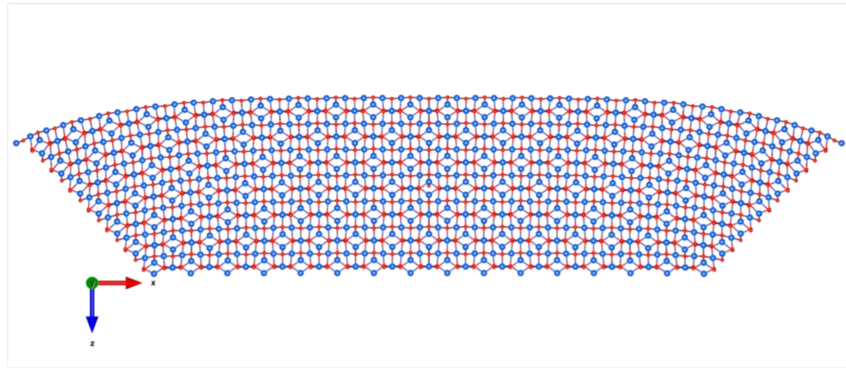

Fig. 4.30: Model's angle before applying the displacement field: $\theta \approx 53.31^o$ and $\beta \approx 36.87^o$. Angle after applying the displacement field: $\theta \approx 45^o$ and $\beta \approx 45^o$.Red: iron atoms, blue: oxygen atoms.

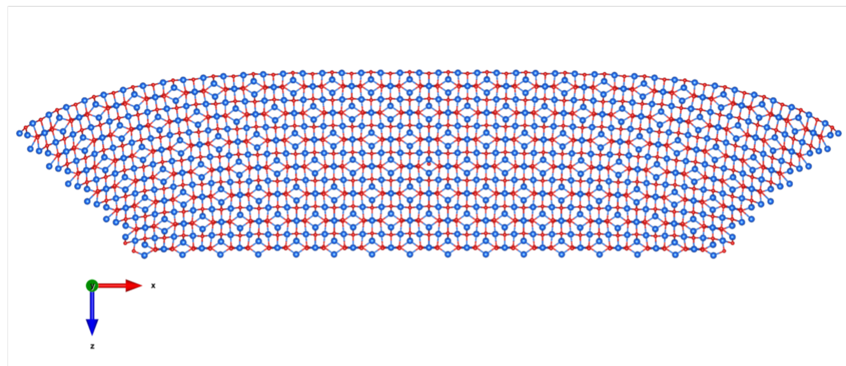

Fig. 4.31: Model's angle before applying the displacement field: $\theta \approx 56.31^o$ and $\beta \approx 33.69^o$. Angle after applying the displacement field: $\theta \approx 45^o$ and $\beta \approx 45^o$. Red: iron atoms, blue: oxygen atoms.

4.5 Simulation approach

STEM images were simulated using Quantitative TEM/STEM Simulations (QSTEM) software [15]. The simulation employs the multislice method (the image computing method is mentioned in Appendix F). The simulation was conducted using a supercomputer (Viking Cluster) at the University of York [105].

The QSTEM simulation parameters are shown in Tables 4.8 and 4.9. I used two sets of parameters since the experimental data came from two different microscopy instruments. The experimental images of 21.5 nm, 27nm and 34 nm were taken in Daresbury's *SuperSTEM* by Dr Demie (Despoina Maria) Kepaptsoglou [84]. While the image of 15 nm was taken in *The York JEOL Nanocentre* at the University of York by Dr. Leonardo Lari [106].The NPs were prepared and imaged from two different cluster sources and underwent oxidation over similar time intervals.

Table 4.8: simulation parameter used in QSTEM for the model of 15 nm.

Voltage (kV)	Defocus (nm)	Astigmatism (nm)	C3 (mm)	Cc (mm)	dE (eV)	TDS	Detector(mrad)
200	0	0	0	1.2	0.8	50	110-180

Table 4.9: simulation parameter used in QSTEM for models of 21.5 nm, 27nm and 34 nm size length.

Voltage (kV)	Defocus (nm)	Astigmatism (nm)	C3 (mm)	Cc (mm)	dE (eV)	TDS	Detector(mrad)
100	0	0	0	1.2	0.3	50	90-200

The simulation results of multislice Z-contrast images of Fe_3O_4 are shown in Fig. 4.32, for a model with a thickness of 3 nm and a length of 15 nm. The edges reveal some missing atoms (as shown in Fig. 4.32) as a result of the model being sliced based on the required quantity. For example, the number of atoms, such as the 45-degree slice cut angle and non- 45-degree slice cut angle. The first set of images Fig. 4.32A,F,G are non-displaced model. The other set of images in Fig. 4.32 are displacement model with different values, as shown in Fig. 4.33. It is clear that the models are not in periodic boundary condition. This is due to the cutting angle used when creating the model. As a result, I added ≈ 3 nm vacuum spaces around the model to minimise the impact of the periodic boundary condition. Appendix G

shows more simulated image for other sizes such as 21.5 nm, 27nm and 34 nm.

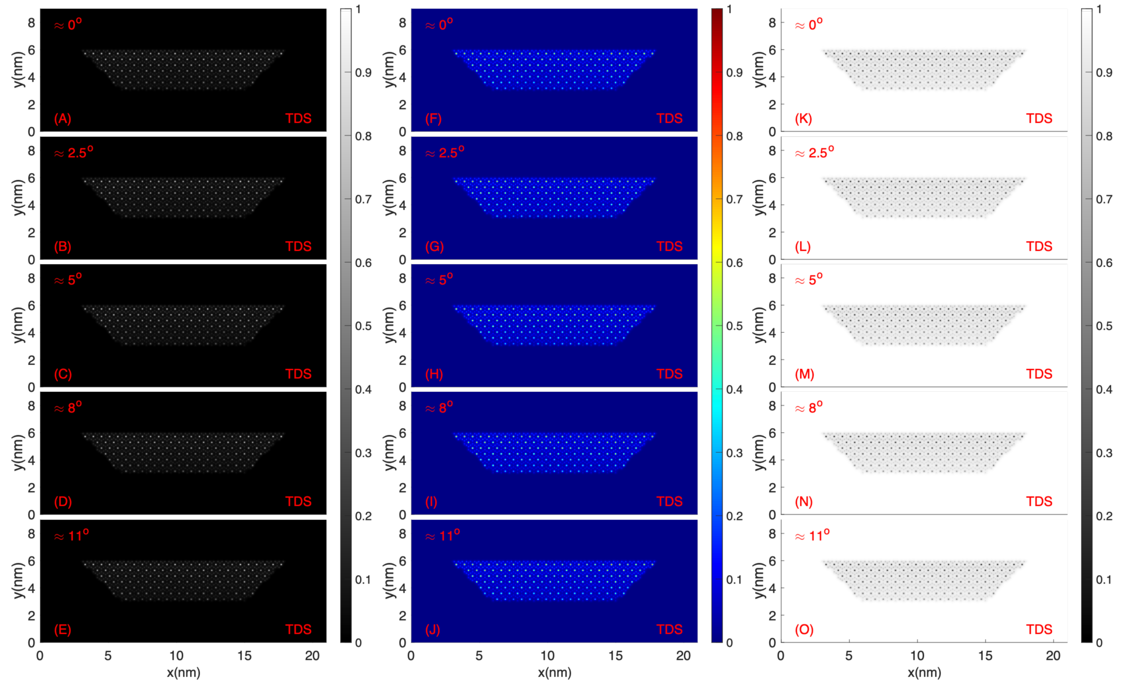

Fig. 4.32: Multislice simulated Z-contrast images for model 15 nm of Fe_3O_4. Fe^{2+} columns correlate to high-intensity maxima, while Fe^{3+} columns correspond to low-intensity maxima.The angles diffidence are state in each image as $\beta = -\theta$. The 1st columns (A,B,C,D,E) are dark field (DF) images. The 2nd column (F,G,H,I,J) are false-colored of DF images. The 3rd column (K,L,M,N,O) are corresponding the bright field images (BF).

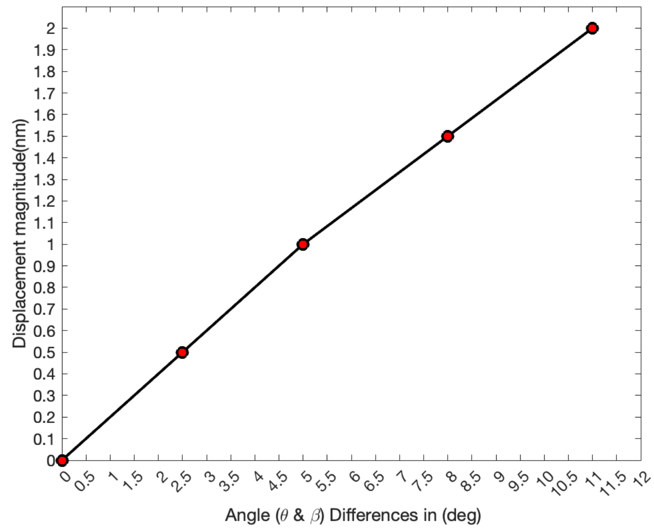

Fig. 4.33: Plot depicts the angle differences (α and β as in Table 4.3) used to generate the model in relation to the displacement magnitude.

Chapter 5

Displacement field impact on the STEM images

5.1 Introduction

Atomic displacement fields, which can be caused e.g. by local defects or external strain fields, have a significant effect on Z-contrast imaging. This impact is due to the local disorder leading to variations of atomic positions in the electron beam direction and affects both the positions and intensity of atomic columns in the resulting images. The main focus of this thesis lies on a better quantitative understanding of the correlation between the displacement fields in the oxide shell of Fe/Fe_3O_4 nanoparticles, as discussed in Chapter 1 section 1.1.1, and both the intensities and positions (and hence displacement fields) of the atomic columns. For this purpose, this chapter is concentrating on two model truncated pyramid shaped oxide segments, one with long-edge length of 15 nm (Model I) and one with 34 nm (Model II). These two cases were chosen since they represent typical dimensions found in the experimental samples. Further model dimensions were used for modelling and are covered in Appendices H (for intensity profiles) and I (for displacement fields). These models were used for Z-contrast multislice image simulations under varying strain fields as discussed in Chapter 4. To determine the impact of thermal diffuse scattering (TDS) image simulations for both non-TDS and TDS were performed. This approach was chosen to obtain a more accurate representation of the impact

of displacement fields on the electron scattering and hence image formation [107]. Atomic displacement field mapping for Model I and Model II will be investigated, which will help comprehend how the atomic displacement field influences the model geometry. The primary objective of this study is to quantify the correlation between the external stress (hence the atomic displacement in 3D) and the intensity distribution in the 2D Z-contrast images.

5.2 Results for Model I and II

The following results are intensity profiles of simulated images of multislice Z-contrast images for non-strained and strained model systems of the Fe_3O_4 domains. As discussed in Section 5.1 only two models, one with a 15 nm long edge (Model I) and one with a 34 nm long edge (Model II), will be presented in this section, while other models such as 21 nm long edge (Model III) and 27 nm long edge (Model IV) will be presented in Appendix H.

5.2.1 Intensity profiles for Model I

For the evaluation of the simulation results and the comparison with experimental data, image intensity profiles in x- and y-directions were acquired at specific locations, as indicated by arrows in Fig. 5.1. A central line profile in y-direction was determined in the centre of the domain (red arrow) and several line profiles in x-direction (arrows in magenta, brown, purple, and green) were taken.

Figure 5.1 shows the results of the image simulations for the unstrained and strained model values in y-direction for varying truncation angles (see in Chapter 4) for the simulated images using Model I. The respective line profiles given in Fig. 5.1 compare both the results with and without considering TDS.

Figure. 5.1A shows the unstrained model with the respective line profile shown in Fig. 5.2A. A gradient of intensity can be observed, which is expected as the number of Fe-ions (atoms) in beam direction increases with increasing y-value due to the truncated pyramid-shaped geometry of the domain and the dependence of the Z-contrast on the number of atoms along the beam direction. In the presence of stress

fields, the Z-contrast images as shown in Fig. 5.1B-E with the respective intensity profiles as shown in Fig. 5.2B-E. As can be seen in the profiles, the intensity of the bottom atomic column is now always lower than that of the top atomic column for all strain values in contrast to the unstrained case which can be explained by the disorder of the atoms in beam directions which increases with increasing strain [87].

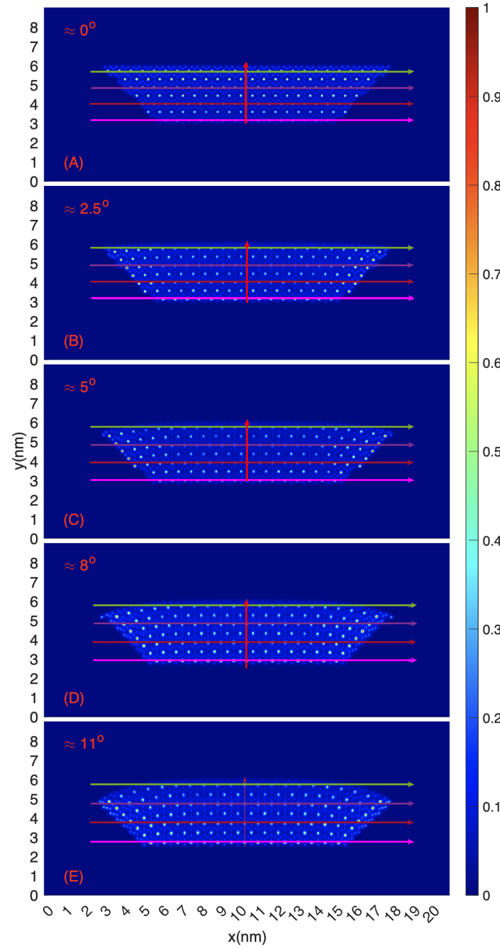

Fig. 5.1: Multislice (QSTEM) simulated normalised Z-contrast images obtained for a truncated pyramid geometry of Fe_3O_4 for different. Fe^{2+} columns correlate to high- intensity maxima, while Fe^{3+} columns correspond to lower intensity maxima between the Fe^{2+} columns. (A) represents the unstrained case, (B) corresponds to a 0.5 nm edge displacement, (C) 1 nm, (D) 1.5 nm, and (E) 2 nm. Coloured arrows show the line profile positions.

A second finding indicates that the strain distribution or displacement field influences not only the intensity of the simulated image, but also the position of each

column in simulated image. Comparing the non-displaced to the displaced models, for instance, reveals a local increase of the spacing of atomic columns as shown in Fig. 5.2.

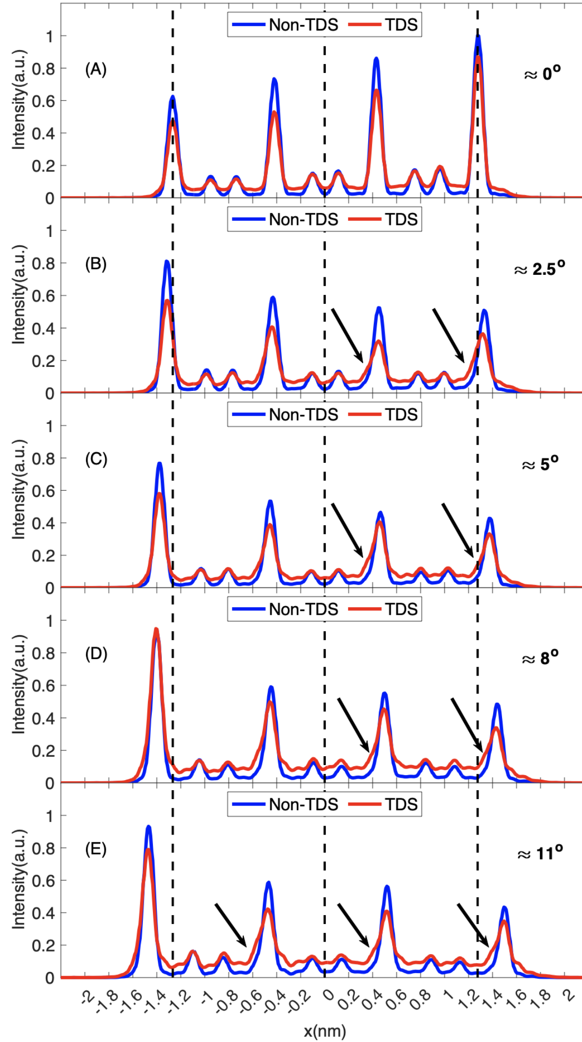

Fig. 5.2: Line profiles of simulations in Fig. 5.1 in y-axis direction. (A) shows the unstrained model, with (B-E) showing the results for the strained model. The truncation angle values for $\beta = -\theta$ are given in line with those provided in Fig. 4.33(see Chapter4). The black arrows point towards shoulders of the maxima. The dashed line indicates the peak positions according to the unstrained model.

Furthermore, the results of the image profile analyses reveal peak shape variations as a function of displacement. For instance, the strained models exhibit a loss of symmetry, which expresses itself as shoulders of the column intensity profiles, as pointed out by arrows in Fig. 5.2B-E. It becomes clear that these shoulders are

related to the displacement field. As an example, for the smallest truncation angle (Fig. 5.2B) there is a small shift in the shoulder near the top column maximum, whereas in Fig. 5.2E, there are significant shoulders found in the majority of the maxima, indicating that with an increase of truncation angle the resulting increasing displacement field has a stronger effect on the intensity distribution, as could be expected. This local variation of the column position will affect in turn the probability of lattice diffusion (see Chapter2).

As depicted in Fig. 5.2A, for the unstrained model using non-TDS, the peak shape does not significantly differ from the case where TDS is included. However, the peak intensities vary as the TDS leads to an increased background and lowered peak intensity as shown in Fig. 5.2A (red). Figures 5.2 B-E in contrast, demonstrate the effect of TDS on the peak intensities of the strained model indicating also pronounced anisotropic peak shapes with the increased occurrence of shoulders as the strain increases. This shows that the strain induced atomic disorder introduces anisotropic electron scattering behaviour of the individual atomic columns; this also expresses itself in the "reversal" of the absolute intensities in comparison to the unstrained case. Overall, the peaks for the unstrained situation exhibit largely a Gaussian distribution with the strained cases showing a pronounced non-Gaussian distribution which is enhanced by TDS. The lower peak intensities for the TDS cases are related to an increased number of electrons scattered anisotropically around the columns and into the background. Overall, a significant impact of TDS can be observed which is enhanced by the presence of lattice strain.

Figure 5.3 shows the intensity profiles in x-direction. As discussed in the context of Fig. 5.1 four positions were chosen for these profiles. The magenta-coloured line profile (Fig. 5.3A) indicates a lower local atomic displacement near the bottom edge of the domain (corresponding to the core-shell interface of the iron/iron oxide NP). When comparing the first line profiles of the unstrained model with the strained cases, the peaks shift, as expected, indicating increased spacing between the columns.

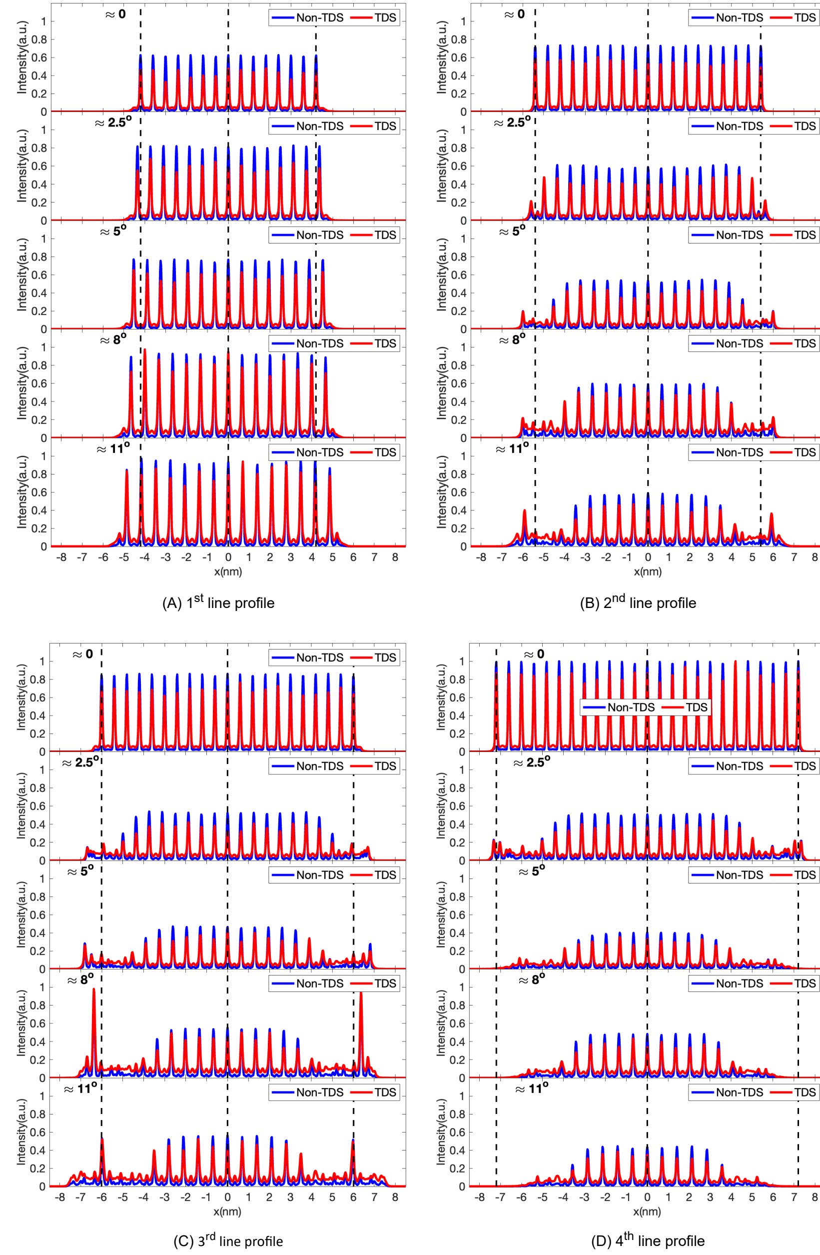

Fig. 5.3: Intensity profiles taken in the x-direction for Model I, as shown by the magenta, brown, purple, and green arrows in Fig. 5.1. The black dashed line indicates the peak positions according to the unstrained model. The zero angle is the non-displaced column. The angles difference are stated in each image in terms of $\beta = -\theta$.

Fig. 5.3B-D shows the line profiles along the brown, purple, and green lines in Fig. 5.1, respectively. Due to the increased level of strain in comparison to Fig. 5.3A, the intensity maxima on the line profiles vary. This behaviour is due to an increased

level of disorder of the atom arrangements in beam direction as well as a reduced contribution to the effective scattering of atoms near the edges in beam direction. The strain fields influence the atom columns, resulting in bending or curvature of the model structure. This is increasingly more pronounced in Figs.5.3B-D. The peaks at the periphery in Fig. 5.3C (as in the fourth- and fifth-line profiles in C) are due to the fact that atoms from adjacent columns contribute to the scattering due to the lattice plane bending. Interestingly, no apparent anisotropy of intensity distribution in the peaks is found in x-direction for all line profiles.

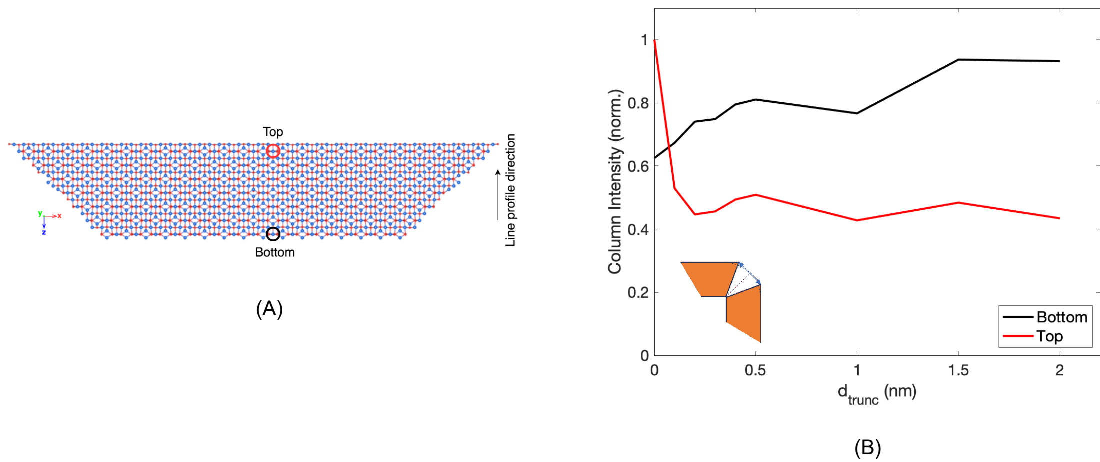

Fig. 5.4: (A) Model of the top segment of a cubic NPs' oxide shell with two selected columns at the top and bottom of the segment (Fe: blue, O: red). (B) Impact of the truncation angle on column intensities in the simulated images for the top and bottom column selected in (A). Insert shows schematic of the truncation angle impact on d_{trunc}.

The impact of atom displacement on image intensity is compared in Fig. 5.4 where the column peak intensity is tracked for different strain levels for one column at the top and one at the bottom of the domain as indicated in Fig. 5.4A. The image profile was captured along the column direction from two distinct positions, as shown in Fig. 5.4A. The results in Fig. 5.4B show that as the model displacement field increases, the intensity of the respective columns changes such that there is a gradual increase of intensity for the bottom column whereas the top column shows a massive decrease already for small strain values and subsequent further decrease as the strain increases [87].

5.2.2 Intensity profiles for Model II

To compare the smaller domain used for Model I with a larger model system a long edge length of the truncated pyramid of 34 nm (Model II) was used with the image simulation results presented in Fig. 5.5.

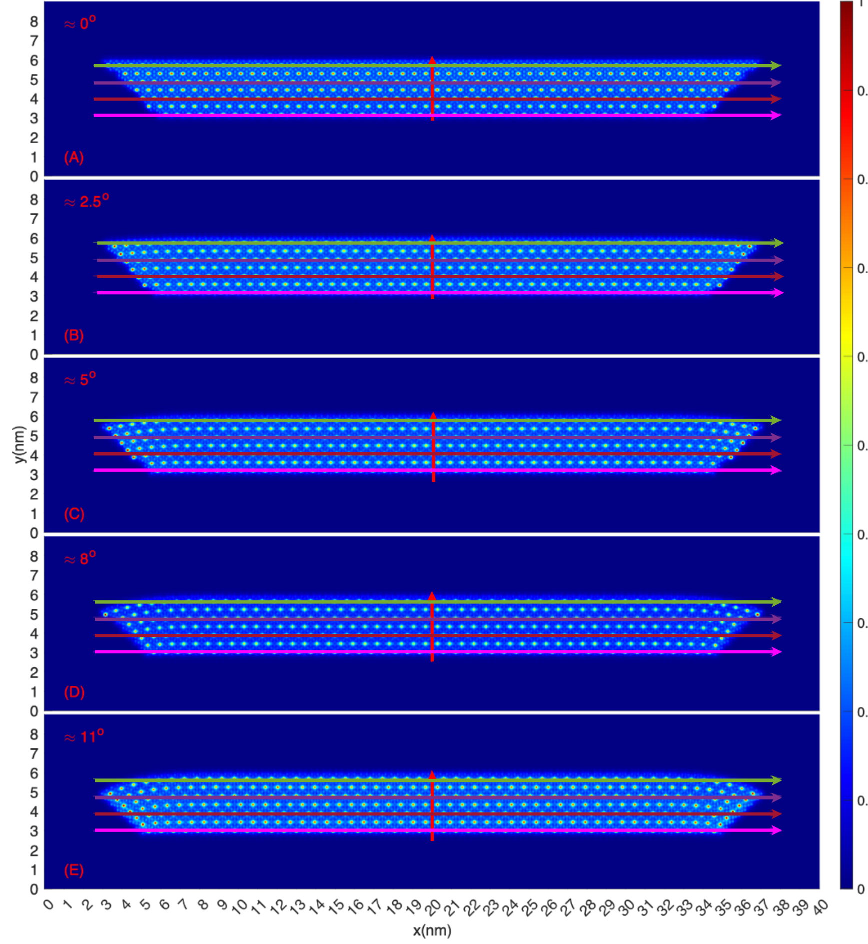

Fig. 5.5: Multislice (QSTEM) simulated normalised Z-contrast images of Fe_3O_4 for Model II. Fe^{2+} columns correlate to high- intensity maxima, while Fe^{3+} columns correspond to low-intensity maxima. The angles difference are stated in each image as $\beta = -\theta$. (A) represents the unstrained case, (B) corresponds to a 0.5 nm edge displacement, (C) 1 nm, (D) 1.5 nm, and (E) 2 nm. Coloured arrows show the line profile positions.

Like the approach for Model I line profiles in y- and x-direction were determined as shown in Figs. 5.6 and 5.7. The respective positions for the line profiles are denoted by arrows in Fig. 5.5. In the unstrained and strained models, the slope of

the image intensity gradient is qualitatively comparable to the 15 nm model (Model I) due to overall geometric similarities, as indicated in Fig. 5.6. However, the gradient in Model II is reduced compared to Model I due to its larger size which is related to the larger number of atoms along the trajectory direction of the beam for this system [87]. Consequently, there is less variance in intensity between a strained region and one that is free of strain [37].

In addition, the variation of spacing between the maxima is not identical for both models, as expected. The strain induced by the assumption of a "forced rotation" of the segments' side facets to close the truncation angle does not affect the centre region of the segment as much as in the Model I case.

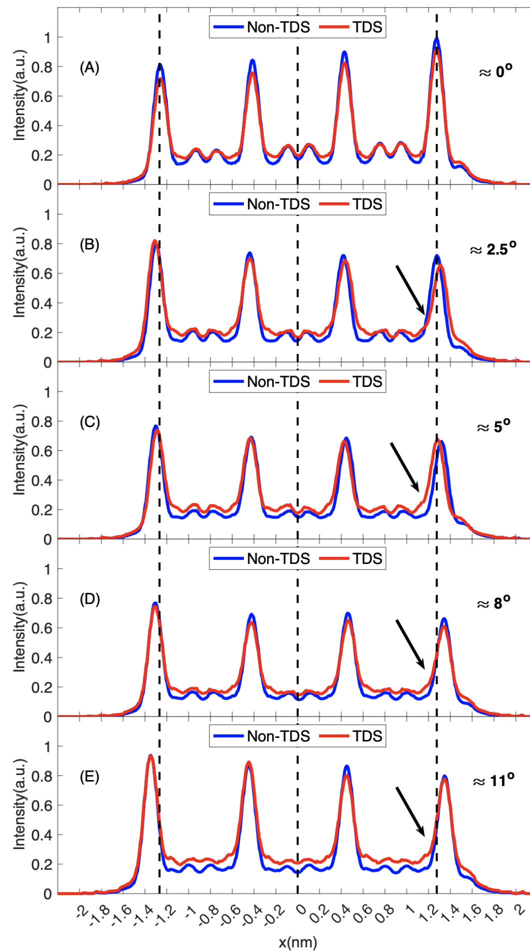

Fig. 5.6: Line profile taken in y-direction for Model II. (A) shows the result for the unstrained model, while B-E show the strained cases. The angle difference is stated in each plot as $\beta = -\theta$. Black arrows indicate shoulders on the maxima. The dashed lines mark the centre and position of the peripheral peaks for the unstrained case.

The x-axis line profiles in Fig. 5.7 reveals a curvature of lattice planes Model II, similar to Model I, however it is less pronounced due to the larger extension of the central region in Model II. Hence, the atomic displacements are in this case largely confined to the regions near the side facets. In agreement with the findings for Model I, Fig. 5.7 shows generally a decrease of all peak intensities and increase of background intensity when TDS is considered. Also, due to the lattice plane bending, the intensity peaks can be occasionally observed (e.g. in Fig. 5.7C) [34, 37]. An increased attenuation of intensity in the peripheral peaks can be observed with increased truncation angle values.

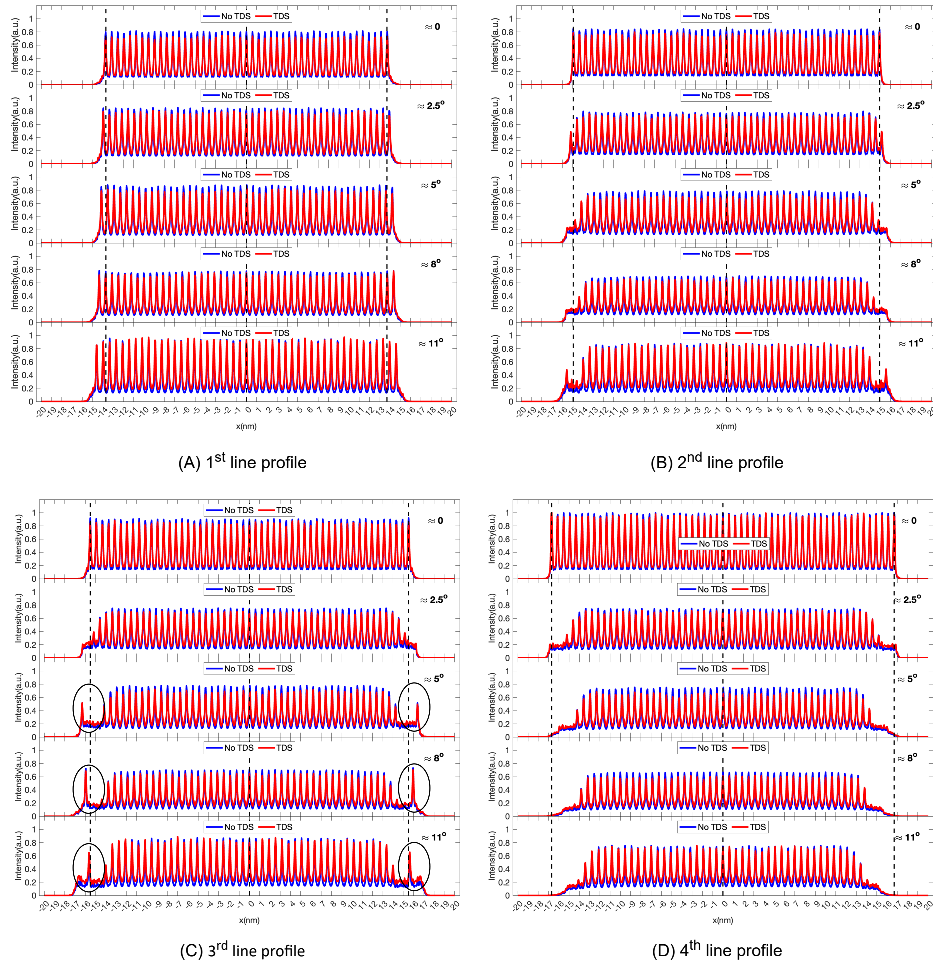

(A) 1st line profile

(B) 2nd line profile

(C) 3rd line profile

(D) 4th line profile

Fig. 5.7: Intensity profiles in x-direction, as indicated in Fig. 5.5. The dashed lines mark the centre and position of the peripheral peaks for the unstrained case. The zero angle is the non-displaced column. The angles difference are stated in each image in terms of $\beta = -\theta$.

In comparison, the impact of the applied external stress on the side facets of the truncated pyramid domain is more pronounced in the central part of the domain for the smaller domain (Model I) indicating that the atomic displacements are more significant here in comparison to the larger (Model II for 34 nm), which could be related to a greater significance of this local strain for lattice diffusion while for the larger domains the atomic displacement is more confined to the boundaries.

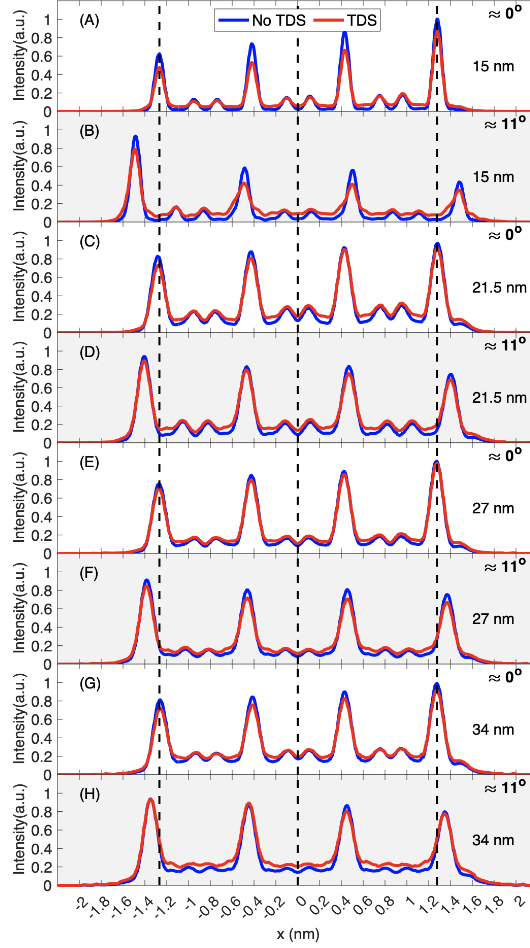

Fig. 5.8: Comparison of line profiles in y-direction for Model I, Model II, Model III and Model IV for the unstrained and maximum strained cases. (A, B) unstrained and strained case for Model I. (C, D, E and F) unstrained and strained case for Model III and Model IV, respectively (Since the centre of the model shows only three maxima in intensity (as in Figs. H.2 and H.5), this line profile is 1 nm off-center because of the model's cutting angle). (G, H) unstrained and strained case for Model II. The results show a "reversal" of peak intensity distribution in both cases but more pronounced for the smaller domain (Model I).

Finally, a direct comparison of the profiles in y-direction for Model I (15 nm), Model II (34 nm) Model III and Model IV (21.5 nm and 27 nm, respectively, see Appendix H.2 and H.5) reveals that the observed "reversal" of maxima intensity increases from bottom to top in the presence of strain can be observed for the small and large models with the difference that this effect is significantly more pronounced for Model I. This shows that the impact of external stress on the strain distribution within the oxide domain is mostly relevant for NPs with long edged length values $<$34 nm and, as can be seen in the examples shown in Appendix H.2, this is also true for values $<$21 nm. Hence, only small oxide domain sizes show an impact of the external stress on the lattice strain in the centre of the domain.

5.3 Comparing simulated and experimental Z-contrast images

After studying the results of Z-contrast image simulations of unstrained and strained iron oxide domains with and without TDS a comparison with experimentally obtained Z-contrast images was performed. The objective is to examine possible similarities or dissimilarities between the experimental image and the expected image contrast as observed for the simulated image by analysing the intensity line profiles as discussed in the previous section. This section will examine two experimental images, one with a side length of 15 nm and the other with a side length of 21.5 nm. The inclusion of both images is justified by their good quality, which facilitates the procedure of quantification.

Firstly, the smallest NP analysed by STEM of a cubic iron/iron oxide NP with a 15 nm side length and a 3 nm oxide shell as depicted in Fig. 5.9 was scrutinised. For this purpose, selected atomic columns at the periphery and at the core-shell interface were analysed. It was found that the column intensities near the core-shell interface are higher than those at the periphery (in this case, twice as high), in agreement with the results of the strained Model I findings.

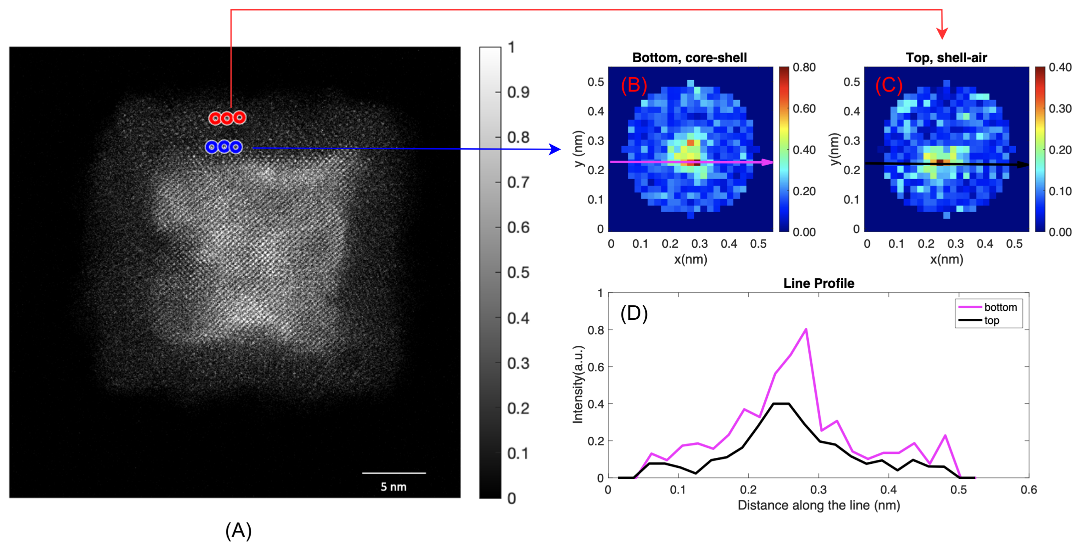

Fig. 5.9: (A) Normalised Cs-corrected HAADF image of a 15 nm cubic core/shell Fe/Fe oxide nanoparticle exhibiting a 3 nm-thick oxide shell. Blue circles represent columns near the core-shell boundary, while the red circles represent columns close to the surface of the oxide shell. (B,C) The images show the average of three columns, as indicated by the blue, red arrows close to the core shell and top oxide shell, respectively. (D)The line profiles of images of the average of three columns (B,C) in black and magenta plots.

Another illustration is given in Fig. 5.10. In this instance, the experimental image is of a cubic NP with a side length of 21.5 nm and an oxide shell of 3 nm. The results also reveal an intensity gradient in the image that corresponds to the trend of the displaced simulated image. The column intensities near the core shell are doubled than those at periphery in agreement with the results of the strained Model III findings (See Fig. 5.8 C,D).

Secondly, two different line profiles were produced on the x-axis (red arrow) and the y-axis (blue arrow), respectively. As depicted in the image on Fig. 5.11, the orientation of the arrows corresponds to the direction of the line profile. For this case a line profile was analysed for 21.5 nm side length. The region of interest is located in an area of the image where there is less noise and where the columns are easy to evaluate.

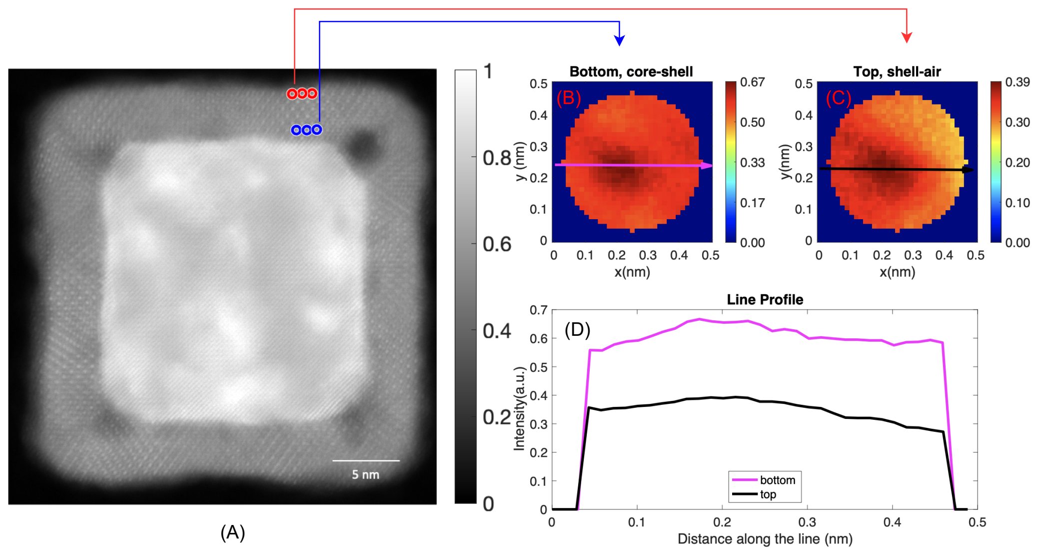

Fig. 5.10: (A) Cs-corrected HAADF images of a 21.5-nm-cubic core/shell Fe/Fe oxide nanoparticle exhibiting a 3 nm-thick oxide shell. The blue circles represent single columns that were determined to be closest to the core shell, while the red circles represent other columns close to the oxide shell. (B,C) The images show the average of three columns, as indicated by the blue and red arrows close to the core shell and top oxide shell, respectively. (D)The line profiles of images of the average of three columns (B,C) in black and magenta plots.

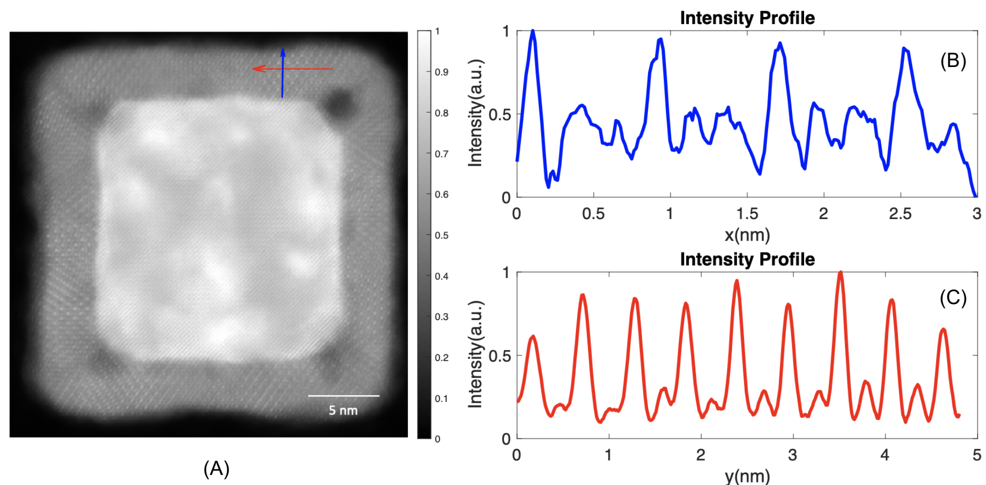

Fig. 5.11: HAADF image of a 21.5 nm core/shell iron oxide nanoparticle exhibiting a 3 nm-thick oxide shell(A). The y-direction is indicated by the blue plot (B), and the x-direction by the red plot (C). The arrows in the HAADF image indicate the positions and directions of the line profile.

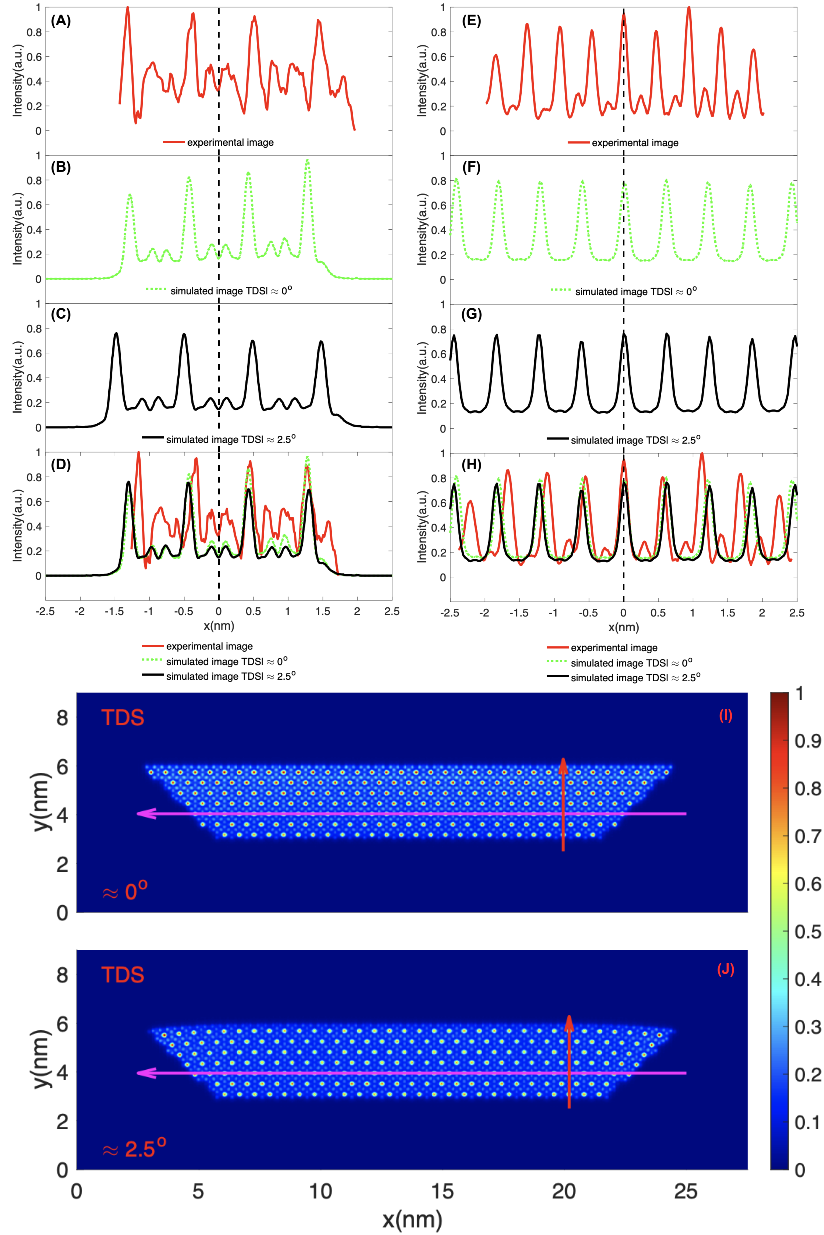

Fig. 5.12: Comparison of the simulated and experimental image line profiles. (I, J) simulated images of (model 21.5 nm). I is the non-displaced model and J is the displaced model with edge displacement of 0.5 nm. (A, B, C, D) line profile in the x-direction for experimental image (as in blue plot in Fig. 5.11.) and simulated image (as in red arrows in I,J). (E,F,G,H) line profile in y-axis for experimental image (as in red plot in Fig. 5.11.) and simulated image (as in magenta arrows in I,J).

In terms of the intensity gradient in the y- direction, the experimental image largely follows the trend of the simulated image. For example, the experimental

image line profile along the y-axis exhibits the intensity gradient shown in Fig. 5.11B, which is comparable to the behaviour of a displaced simulated model shown in Fig. 5.12C. The result also revealed that the spacing between the maximal peaks in the experimental image is compressed compared to the simulated images, an observation which is further supported by the FFT images acquired from the same portion of the line profile as that in Fig. 5.13. The FFT analysis reveals that the FFT image within the green square in the HAADF image exhibits a greater degree of elongation in its vertical orientation peaks, as compared to the FFT image within the red square in the HAADF image. This discrepancy may suggest the presence of compression within the oxide shell [108, 109].

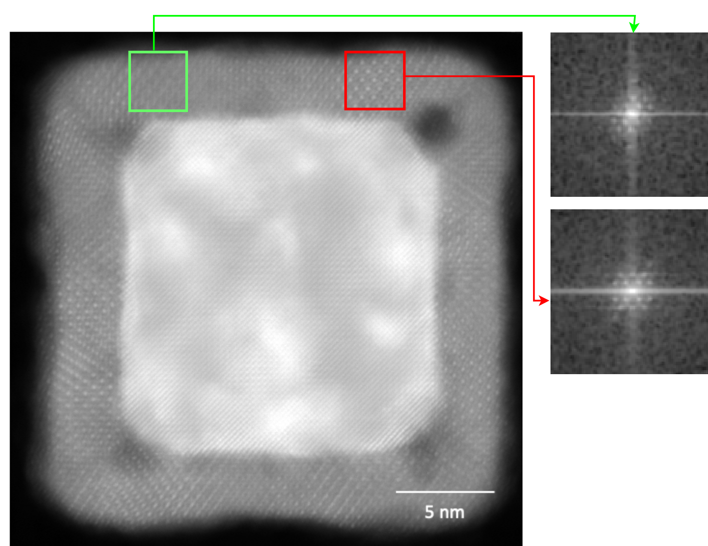

Fig. 5.13: HAADF image of a cubic 21.5 nm core/shell Fe/Fe oxide nanoparticle with a 3 nm oxide shell. Two FFT images were selected, as represented by the green and red squares in the HADF image. The FFT images were filtered out to reduce the image noise by using the imfilter function native to MATLAB. The FFT image in the green square in HAADF image shows elongation vertical orientation peaks compared to the red square in HAADF image which could indicate present of the compression in the oxide shell.

The line profile of the experimental image along the x-axis is displayed in Fig. 5.11C as the red plot and compared with the simulated images in Fig. 5.12 E, F, G, and H. This finding suggests that there is a degree of compression present in the

area selected in the experimental image which is further supported by FFT images in Fig. 5.13. The plot demonstrates that there is a smaller distance between each peak in the images obtained through experimentation as opposed to the distance present in the images obtained through simulation.

The line profile of the experimental images has limitations that make comparison of the experimental image to a simulated image challenging. For instance, the experimental image has more background noise than the simulated. The increase in background noise is a side effect of the experimental image, which makes it difficult to analyse the line profile. In addition to this, the image of the experiment was not taken at the perfected zone axis, which makes it difficult to acquire the line profile down the column. As a direct consequence, a single column is utilised in order to make the comparison between the simulated and the experimental images.

As a result, the experimental image data support the results of the simulation image in relation to the intensity being affected by the displacement field. When comparing the results of experimental and simulated images, using single columns provided the most accurate analysis of atomic column intensities.

5.4 Displacement fields for Model I and II

Within the context of the simulation image, the displacement field was calculated in order to investigate the influence of the displacement field on the model geometry. Instead of basing the calculations of the local displacement field on the whole Fe oxide atoms (Fe^{2+} and Fe^{3+}), it was the Fe^{2+} atoms in the model that were used for the calculation.

This strategy is being pursued because it is simple to analyse, as demonstrated in ref. [30], and because the experimental image reveals that Fe^{2+} has higher intensities than Fe^{3+} hence easy to identify. The distance between the base lattice vector and the reference point in the model was used to calculate the displacement field mapping. Therefore, displacement can be determined by calculating the distance between these points as follows

$$D_{R1} = \frac{\sqrt{XY^2 + X_0^2}}{\sqrt{R_{1i}^{\,2} + R_{1f}^{\,2}}} \tag{5.1}$$

$$D_{R2} = \frac{\sqrt{XY^2 + Y_0^2}}{\sqrt{R_{2i}^{\,2} + R_{2f}^{\,2}}} \tag{5.2}$$

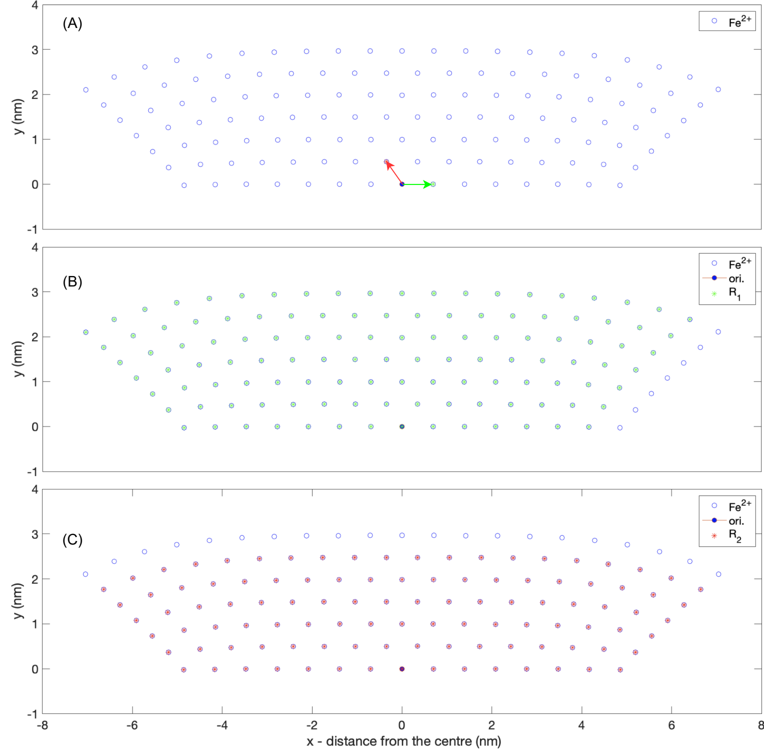

Fig. 5.14: Atomic distribution of Fe^{2+} atom positions for Model I. (A) 2D plot of Fe^{2+} atom positions (blue open circle), a reference point (the original point, filled blue circle), a base lattice vector in the R_1 (x)-direction (green arrow), and a base lattice vector in the R_2 (y)-direction (red arrow). (B, C) identify the neighbouring Fe^{2+} atom positions close to the reference point. (B) Fe^{2+} ions positions along the R_1 (x)-direction. (C) Fe^{2+} atom positions along the R_2 (y- direction). Some atoms near the right boundary, as in (B), and near the top boundary, as in (C), were not picked up because there are no neighbouring atoms along these boundaries.

where XY is the atom position and X_0 is the nearest atom position in the R_1 (x)-direction, and Y_0 is the nearest atom position in the R_2 (y)-direction. The base vector fields in the d_1 and d_2 directions are $R_1 = (R_{1i}, R_{1f})$ and $R_2 = (R_{2i}, R_{2f})$, respectively. Figure 5.14 shows the selected points (base lattice vector and the

reference point) in the model. The reference was chosen from the model lower strain area. This is the interface between the core and shell of the Fe@FeOx NP. The two vectors represent the positions of the atoms nearest to the reference point.

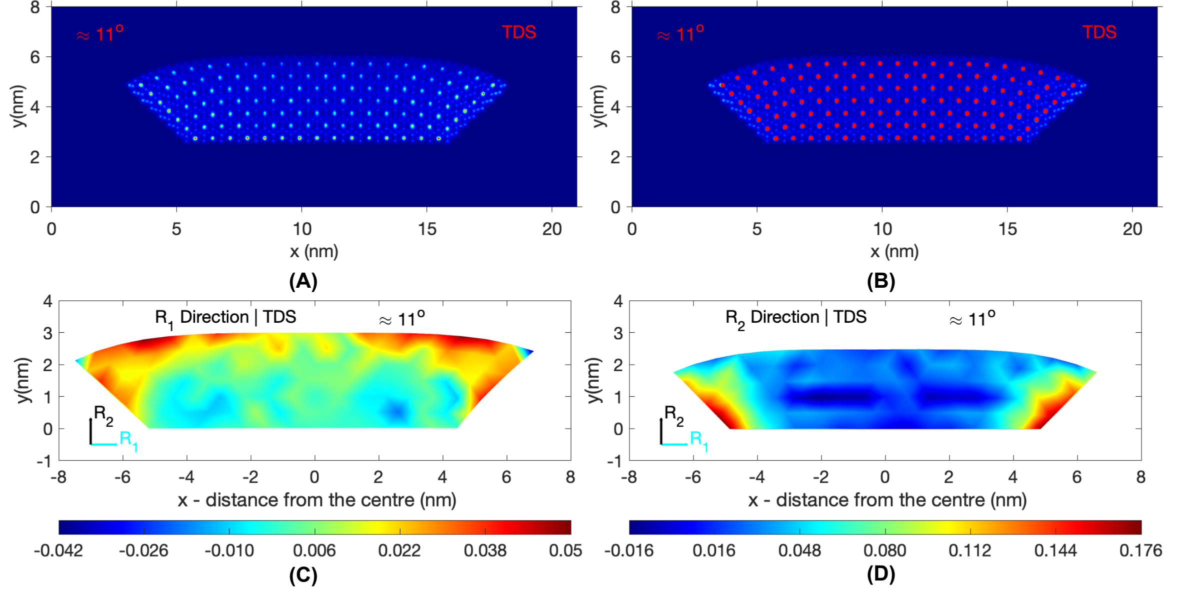

Fig. 5.15: Multislice simulated Z-contrast image for colour mapping image (A) of Model I. The Fe^{2+} columns correlate to high-intensity maxima, while the Fe^{3+} columns correspond to low-intensity maxima. (B) The Fe^{2+} atom positions (red dots) overlap the simulated image to identify the Fe^{2+} in the image. (C, D) displacement field mapping along the R_1 (along the x-axis) and R_2 direction (along the y-axis) based on the Fe^{2+} atom positions displayed in Fig. 5.14(B, C).

Figure 5.15 presents the mapping of the displacement field for Model I. Fig. 5.15B provides a visual representation of the identification of the Fe^{2+} atoms. The displacement field was calculated by applying Eqs. 5.1 and 5.1 after taking into account the atom distribution. Fig. 5.15C and D show the displacement fields in the R_1 direction (along the x-axis) and in the R_2 direction (along the y-axis), respectively. As can be seen in Fig. 5.15C, the majority of the displacement happens to be found around the upper boundary, at roughly 5.5% which is reveals a local increase of the spacing of atomic columns. However, there are small compressions at the bottom edges. In addition, some other regions of the model exhibit compression strain. This is as a result of the fixed condition that is located at the base of the model. On the other hand, the displacement map in the R_2 direction (along the

y-axis) reveals that the largest displacements, of around 17%, can be found near the left and right boundaries which could indicate a large spacing between the atomic columns around these area. There is a compression strain present on the y-axis in this mode as well around 1.6%. The displacement field mapping of the model shows a bending in Model I which is related to gradient deformation in the metals, which is caused by the Gorski effect (see Section 2.2.2 in Chapter 2) [63, 64, 5]. It is evident that the distribution of the displacement field in the model, at least in the R_1 direction, is extremely widespread across the entirety of the model. Because this is where the core shell interface is located, it is quite likely that the displacement field will disperse the majority of the atoms along this direction. This will result in the formation of additional defects, which will then lead to an increase in the number of paths available for diffusion and oxidation (see Chapter2) [30].

Figure 5.16A shows the field profile for Model I. The strain field profile was obtained from two different places in the model displacement field mapping in the R_1 (x)-direction. The strain field was obtained from the centre of the model, as can be seen from the magenta plot and arrow in Fig. 5.16A. The results reveal that the strain profile shows no compression strain at the bottom and 1.5% strain tensile at the model centre top as in Fig. 5.16B.

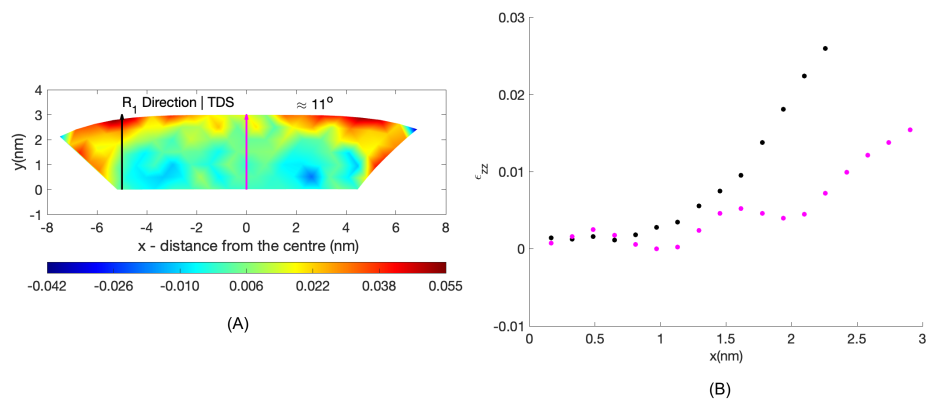

Fig. 5.16: (A) 2D displacement mapping of model 15 nm in the R_1 direction along the x-axis. (B) strain profile in R_1 direction. Data were obtained from two-line profiles, as indicated by the arrows in the 2D displacement mapping.

Another strain field profile was obtained, this time close to the edges of the boundary, as per the black plot and indicator arrow in Fig. 5.16A. There was around a 0.5% tensile strain area near the bottom edge of the model as in Fig. 5.16B. The

strain tensile strength was higher at the top surface, which was around 2.5% strain. The reason for the increased strain at the top in this location relative to the centre of the model is due to the grain boundary (GB) being subjected to high strain. The idea is that the GB will undergo internal strain caused by the triple junction (TJ) location where the anisotropic component meets when the model grows (crystal growth) [99].The behaviour of the strain profile along the R_1 direction is, for the most part, comparable to the experimental image that was published in ref. [30]. It can be seen that the strain profile has a gradient, which is in agreement with the findings of the experiment that were presented in ref. [30]. Despite the fact that it does not have the same value of strain, it follows the gradient of the strain profile. A further observation is that the strain is not mostly concentrated at the centre of the model; rather, it has moved towards the boundary, which is analogous to the experimental image result reported by Pratt et al [30].

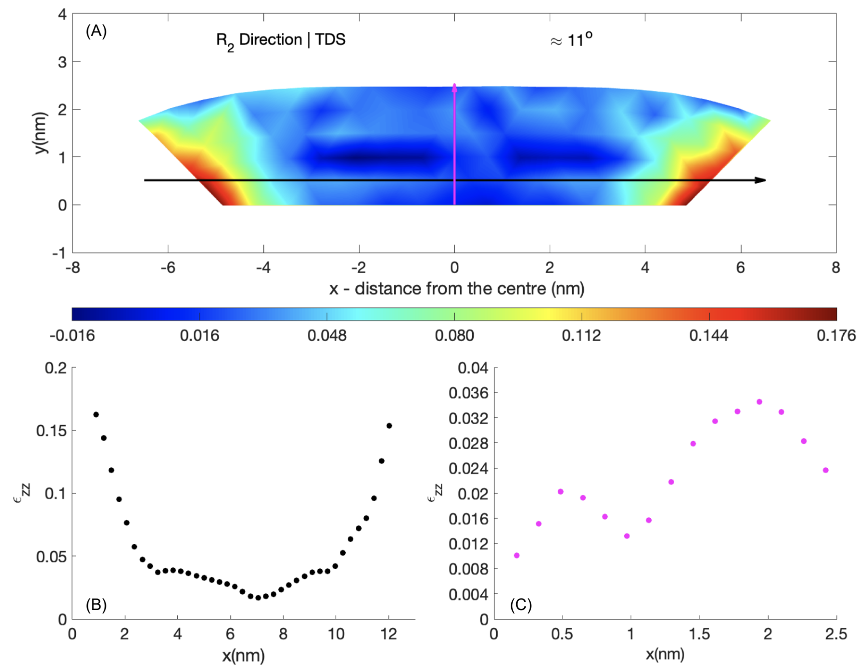

Fig. 5.17: (A) 2D displacement mapping of model 15 nm in the R_2 direction along the y-axis. (B) strain profile in R_2 direction as indicated by the black arrow in (A). (C) strain profile in R_2 direction as indicated by the magenta arrow in (A).

The strain profile was taken in the R_2 (y)-direction from two different places in the model displacement field mapping, as shown in Fig. 5.17. The first line profile was taken from the centre of the model, as indicated by the magenta arrow Fig.

5.17A. The strain at the bottom is around 0.08% and the top of the model is around 2.5% as shown in Fig. 5.17C. The black arrow denotes the taking of another strain line profile from left to right. The strain is around 16% around the model grain boundaries as shown in Fig. 5.17B.

Around the boundary edges, the majority of the strain can be found in the R_2 direction. The strain in this particular direction (R_2) is not truly calculable based on the experimental data that we compared to that reported in ref. [30]. Nevertheless, it could be an interesting subject of future work to investigate the characteristics of this finding and compare them to the results of experiments. It is also possible that it caused a void in the experimental images. This is supported by the fact that some experimental images display a number of voids around the borders of the grain boundary(one example of the voids is Fig. 5.13), which may be connected to the phenomenon in some way. Fig. 5.18 displays the strain profiles that result from the various displacement fields applied to Model I. Table5.1 provides a listing of the values of the displacement field that were applied to the model.

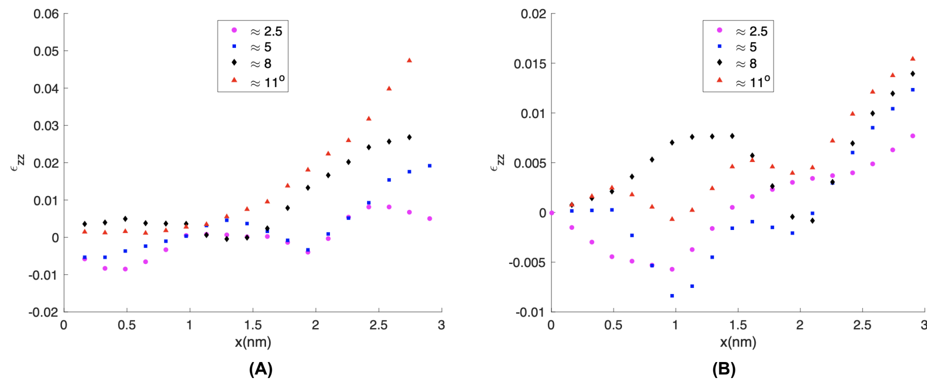

Fig. 5.18: Line profile plot of model 15 nm(Model I). Two line profiles were determined for different displacement fields applied to the model, as shown in Table5.1. The displacement field mappings of the model at 2.5^o, 5°, and 8° angles are shown Fig. I.1.The directional orientation of the strain line profiles is denoted by the arrows depicted in Fig. 5.16A. (A) Data is obtained from line profile close to the edge as indicted by the solid black arrow in Fig. 5.16A. (B) Data obtained from profile at the centre of the model as indicated by the magenta arrow in Fig. 5.16A.

Table 5.1: Displacement fields and parameters used for Model I.

Model	$\approx L_i$ nm	$\approx L_b$ nm	$\approx L_f$ nm	$\approx$ d nm	$\approx$ angle
2	14.5	9	15	0.5	2.5
3	14	9	15	1	5
4	13.5	9	15	1.5	8
5	13	9	15	2	11

L_i is the oxide segment top length model prior to application of the displacement field, L_b is the length of the bottom of the oxide segment where the core and shell meet, L_f is the length of the top of the oxide segment model after the displacement field is applied, d is the edge displacement, and the angle is the difference between the model without displacement and the model with.

The strain profile that was determined for the edges of the models is depicted as a solid black arrow in Fig. 5.16A, and which can be found in Fig. 5.18A. As indicated in Table5.1, the model with an angle of 11° shows the largest strain, and the displacement field there is around 2 nm edge displacement. Approximately 5% of the total is strain. The model with an angle of 2.5^o has a displacement field that is around 0.5 nm edge displacement, making it the model with the lowest strain, at around 0.6% tensile strain. On the other hand, as compared to the strain for the model for 11°, the strain at the model of 2.5^o does not indicate a significant amount of strain tensile gradient. This could not be connected to the fact that the 2.5^o angle has a large relaxation region and the majority of the atoms in this direction are not affected by the displacement field. On the other hand, Fig. 5.18B depicts the strain profile at the model centre, as indicated by the magenta arrow in Fig. 5.16A. This line extends from the bottom of the model to the top surface. There is less of a correlation between the displacement field and the other strain profiles (Fig. 5.18A), which suggests that the strain moves away from the centre [30]. As can be seen in the red plot in Fig. 5.18B, the model of an angle of 11° demonstrates that there is a gradient in the strain, which rises from the bottom to the top of the surface.

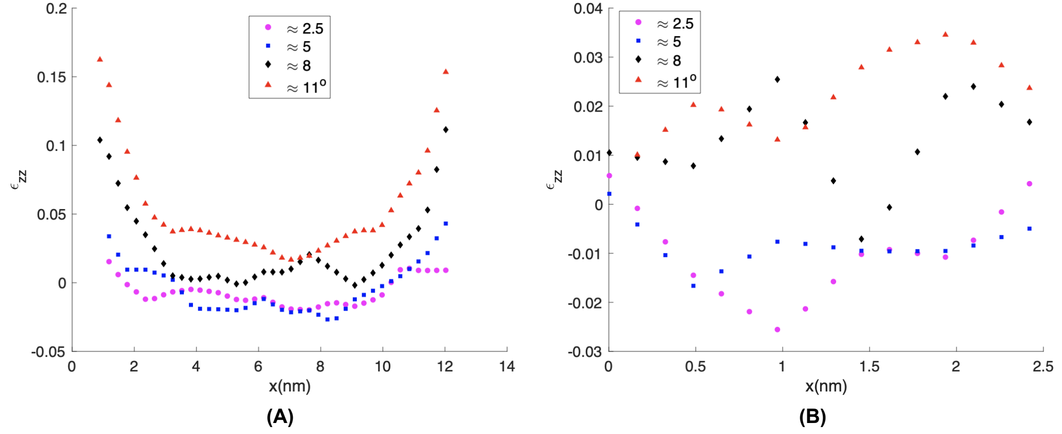

Fig. 5.19: Line profile plot for model 15 nm. Two line profiles were conducted for different displacement fields applied to the model, as shown in Table5.1. The displacement field mappings for the model at angles of 2.5^o, 5° and 8° are shown in Fig. I.1. The directional orientation of the strain line profiles is indicated by the arrows depicted in Fig. 5.17. (A) Data obtained from line profile close to the edge as indicted by the solid black arrows in Fig. 5.17. (B) Data obtained from profile at the centre of the model as indicated by the magenta arrow in Fig. 5.17.

In Fig. 5.19, a strain profile plot of several displacement fields that were applied to the model 15 nm(Model I) along the R_2 direction (along the y-axis) is presented. As indicated in Fig. 5.17A by the solid black arrow line and the magenta arrow, the strain profiles were obtained from the model in two separate places. The comparison reveals that the majority of the strain can be found in close proximity of the grain boundaries of the model along this specific direction. The strain represented by the model of the 11° (2 nm edge displacement) angle is approximately 16%, as shown by the red plot in Fig. 5.19A. Nevertheless, compression can be seen in the strain line profile of the models that have a lower displacement field. For instance, compression strain can be shown around the centre in the models with a 2.5^o and 5° angle, as depicted in Fig. 5.19A by the magenta and blue plots, respectively. This may have something to do with the fact that these models have a relaxation area. This is because the presence of a larger displacement field in the model results in a reduced amount of compression along, in particular, the R_2 direction (along the y-axis).

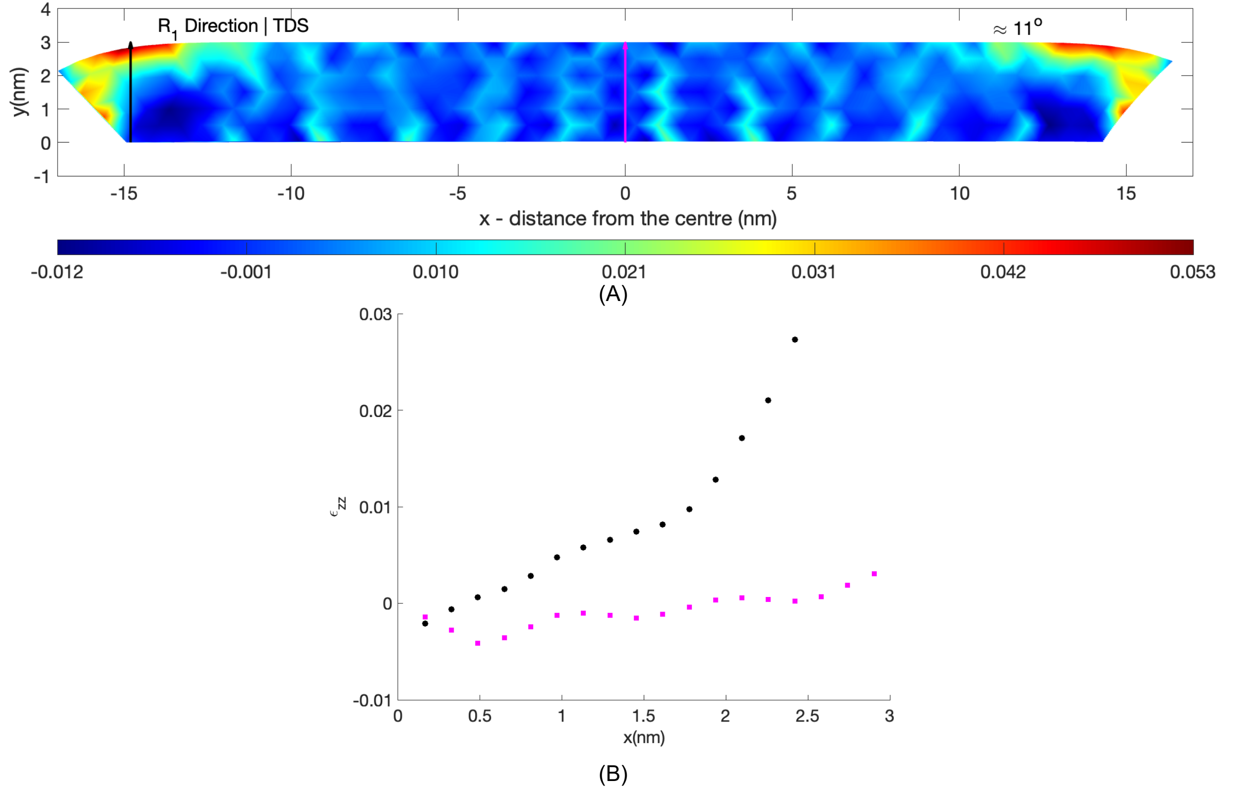

Fig. 5.20: 2D displacement mapping of model 34 nm in the R_1 direction along the x-axis. (B) strain profile in R_1 direction. Data were obtained from two-line profiles, as indicated by the arrows in the 2D displacement mapping.

This can be explained by the Poisson's ratio in the system, which explains the strain in one direction (tensile) and another (compression) [110]. Additionally, the system's geometry (truncated pyramid shape) is due to the external stress being applied to the side facets of the truncated pyramid domain, which are more pronounced than the centre. Fig. I.1(B, D, F, H) displays the lower displacement field among the models, with more compression values shown in the R_2 direction (along the y-axis).

Because one of the main objectives of this project is to provide a systematic study of the impact that the displacement field has on the image's intensity, the displacement field was not considered for model 15 nm (Model I) alone; Model II (34 nm), Model III (21.5 nm), and Model IV (27 nm) were also examined. Model II (34 nm) will be used in the following illustration; the other models can be found in Appendix I. The displacement fields were considered in the R_1 (the x-axis) and R_2 (the y-axis) directions, as shown in Fig. 5.20A and Fig. 5.21A, respectively, and the

values of the displacement fields were applied to the model based on the information reported in Table 5.2.

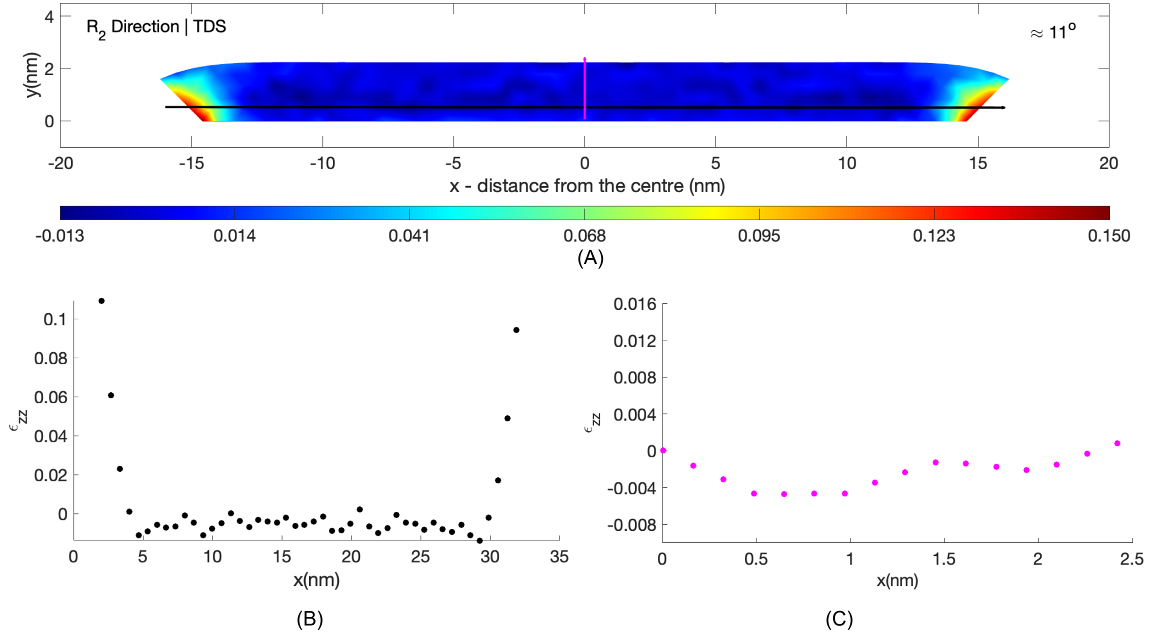

Fig. 5.21: (A)2D displacement mapping of model 34 nm in the R_2 direction along the y-axis. (B) strain profile in R_2 direction as indicated by the black arrow in (A). (C) strain profile in R_2 direction as indicated by the magenta arrow in (A).

Table 5.2: Displacement fields and parameters used for the 34 nm model.

Model	$\approx L_i$ nm	$\approx L_b$ nm	$\approx L_f$ nm	$\approx$ d nm	$\approx$ angle
2	33.5	28	34	0.5	2.5
3	33	28	34	1	5
4	32.5	28	34	1.5	8
5	32	28	34	2	11

The maximum tensile strain of 5% is observed in the displacement field in the R_1 direction for Model II at an angle of 11°, and a maximum compression strain of 1.2% is observed near the bottom near the grain boundary, as can be seen in Fig. 5.20A. For the same degree of displacement field, the models' overall tensile strains, at Model I and Model II, are not very different. The strain tensile in Model I at an 11° angle (about 2 nm edge displacement) is about 5.3%, while in the Model II is about 5%. However, Model II shows higher strain shifting along the model edge and

a larger area of relaxation in the centre compared to smaller models (e.g., Model I) in the R_1 direction displacement field; that is to say, the displacement field has not affected the vast majority of the atoms in the large model. One of the objectives of this effort is to determine how the atomic displacement field influences the oxidation mechanism's pathway. In this case, the large model (e.g., a Model II) exhibits a large relaxation area along the x-axis, mostly at the model centre, while most of the strain is shifted around the boundary of the model. As a result, the atoms near the model centre are less affected by the displacement field and might display fewer defects, while those near the boundaries display a higher degree of defect, vacancy, and oxidation.

As can be seen in Fig. 5.21A, Model II displacement field along R_2 exhibits characteristics analogous to those of Model I. The strain profile, for instance, is most pronounced around the model periphery. Strains of 15% in the tensile direction are present around the model periphery in the maximum displacement field mapping, while strains of 1.3% in the compression direction are seen in the same area. Figure 5.21C shows the strain profile conducted from the centre of the model. The result revels that less strain present in centre of the model compared to the periphery.

Several displacement fields applied to Model II along R_1 and R_2 are shown in Fig. 5.22. The results reveal an increase for the model of 11° in the R_1 direction, as can be seen in Fig. 5.22A, and which indeed are expected because of the high displacement field. Also, the majority of the strain is located close to the edges, as shown in Fig. 5.22A, while in the centre of the model, the strain profile is reduced compared to the edges, as shown in Fig. 5.22B.

A comparison of the strain profiles resulting from the use of the various size models, such as model 15 nm (Model I), Model II (34 nm), Model III (21.5 nm), and Model IV (27 nm), is given in Fig. 5.23. The strain profile was determined in two directions, R_1 as A, B in Fig. 5.23, and the data obtained from line profile close to the edge, which is shown by the solid black arrow and magenta arrow in Fig. 5.16A, 5.20A, I.3D and I.5D. The strain profile of R_2 as C, D Fig. 5.23 and its data obtained from line profiles from left and right as indicted by the solid black arrow and magenta arrow in Figs.5.17A,5.21A,I.3H and I.5H.

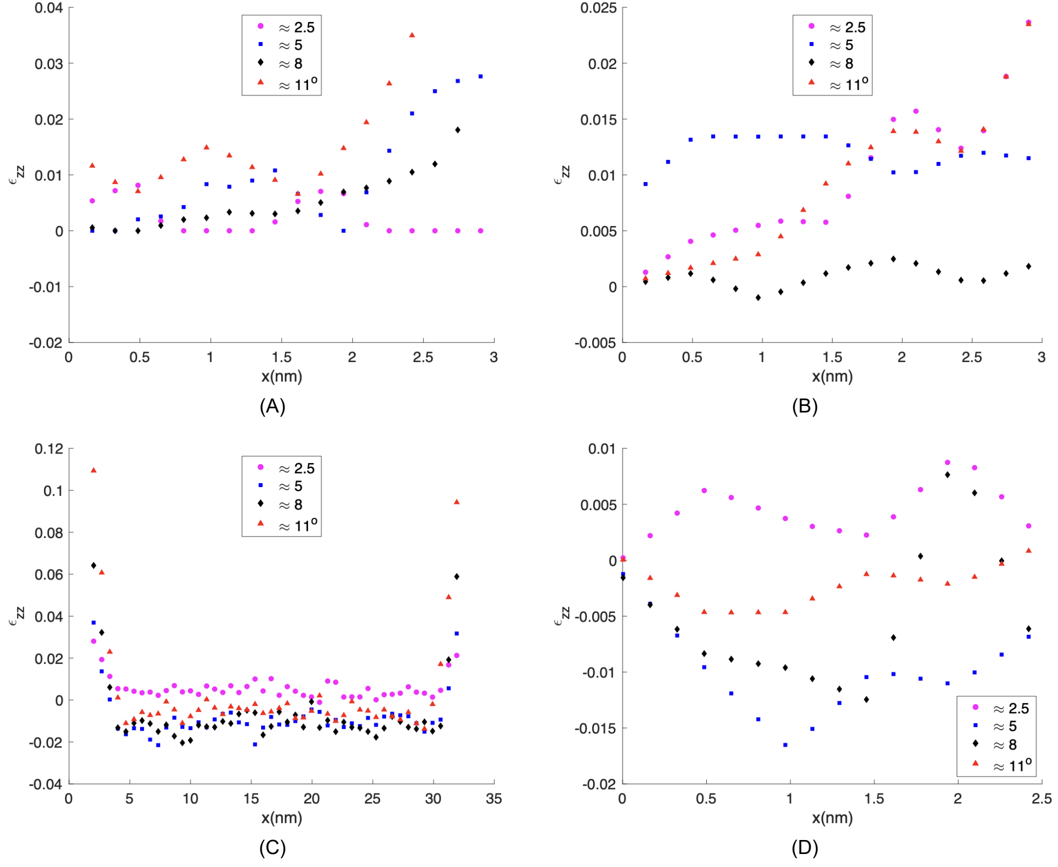

Fig. 5.22: Line profile plot of Model II. Two line profiles were determined for the different displacement fields applied to the model, as shown in Table5.2. (A) Data obtained from line profile close to the edge, as indicted by the solid black arrow in the displacement field mapping in R_1, as shown in Fig. 5.20A. (B) Data obtained from at the centre of the model, as indicated by the magenta arrow in the displacement field mapping in R_2, as seen in Fig. 5.21A. The directional orientation of the strain line profiles is indicated by the arrows. The displacement field mappings of the model at angles of 2.5^o, 5°, and 8° are shown in Fig. I.2.(Appendix I).

Comparison reveals that the large model has greater strain since strain is more pronounced at the edges. This is likewise the case in Model II where strain is relatively high compared to that of the other models. For comparison, the total strain in Model II is about 6%, while in Model I is about 5.5%. It should be noted that this merely shows the strain along the line and not the entire model. Therefore, one cannot reliably compare all models using the arrow-based line profile of the 2D displacement mapping; rather, it is far more appropriate to compare them based

on the entire distribution of the displacement field. While the tensile strain in the smaller Model I (15 nm) and Model III (21.5 nm) is 5.5% and 4.2%, respectively, it is higher in the larger Model IV (27) nm and Model II (34 nm) models at an 11° angle, at around 6%.

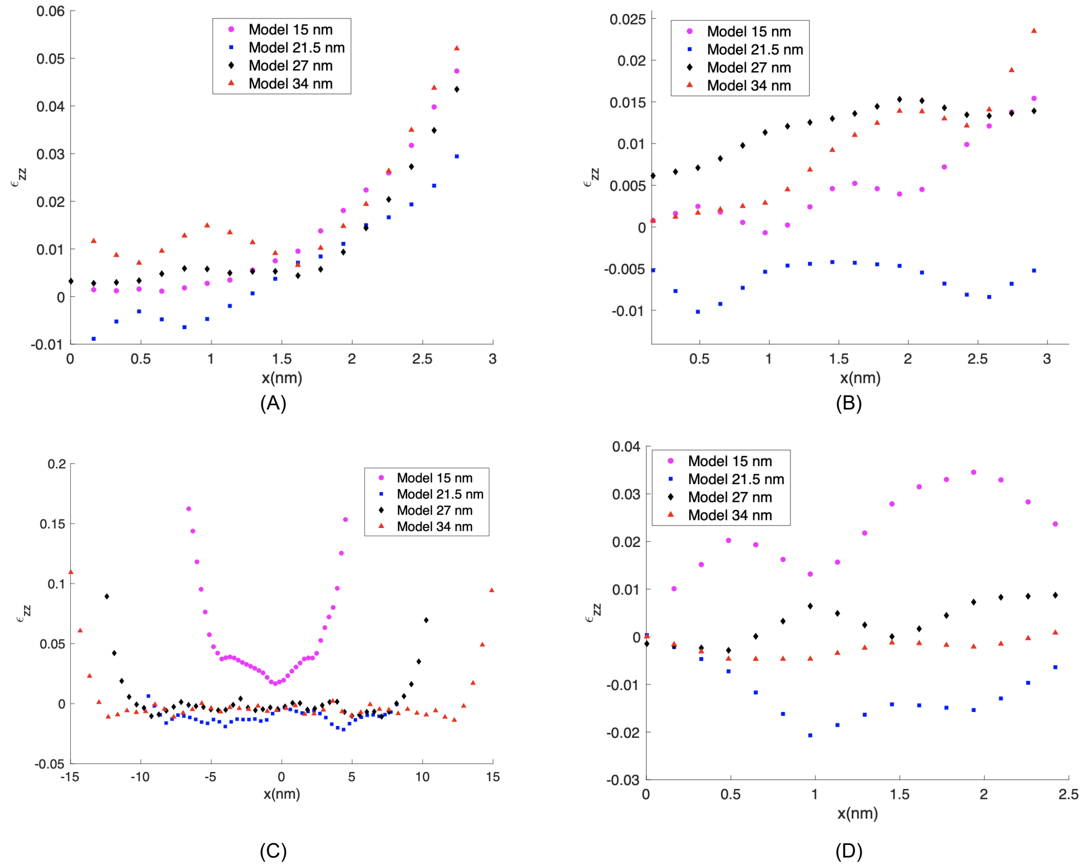

Fig. 5.23: Comparing the strain profile in the R_1 direction in (A) and (B), and the R_2 direction in (C) and (D) for different-sized models. The comparison is made between the different-sized models for the 11° angle. The data obtained from the line profile close to the edge is indicted by the solid black arrow and magenta arrow in Fig. 5.16, 5.20A, I.3D, and I.5D, and the data obtained from line profile from taken from the left and right is indicted by the solid black arrow and magenta arrow in Figs.5.17, 5.21A,I.3H, and I.5H.

Chapter 6

Conclusion and future work

6.1 Conclusion

This study reveals the important role of atomic displacements in core-shell nanoparticles of iron/iron oxide. In this work, one side facet of the 3D atomistic models of the oxide shell around an iron/iron oxide core NP are simulated using FEM to examine the effect of a 3D displacement field. After the 3D models were completed, simulations were run using the QSTEM simulation software. The effects of the 3D atomic displacement field have been studied using a range of sizes, such as 15 nm, 21.5 nm , 27 nm and 34 nm.

To summaries, the project's methodology is described in Chapter 4. First, the properties of the experimental image, such as the geometry, thickness, and length of the nanoparticles (NPs) that were employed in the FEM simulation to construct a three-dimensional atomic displacement field. Following this, the findings were implemented into the three-dimensional atomic structure of one side facet of Fe_3O_4 oxide shell. Each model was evaluated in a number of different 3D displacement fields, including those with edge displacements of 0.5 nm, 1 nm, 1.5 nm, and 2 nm.

The simulation results were shown in Chapter 5. Models intensity profiles and displacement field mappings were discussed. The results demonstrate the effect of the three-dimensional atomic displacement field on the three-dimensional models. As shown in Fig. 5.2, the image intensity of the 3D models reveals a gradient along the y-axis. This is because the atoms along the beam direction were displaced,

influencing the intensity of the image. Additionally, the x-axis intensity profile was investigated as in Fig. 5.3. The results demonstrate that the 3D atomic displacement field influences the number of atoms along the beam direction that contribute to image intensities. In Model I, as in the unstrained case, the number of Fe^{2+} atoms along the beam direction at the top is more than 10 atoms higher than that at the bottom,which is due to the 3D model geometry as a truncated pyramid structure; however, the strained model reveals that the number of Fe^{2+} atoms along the beam direction at the top is 4 atoms less than that at the bottom due to the displacement field. This is crucial for determining the number of atoms along the beam direction using the STEM image. This is important because both the internal strain field and the number of atoms along the beam direction influence the image intensity. Using the STEM image to determine the number of atoms is only possible if the image is made of strain-free materials. This result may help researchers who want to quantify the image contrast.

The findings of the displacement fields mapping in R_1 (as in $x-$axis) reveal that the distribution of the displacement field relies on the size of the model. For instance, the displacement field distribution of Model I is distributed all over the side facet of the model, but the displacement field mapping of Model II is likely to vary around the grain boundaries of the model. This suggests that the relaxation area for Model I is smaller in comparison to that of Model II. This finding also suggests that diffusion in small NPs, such as in Model I, occurs primarily as a result of the lattice strain, but in large NPs, such as in Model II, diffusion occurs primarily across the grain boundaries because the presence of the strain can enhance the oxidation and diffusion of the NPs [30]. As a direct consequence of this, the size of the NPs is a significant factor in the diffusion and oxidation behaviour of the NPs. This is could be related to the voiding that cause by out-diffusion iron from the core to the oxide shell [30] as seen in the experimental images in Figs. 4.3 and 4.4,4.5. For example, the large experimental images show a formation of such voids at the corners of these images which can be related to grain boundary diffusion while this is not true for small NPs as in Fig. 4.2, there is no void which is out diffusion through the lattice strain contributes to the whole structure. The displacement fields mapping in R_2 (as in the $y-$axis) reveals that the distribution of the displacement field varies around

the grain boundaries of the model regardless of whether the model is small or large.

6.2 Future work

Future work could make use of the approach developed in this thesis (combination of finite simulations and their application to nanostructures for image simulation) to evaluate the effect of strain fields in nanostructures with different geometries (e.g. spherically shaped particles). This approach would help to identify the potential contributions of lattice and grain boundary diffusion to the nanoparticle reactivity. Furthermore, the impact of size variations and core-shell structures on nanoparticle reactivity should be explored in this context.

Appendix A

Aberration-correction in STEM

The aberration that occurs in the STEM is due to the electromagnetic lenses that used in the STEM. Figure A.1 shows a schematic of electromagnetic lenses.

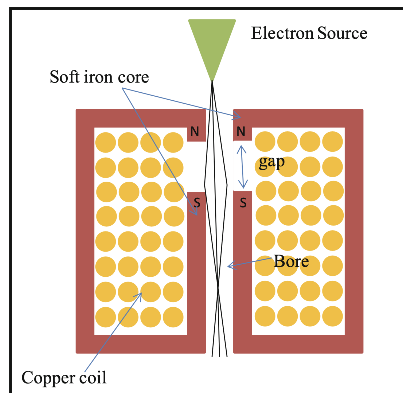

Fig. A.1: Schematic of electromagnetic lenses [16].

The lenses are composed of two distinct components. The first component consists of a cylindrical, symmetrical core composed of soft magnetic material. The polepiece, which is composed of soft iron, features a central aperture known as the bore. The polepiece has the potential to consist of two distinct components, namely an upper and a lower portion. The spatial separation between the two polepieces is commonly referred to as the gap. The ratio between the bore and gap of a lens is a significant property that influences the lens's ability to manage focus. The second component consists of a coil made of copper wire, which is positioned around the polepieces. By circumventing the prevailing notion of coiling, the act of passing through it will result in the generation of a magnetic field within the bore. The

field in this context exhibits heterogeneity. The presence of resistance in the coiling process leads to the heating of the coil, necessitating the inclusion of a cooling mechanism within the lenses to regulate their temperature[16].

One of the examples of the aberration- correction is spherical aberration (C_s). Spherical aberration is measured by its coefficient, C_s:

$$d_{C_s} = C_s \alpha^3 \quad \text{(eq. A.1)}$$

where is α is convergent semiangle.

The C_s-correction in STEM is a probe correction which means that the beams pass through the OLs is corrected by adding the aberration corrector before the OLs as shown in Fig. A.2.

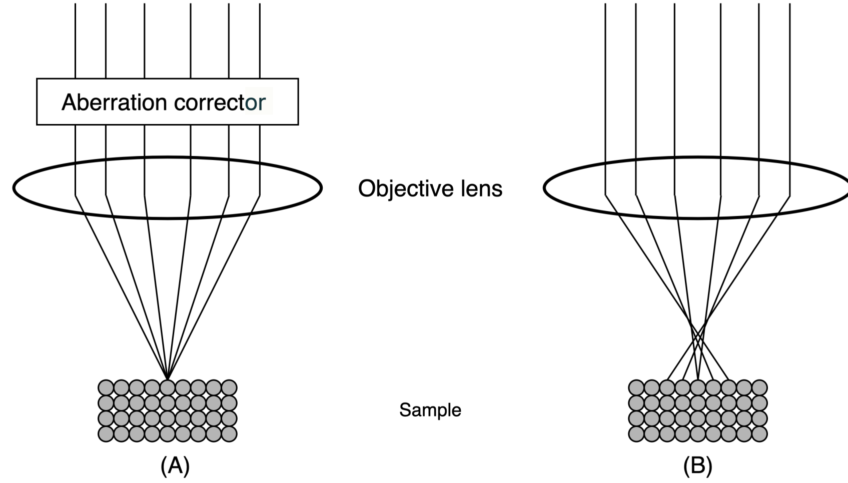

Fig. A.2: Electron trajectory in an electromagnetic lens and a perfect lens. (A) Schematic of the corrected probe after adding an aberration corrector. (B) schematic of uncorrected probe[17, 18].

The C_s correction STEM provides higher image resolution. This is because the image resolution δ in STEM depends on the wavelength λ and coefficient, C_s, as fallows.

$$\delta_{STEM} = 0.43(C_s \lambda)^{\frac{1}{4}} \quad \text{(eq. A.2)}$$

To improved the image resolution, the δ should be a small, which can be done either λ or C_s decreasing. However, decreasing λ has limitation because lower λ

value increase the electron voltage energy, as in Eq. 3.2, of the beam which could damage the sample(around 300 kV but depends on the sample itself). In the other hand, the C_s can be improved by adding an aberration corrector to reduce the C_s value close to zero.[17, 18].

There are two further types of aberration corrections, namely astigmatism aberration and chromatic aberration. In essence, astigmatism arises from the electron's interaction to an asymmetrical magnetic field in around of the optical axis. The presence of a magnetic field can occur from several factors, including the introduction of an aperture that can disrupt the field surrounding the optical axis in the lens. Consequently, the focal length exhibits variation when considering the lens orientations that are perpendicular to one other. Astigmatism can be managed by the utilisation of astigmators, which are miniature octopoles employed to mitigate the field inhomogeneities induced by astigmatism. The equation that explains the balance expressed as follows

$$r_a = \alpha \Delta f \qquad \text{(eq. A.3)}$$

Where Δf is the maximum difference in focus influenced by astigmatism and β is the angle between the optical axis and diffracted beam. The balance between the Δf and β can be corrected by build in software in STEM[17, 18].

Chromatic aberration occurs when electrons with various energies travel through the objective lens, causing the electrons with lower energies to deflect (bend) substantially and create a disc at a different point along the optic axis.[17, 111]. The radius of this disc can be calculated using the following equation

$$r_{chr} = C_c \frac{\Delta E}{E_0} \alpha \qquad \text{(eq. A.4)}$$

Where C_c is the chromatic aberration coefficient of the lens, ΔE is the energy difference of the electron, E is the initial energy of the electron, and β is the angle between the optical axis and diffracted beam.

Appendix B

Elastic and inelastic electron scattering

The interaction between the electron beam and the specimen causes electron scattering. In the Electron Microscopy (EM), many signals of the electron will be produced after the interaction of the electron with the specimen as summarised in Fig. B.1.

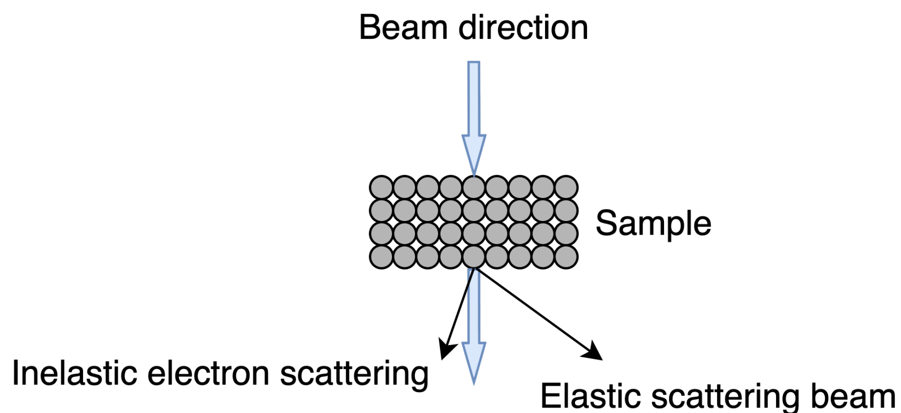

Fig. B.1: Summary of elastic and inelastic electron signals resulting from an electron's interaction with matter in TEM. The elastic scattered at higher angle and inelastic scattered close angle to optical axis.

The scattering of the electron within the sample results in a primary or secondary electron. A primary electron is one that transmits through the specimen, whereas a secondary electron generate inside the specimen and, in some cases, it does not leave the specimen[90]. As a result, there is elastic electron scattering and inelastic

electron scattering. Elastic electron scattering occurs at large angles which can be in the region of 0.01 - 0.1 radians, where none of its kinetic energy is lost. In comparison, inelastic scattering has a slight scattering angle in the region of 0.002 radians and is characterised by an electron energy loss. It is possible to determine the scattering angle θ using Bragg's law, as follows

$$\theta = \frac{\lambda}{2 \times d_{hkl}} \qquad \text{(eq. B.1)}$$

Where λ is the wavelength and d_{hkl} is the distance between the lattice plane. Electron scattering comes from either the interaction between the electron beam and the atomic nuclei or the electron cloud around the atomic nuclei [90]. As a result, the electron will experience Coulomb interaction. When the electron comes into the electron cloud, the electron beam will scatter at a high-angle, small-angle, or 180-degree angle, depending upon how strong the Coulomb interaction is [17], as shown in Fig. B.2.

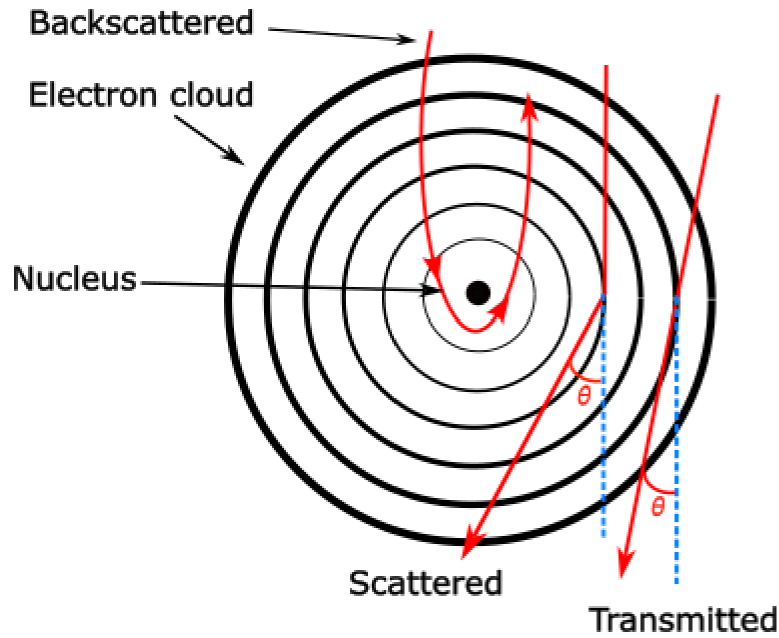

Fig. B.2: How the electron beam interacts with the nucleus in the electron cloud.

After Coulomb interaction has influenced the electron, the electron deflection will be proportional to the cross-section which is called the Rutherford differential cross-section [19].

$$\frac{d\sigma}{d\Omega} = \left(\frac{1}{4\pi \cdot \epsilon_0} \cdot \frac{Z \cdot e^2}{4 \cdot E_0} \right)^2 \cdot \frac{1}{\sin^4 \frac{\theta}{2}} \qquad \text{(eq. B.2)}$$

By integrating Eq eq. B.2,

$$\sigma\left(\alpha\right)=\left(\frac{Z\cdot e^{2}}{8\cdot\epsilon_{0}\cdot E_{0}}\right)\cdot\frac{1}{\pi\cdot\tan^{2}\frac{\alpha}{2}} \tag{eq. B.3}$$

The acceptance angle should be less than the total electron scattering angle (α). ε_0 is the permittivity of vacuum, Z is the atomic number, e is elementary electric charge and E_0 is the energy of the primary electrons. Another influence on electron scattering is the atomic density of the specimen. It is possible to indicate that the total electrons scattered by the atomic density of the specimen is expressed as follows

$$N=N_{A}\cdot\rho V \tag{eq. B.4}$$

The number of the scattered electrons (N) directly relates to the N_A Avogadro's constant, density ρ and volume V of the specimen.

Meanwhile, scattering electron magnitude depends upon the thickness of the specimen. The description of this is expressed as follows

$$N_{E}=N_{E,0}\cdot e^{-s/\Lambda_{el}} \tag{eq. B.5}$$

The equation describes the number of deflected electrons (N_E), while $N_{E,0}$ is the incident electron and the electron path is s. Λ_{el} is a free path of the elastic scattering known as follows

$$\Lambda_{el}=\left(\frac{8.\varepsilon_{0}.E_{0}}{Z.e^{2}}\right)^{2}.\frac{\pi.tan^{2}\frac{\alpha}{2}}{N_{A}\ .\ \rho} \tag{eq. B.6}$$

Figure B.3 shows the detector's angle that impacts the scattered electron that contribute to the image. The reason for this is θ dependents in Eq.(eq. B.2). The scattering angle becomes smaller for larger values of θ and becomes larger for smaller values of θ. The parameters used $e = 1.60219 \times 10^{-19}$ electron charge, C. $\epsilon_0 = 8.85418 \times 10^{-12}$ vacuum permittivity, $C^2/(N * m^2)$. Z ($Fe^{2+} = 26$, $Fe^{3+} = 26$, and $O = 8$), effective atomic number for Fe_3O_4. $E_0 = 200$ kV.

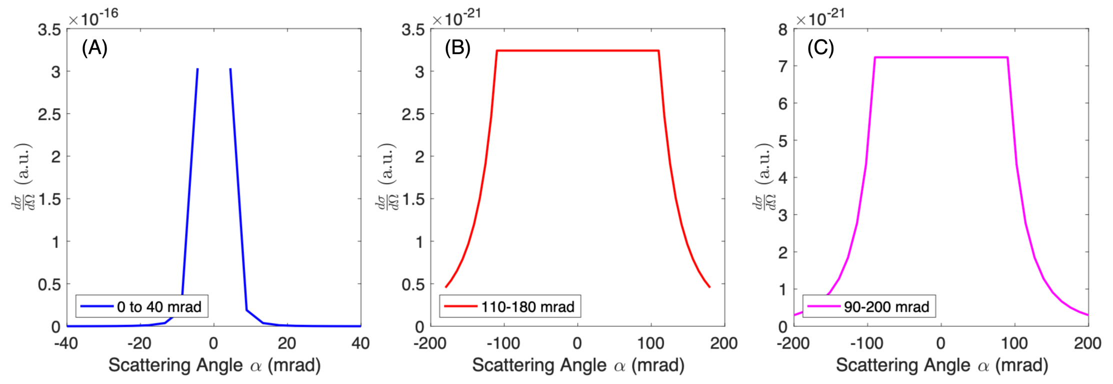

Fig. B.3: Electron scattered impacted by the the detector angle. (A) BF detector angle for 0-40 mard and (B) ADF angle detector for 110-180 mrad and (C) ADF detector for 90-200 mrad. These angels are based on the instrument that was used to take the STEM images. Using Eq.(eq. B.2) to calculate the scattered electron vs. the angles.

Appendix C

Contrast mechanisms

Contrast results from beam interaction with the specimen. It can be said that contrast is only related to elastic scattering in the specimen which can be spotted in the bright-field image. Contrast can be defined as the difference in illumination densities between two areas within the specimen and can be calculated using the following equation

$$C = \frac{(I_2 - I_1)}{I_1} = \frac{\Delta I}{I_1} \quad \text{(eq. C.1)}$$

Where I_2 and I_1 are intensities [17]. Figure C.1 illustrates the different intensities due to the thickness of the sample.

There are three mechanisms that affect contrast: mass thickness, diffraction contrast and phase contrast. Mass thickness contrast is seen in images due to differences in the atomic density of the specimen because the specimen's thickness influences the image's contrast. As a result, the bright-field image shows darker spots and fewer dark spots which indicates that the specimen has a greater density (darker spots) and lesser density (fewer dark spots), as shown in Fig. C.1. The rays when the electrons pass through different masses of the specimen are shown in Fig. C.1.

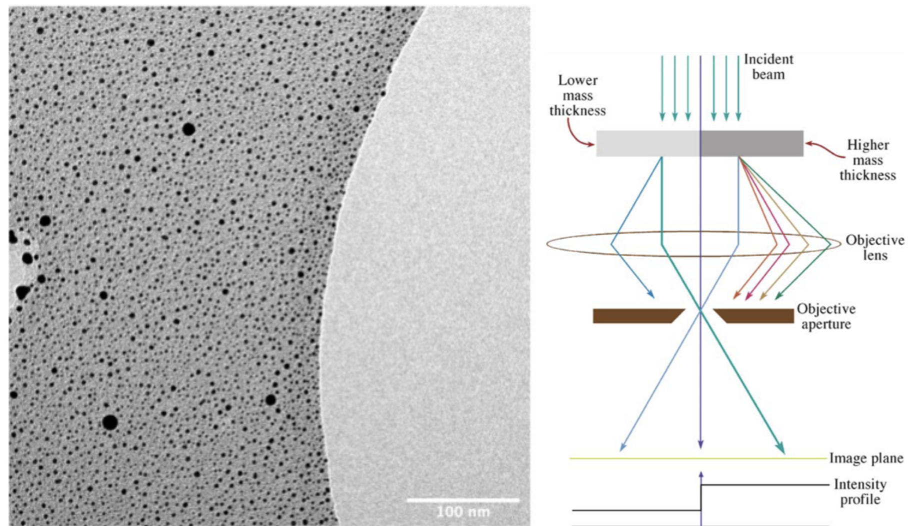

Fig. C.1: The effects of different mass thicknesses in the specimen. On the left is bright-field imaging of a test sample of Au NPs on C. On the right is a diagram showing the mechanism for how the beam interacts in different mass thicknesses in the specimen [17].

Diffraction contrast is a property of the electron wave when it passes through a crystalline sample. This property is due to the atomic arrangement in crystalline substances because when the electron wave passes through a crystal, it passes through slits between the atoms [16].It is worth noting that the TEM user should be able to distinguish between diffraction contrast and mass thickness contrast. To do so, the user should tilt the specimen; if the contrast changes, this indicates diffraction contrast but if it does not, this indicates mass contrast [19]. The final contrast is phase contrast which is essential for high-resolution imaging because this mechanism makes it possible to observe the atomic columns of the crystal. Phase contrast is the result of electrons with different phases interfering with each other as they pass through the objective lens. When the electron interacts with the atomic columns of the specimen, the wave plane which enters the specimen will not be the same as when it comes out of the specimen because the wave plane within the crystal will experience a phase shift [19].

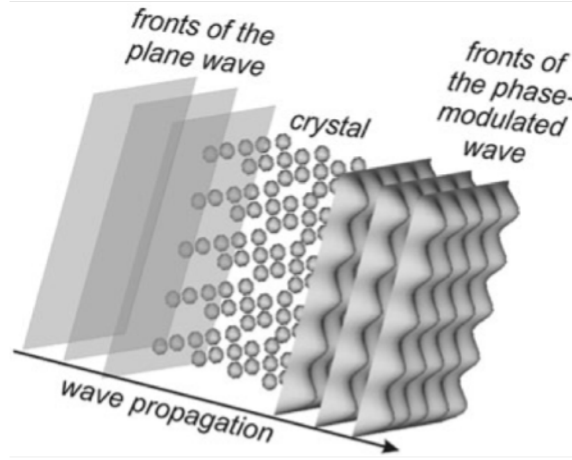

Fig. C.2: Plane waves which pass through the crystal will experience phase modulation[19].

To understand how the image contrast/phase contrast works, it is necessary to understand how the electron wave interacts with the sample. For instance, how the electron interacts with the specimen's crystal lattice or atomic structure along the column. The explanation of the electron movement within the sample can be characterised as a mechanical transverse wave which is not only the wave function motion inside and outside the crystal but also the wavelength behaviour inside and outside the crystal. Quantum mechanics can be used to explain the phase contrast using Schrödinger's equation which describes the electron wave inside the matter[19]. Schrödinger's equation will be used to establish the wavelength properties such as how fast it is and how it moves inside and outside the crystal. However, this could not be established without explaining the wave function in time and position dependence. Schrödinger's equation can be written as follows

$$i\hbar \cdot \frac{\partial \psi (x,t)}{\partial t} = \frac{-\hbar^2}{2 \cdot m} \cdot \frac{\partial^2 \psi (x,t)}{\partial x^2} - e \cdot \phi_0 \cdot \psi (x,t) \qquad \text{(eq. C.2)}$$

Where $\Psi(r,t)$ is the wave function, $\hbar = h/2\ \pi$, h is Planck's constant, $\Delta$is the Laplace operator, and $-e \cdot \phi_0$ is the equal potential energy V. It is good to start with the electron wave function which is dependent on the time (t) and position (r), which can be expressed as follows

$$\frac{d^2 \psi (t)}{dt^2} + \omega^2 \cdot \psi (t) = 0 \qquad \text{(eq. C.3)}$$

Equation (eq. C.3) is a harmonic oscillation for the electron which depends on time. Meanwhile, $\omega = \frac{2\pi}{T}$ where T is the oscillating time.

The solution to Eq. (eq. C.3) can be expressed as follows

$$\psi\left(t\right)=A\cos\left(\omega\cdot t+\phi\left(x\right)\right) \quad \text{(eq. C.4)}$$

Whereas A is constant amplitude and ϕ is a phase shift $=\pi/2$. Equation (eq. C.4) shows the wave movement as harmonic oscillation for $t=0$ and the position phase shift $=0$. However, the electron experiences a shift when passing through the sample due to the electron interacting with the sample. Harmonic oscillation will also shift and can be written as follows

$$\Psi\left(t\right)=A\cos\left(\omega\cdot t+\phi\left(x\right)+\phi_0\right) \quad \text{(eq. C.5)}$$

Where $\phi(x)$ is the phase shift that depends on the wave position and ϕ_0 is the phase shift at position = zero. Equation (eq. C.5) expresses the electron movement within the crystal but does not explain the wavelength's motion which depends on the phase velocity (c).

$$c=\frac{\lambda}{T}=\lambda\cdot v \quad \text{(eq. C.6)}$$

Where v is the oscillation frequency. Therefore, Eq. (eq. C.6) explains the wavelength velocity and Eq. (eq. C.5) shows the wave function behaviour within the crystal. However, Eq. (eq. C.5) requires further clarification and simplification. For example, the number of waves that pass through the sample depends on the time and position of these waves. The wave function is considered to be for the crest and, therefore, the wave function is expressed as follows

$$\Psi=\psi_0=A \quad \text{(eq. C.7)}$$

Hence,

$$\cos\left(\omega\cdot\ t+\phi\left(x\right)+\phi_0\right)=1 \quad \text{(eq. C.8)}$$

Therefore,

$$\left(\omega\cdot t+\phi\left(x\right)+\phi_0\right)=0 \quad \text{(eq. C.9)}$$

From Eq. (eq. C.9), it is possible to describe the wavelength's motion for the x-direction as follows

Because

$$x=c\cdot t\Rightarrow t=\frac{x}{c} \quad \text{(eq. C.10)}$$

and because

$$\omega = \frac{2\pi}{T} \qquad \text{(eq. C.11)}$$

by inserting Eq. (eq. C.10) and Eq. (eq. C.11) into Eq. (eq. C.9), the result is the following:

$$\Phi(x) = -\omega \cdot \frac{x}{c} - \phi_0 = -\frac{2\pi}{T} \cdot \frac{T}{\lambda} \cdot x - \phi_0 = -2\pi \cdot \frac{x}{\lambda} - \phi_0 \qquad \text{(eq. C.12)}$$

From Eq. (eq. C.12), the wave function is expressed as follows

$$\psi(x,t) = A \cdot \cos 2\pi (v \cdot t - k \cdot x) \qquad \text{(eq. C.13)}$$

Where $k = \frac{2\pi}{\lambda}$ which is the wave number, $v \cdot t$ is time dependence and $-k \cdot x$ is position dependence. Equation (eq. C.13) shows the wave function behaviour such as how many waves k pass through the sample and the phase shift velocity v.

Equation (eq. C.13) can be used to find the wave function in time and position dependence by taking the differential of Eq. (eq. C.13) for the oscillation frequency (v):

$$\frac{1}{v^2} \cdot \frac{\partial^2 \psi(x,t)}{\partial t^2} - \frac{1}{k^2} \cdot \frac{\partial^2 \psi(x,t)}{\partial x^2} = 0 \qquad \text{(eq. C.14)}$$

because

$$\frac{1}{v^2} \Rightarrow \frac{\lambda^2}{c^2} \qquad \text{(eq. C.15)}$$

$$\frac{1}{k^2} \Rightarrow \frac{\lambda^2}{4\pi} \qquad \text{(eq. C.16)}$$

From Eq. (eq. C.15) and (eq. C.16) being inserted into Eq. (eq. C.14), the result can be written as follows

$$\frac{1}{c^2} \cdot \frac{\partial^2 \psi(x,t)}{\partial t^2} - \frac{\partial^2 \psi(x,t)}{\partial x^2} = 0 \qquad \text{(eq. C.17)}$$

The solution to Eq. (eq. C.17), wave function, can be expressed as follows

$$\frac{\partial^2 \psi(x,t)}{\partial t^2} = -A \cdot (2\pi \cdot v)^2 \cdot \cos 2\pi (v \cdot t - k \cdot x) \qquad \text{(eq. C.18)}$$

$$\frac{\partial^2 \psi(x,t)}{\partial x^2} = -A \cdot (2\pi \cdot k)^2 \cdot \cos 2\pi (v \cdot t - k \cdot x) \qquad \text{(eq. C.19)}$$

Eq. (eq. C.13) can be written in general form as follows

$$\Psi(x,t) = A \cdot e^{-2\pi i (v \cdot t - k \cdot x)} \qquad \text{(eq. C.20)}$$

The solution can be as follows by taking the 1st differential equation and 2nd differential equation of Eq. (eq. C.20)

$$\frac{\partial \psi(x,t)}{\partial t} = -2\pi i \cdot v \cdot A \cdot e^{-2\pi i(v \cdot t - k \cdot x)} \tag{eq. C.21}$$

$$\frac{\partial^2 \psi(x,t)}{\partial x^2} = -(2\pi \cdot k)^2 \cdot A \cdot e^{-2\pi i(v \cdot t - k \cdot x)} \tag{eq. C.22}$$

The 1st equation, Eq. (eq. C.21), is time dependence and the 2nd equation, Eq. (eq. C.22), is position dependence. So far, the electron's wave function within the sample has been described. Now Eq. (eq. C.21) and Eq.(eq. C.22) are inset in Schrödinger's equation (eq. C.2) as follows

$$\hbar \cdot 2\pi \cdot v \cdot A \cdot e^{-2\pi i(v \cdot t - k \cdot x)} = \frac{-\hbar^2}{2 \cdot m} \cdot (2\pi \cdot k)^2 \cdot A \cdot e^{-2\pi i(v \cdot t - k \cdot x)} - e \cdot \phi_0 \cdot A \cdot e^{-2\pi i(v \cdot t - k \cdot x)} \tag{eq. C.23}$$

To simplify Eq. (eq. C.23), the following term is cancelled in Eq. (eq. C.23):

$$A \cdot e^{-2\pi i(v \cdot t - k \cdot x)}$$

Because $\hbar = \frac{h}{2\pi}$ and $hv = \frac{p^2}{2m}$ which is the energy-momentum, by inserting it into Eq. (eq. C.23), the solution is expressed as follows

$$p^2 = h^2 \cdot k^2 - 2 \cdot m \cdot e \cdot \phi_0 \tag{eq. C.24}$$

From the simply Eq. (eq. C.24), the wavelength of the electron within the specimen (potential Φ_0) is expressed as follows

$$\lambda = \frac{h}{\sqrt{p^2 + 2 \cdot m \cdot e \cdot \phi_0}} \tag{eq. C.25}$$

Where h is Planck's constant, p is electron momentum, and the electron mass is m. The electron charge is e. Finally, the potential is Φ_0.

If the wavelength is outside the crystal, the potential $\Phi_0 = 0$, and the wavelength can be rewritten as follows

$$\Lambda = \frac{h}{\sqrt{2 \cdot m \cdot e \cdot U_0}} \tag{eq. C.26}$$

Where U_0 is electron momentum p^2. It is important to note that the wavelength decreases when it goes inside the sample and this could influence the phase shift.

To describe this impact, the wavelength decreases when the thickness in dz (as z-direction) is increased. The following expression shows this relationship: the difference between the wavelength within the crystal and the wavelength outside the crystal:

$$d\phi = 2 \cdot \pi \cdot \left(\frac{dz}{\lambda_{Cr}} - \frac{dz}{\lambda} \right) = 2 \cdot \pi \cdot \frac{dz}{\lambda} \cdot \left(\frac{\lambda}{\lambda_{Cr}} - 1 \right) \qquad \text{(eq. C.27)}$$

Where λ_{Cr} is the wavelength within the crystal, as expressed in Eq. (eq. C.25), and λ is the wavelength outside the crystal, as shown in Eq. (eq. C.26). Using Eq. (eq. C.25) and Eq. (eq. C.26) in Eq. (eq. C.27):

$$d\phi = 2 \cdot \pi \cdot \frac{dz}{\lambda} \cdot \left(\sqrt{1 + \frac{\Phi\left(x, y, z\right)}{U_0}} - 1 \right) \qquad \text{(eq. C.28)}$$

Equation (eq. C.28) can be expanded using the Taylor serial. By taking only the second term of the Taylor serial, the solution is shown as follows

$$d\phi = 2 \cdot \pi \cdot \frac{dz}{\lambda} \cdot \left(1 + \frac{1}{2} \frac{\Phi\left(x, y, z\right)}{U_0} - 1 \right) = \frac{\pi}{\lambda \cdot U_0} \cdot \Phi\left(x, y, z\right) \cdot dz \qquad \text{(eq. C.29)}$$

The phase shift ϕ can be obtained by taking the integration Eq. (eq. C.28) for the thickness t, and the solution is expressed as follows

$$\phi = \frac{\pi}{\lambda \cdot U_0} \cdot \int_0^t \Phi\left(x, y, z\right) \cdot dz \qquad \text{(eq. C.30)}$$

Equation (eq. C.30) shows the phase shift of the wave function through the crystal. However, if it is assumed that the potential depends on the x- and y-direction and is constant in the z-direction, as in the image, Eq. (eq. C.30) can be rewritten as follows

$$\phi\left(x, y\right) = \frac{\pi \cdot t}{\lambda \cdot U_0} \cdot \Phi\left(x, y\right) \qquad \text{(eq. C.31)}$$

Equation (eq. C.31) is a solution to Eq. (eq. C.30) after taking the differentiation for the thickness t.

Equation (eq. C.31) explains that the incident electron wave depends on the specimen's thickness. In other words, the incident electron penetrates (t) in the z-direction within the crystal which means that the periodicity of the crystal lattice reflects the phase shift. The outcome wave shift from the crystal will project the crystal lattice (see Fig. C.2) [19].

Appendix D

Convolution of Functions $\otimes$

The definition of convolution is the multiplication and integration of two functions (f $\otimes$ g). The result describe one of the functions after it has been modified and shifted. These two functions in image processing could be real space function and FT function [90].

$$f \otimes g = \int_{-\infty}^{\infty} \mathrm{f}(y)\mathrm{g}(x-y)dy = \int_{-\infty}^{\infty} \mathrm{f}(x-y)\mathrm{g}(y)dy \qquad \text{(eq. D.1)}$$

Appendix E

Methodology appendix

E.1 Characteristics of the experimental STEM images

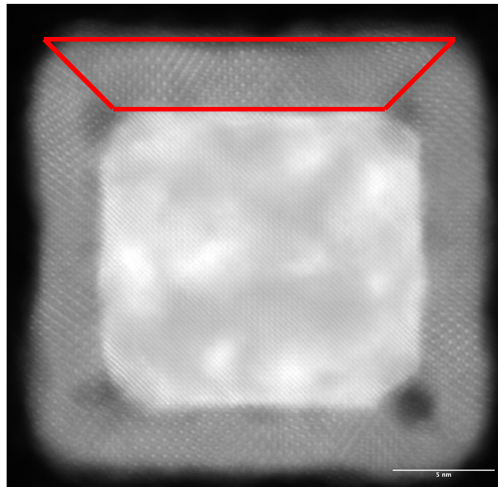

Fig. E.1: HAADF image of a core/shell Fe/Fe oxide nanoparticle. The top facet of the oxide shell is 21.5nm. The thickness of the oxide shell is 3 nm.

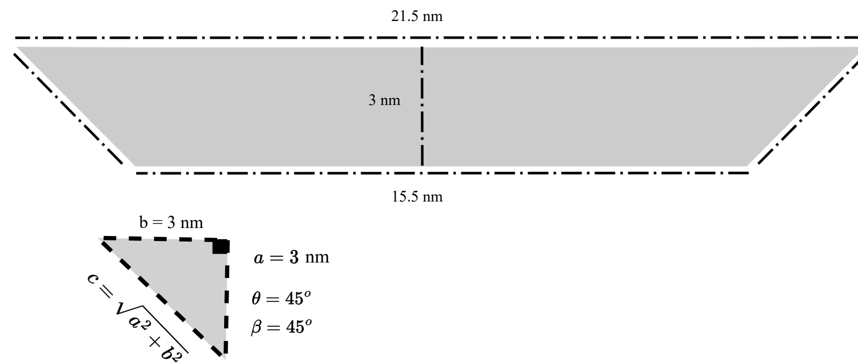

Fig. E.2: The oxide shell chosen from the STEM image, as indicated in the red line in the STEM image.

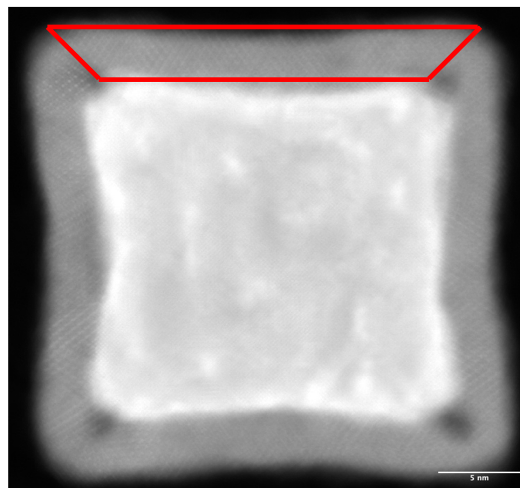

Fig. E.3: HAADF image of a core/shell Fe/Fe oxide nanoparticle. The top facet of the oxide shell is 27 nm. The thickness of the oxide shell is 3nm.

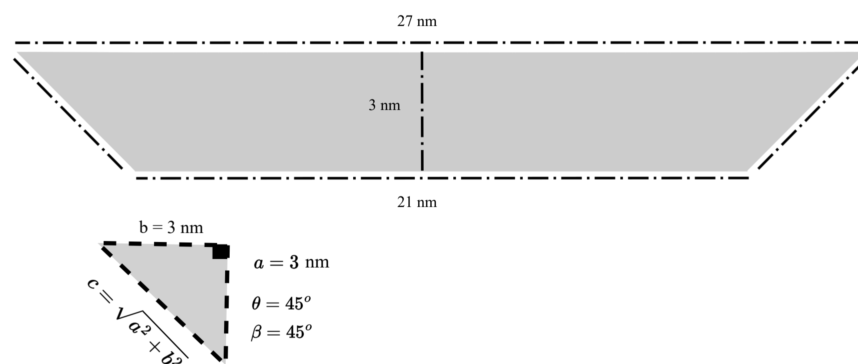

Fig. E.4: The oxide shell chosen from the STEM image, as indicated in the red line in the STEM image.

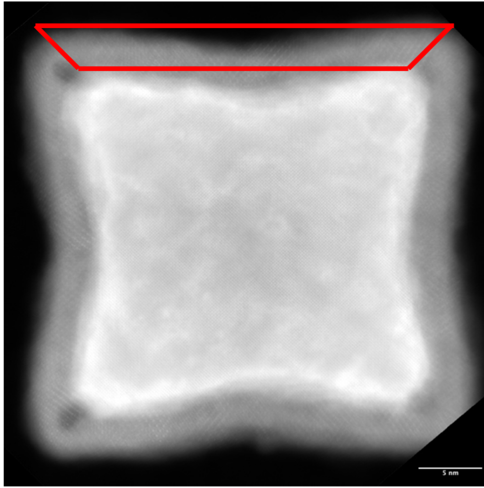

Fig. E.5: HAADF image of a core/shell Fe/Fe oxide nanoparticle. The top facet of the oxide shell is 34 nm. The thickness of the oxide shell is 3nm.

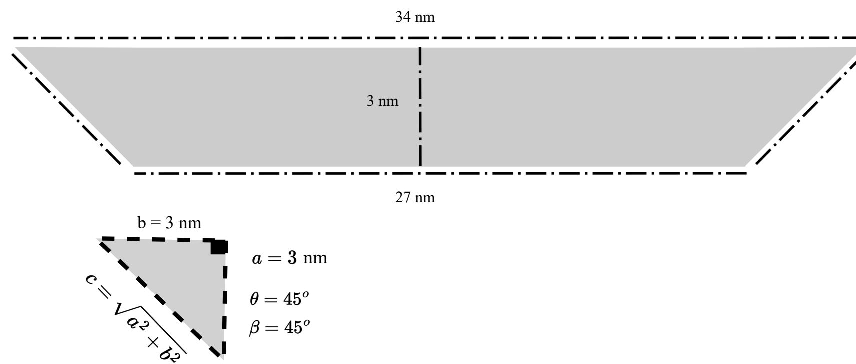

Fig. E.6: The oxide shell chosen from the STEM image, as indicated in the red line in the STEM image.

E.2 3D oxide shell model (truncated pyramid structure) for Model I (15 nm)

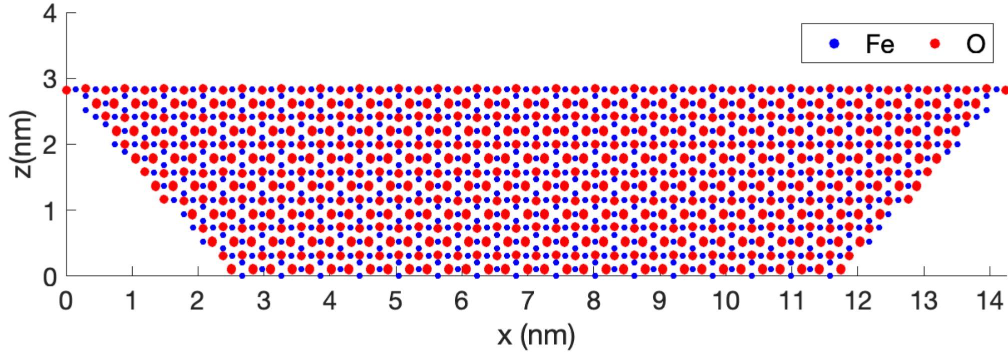

Fig. E.7: Oxide shell of Fe_3O_4. $\theta \approx 47.49$ and $\beta \approx 42.51$, and thickness is 3 nm.

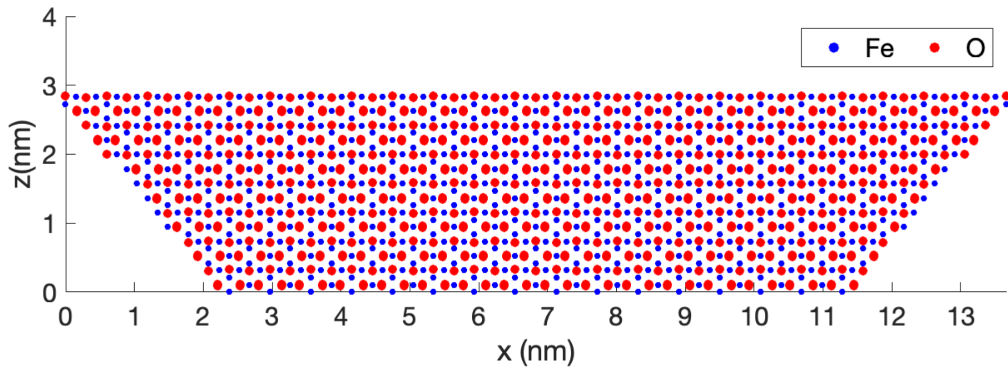

Fig. E.8: Oxide shell of Fe_3O_4. $\theta \approx 50.19$ and $\beta \approx 39.81$, and thickness is 3 nm.

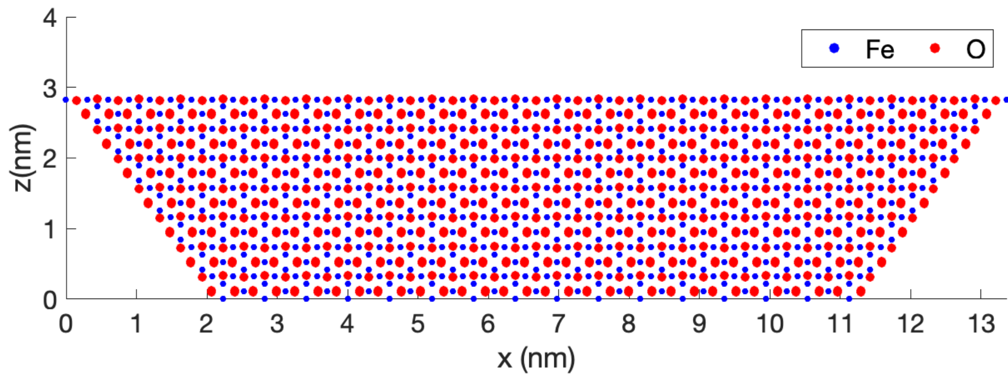

Fig. E.9: Oxide shell of Fe_3O_4. $\theta \approx 53.13$ and $\beta \approx 36.87$, and thickness is 3 nm.

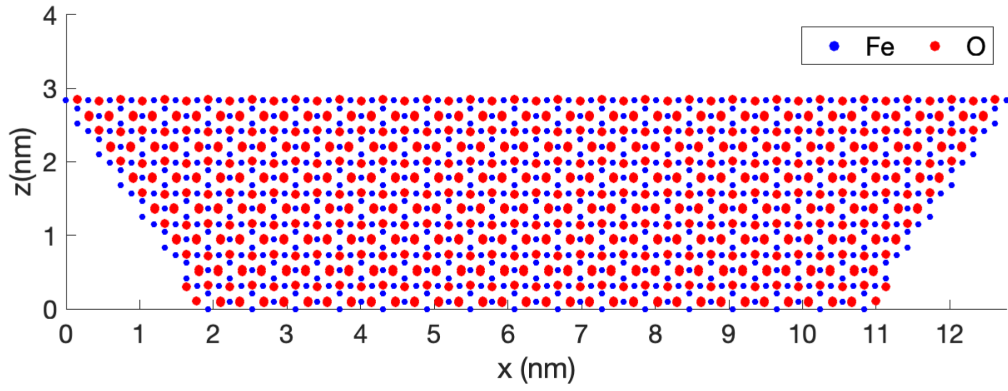

Fig. E.10: Oxide shell of Fe_3O_4. $\theta \approx 56.31$ and $\beta \approx 33.69$, and thickness is 3 nm.

E.3 Geometric Structure of Model I (15 nm)

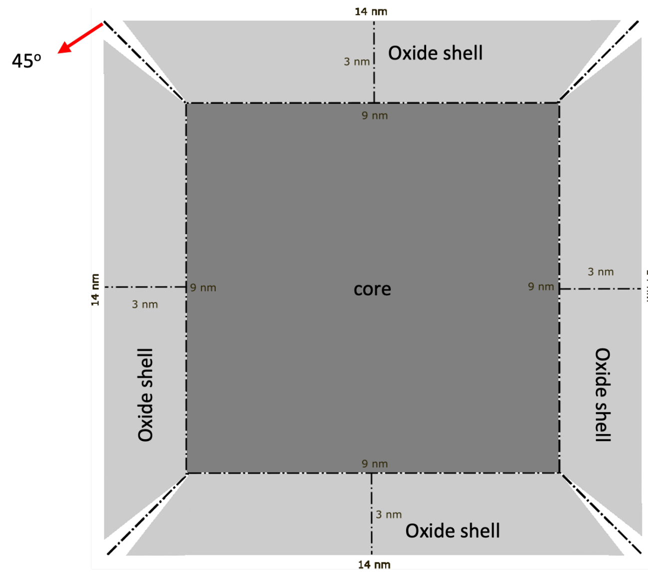

Fig. E.11: non- 45° case before applying external stress. The angles are $\theta = 50.19^o$ and $\beta = 39.81^o$.

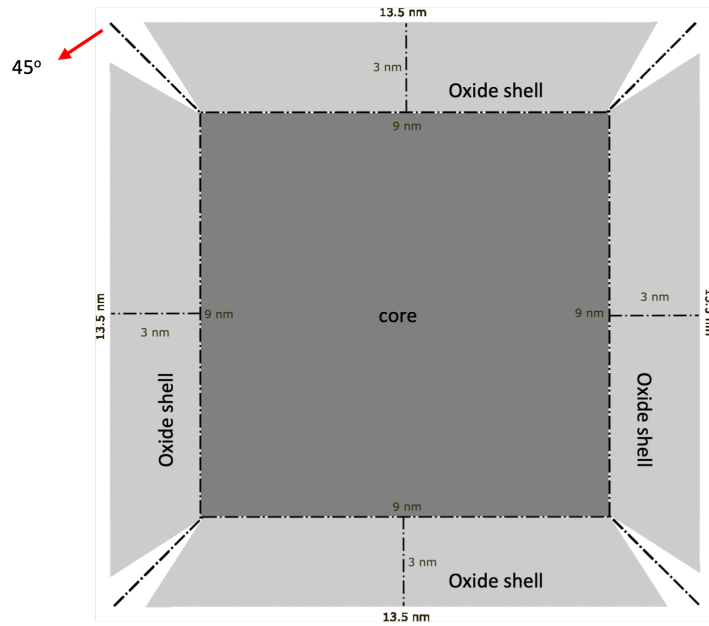

Fig. E.12: non- 45° case before applying external stress. The angles are $\theta = 53.13^o$ and $\beta = 36.87^o$.

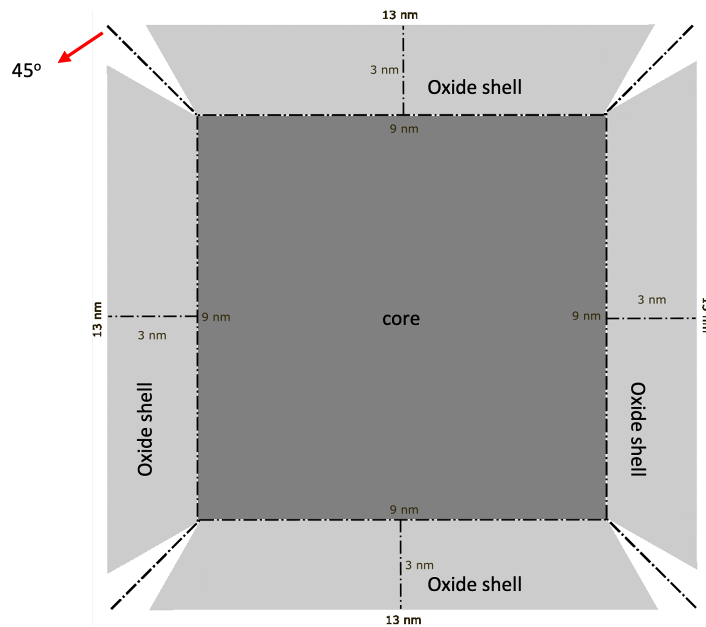

Fig. E.13: non- 45° case before applying external stress. The angles are $\theta = 56.31^o$ and $\beta = 33.69^o$.

Appendix F

Image computing

The STEM/TEM images can explain in 2D functions $f(x, y)$ as x and y spatial coordinates and an intensity f that correlates to the x and y coordinates. Digital image processing consists of a restricted number of pixel elements or arrays. In other terms, these numbers could reflect the image's intensity values which are proportional to its number [112, 83]. Therefore, image processing can be defined as a computer approach used to improve image quality and extract data from the image. This data might be used to comprehend the crystal structure of the space, reduce noise from the image or extract certain features from the experimental image using the Fast Fourier Transform (FFT) [17, 90].

The Fourier transform (FT) or Discrete Fourier Transform (DFT) algorithms facilitate comprehension of the digital image processing procedure. This algorithm's essential concept is to transform the signal domain, which is dependent on the time domain $x(t)$, to the spatial frequency $\chi(\Omega)$, whereas $\chi(\Omega)$is the frequency (rad) divided by time (sec)[113]. In other terms, the method translates an image from real space to reciprocal space and vice versa [83].

FT theory defines the decay of the periodic function $x(t)$ across an infinite series of frequency basis functions, such as the sine and cosine functions [113], as shown below.

$$x\left(t\right) = a_0 + a_1 cos\Omega_0 t + a_2 cos 2\Omega_0 t + a_3 cos 3\Omega_0 t + \ldots 1 sin\Omega_0 t + b_2 sin 2\Omega_0 t + b_3 sin 3\Omega_0 t + \ldots \quad \text{(eq. F.1)}$$

$$x\left(t\right)=a_0\sum_{t=1}^{\infty}\left(a_k\,cos\;t\,\Omega_0+b_k\,sin\;t\;\Omega\right) \quad \text{(eq. F.2)}$$

Where $\Omega=\frac{2\pi}{t}$ and $\tau=\frac{1}{f_0}$

From the equation above, the coefficients a_k and b_k can be found by integrating the above equation for one period of time, as follows

$$a_0=\frac{1}{\tau}\int_0^t x\left(t\right)\;dt \quad \text{(eq. F.3)}$$

$$a_k=\frac{1}{\tau}\int_0^t x\left(t\right)cost\;\Omega_0 dt \quad \text{(eq. F.4)}$$

$$b_k=\frac{1}{\tau}\int_0^t x\left(t\right)sin\;t\;\Omega_0 dt \quad \text{(eq. F.5)}$$

where the basis function $cos\,\Omega\;t-\;sin\,\Omega\,t=e^{-j\Omega t}$

For FT to continue, the integration is more than one period of time, so the definition of FT is shown in the following equation

$$X\left(\Omega\right)=\int_{-\infty}^{\infty}x\left(t\right)e^{-j\Omega t}dt \quad \text{(eq. F.6)}$$

where the time domain $x(t)$ signal is multiplied by the complex basis function $e^{-j\Omega t}$. As shown in the complex exponential in the equation, any given frequency domain adds up to the frequency component. As a result, the outcome of the equation is a spectrum of the time-domain signal [113].

The inverse FT equation is as follows

$$x\left(t\right)=\frac{1}{2\pi}\int_{-\infty}^{\infty}X\left(\Omega\right)e^{j\Omega t}d\Omega \quad \text{(eq. F.7)}$$

Figure F.1, F.2 shows a real space image and its reciprocal space (the FFT).

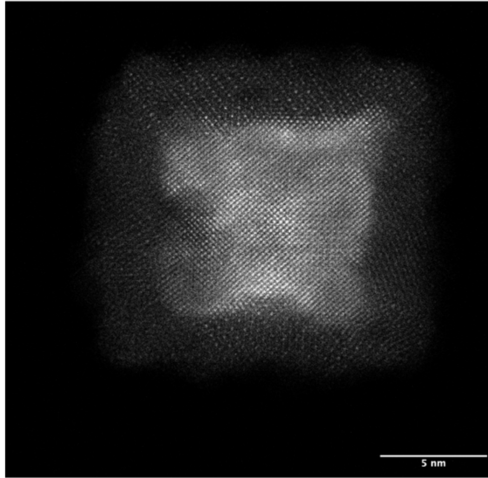

Fig. F.1: HAADF image of a core/shell Fe/Fe oxide nanoparticle.

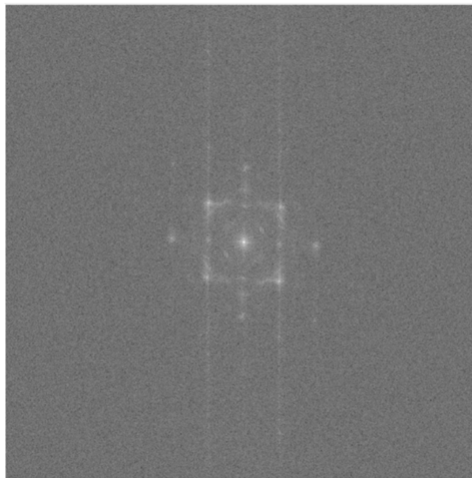

Fig. F.2: FFT of image in Fig. F.1.

F.1 Image simulation

Image simulation can be used to overcome the limitations of the experimental image because the experiential image is sensitive to many factors such as beam alignment around the optical axis, the thickness of the specimen, chromatic aberration, and beam coherence. These factors could cause background noise in the image [17, 114]. Additional information provided by image simulation is the crystal defect which includes dislocation and interfaces [115]. To demonstrate this, the aim of image simulation is twofold. First, the image simulation provides more details about the specimen and electron microscope. For example, it is possible to distinguish

whether the image's details are due to the specimen's structure or the limitations of the electron microscope instruments, such as aberration in the image or distortion. Secondly, the imaging simulation may improve the electron microscopy instrument because image simulation provides information about how the image is formed in the electron microscope, which helps to improve the instrument[114].

F.2 Image simulation method

Two methods can be used to achieve image simulation: the Bloch wave or multi-slice methods. The electron wave function in the Bloch wave method expands inside the specimen. This means that the electron wave will have a periodicity of the specimen. The advantage of using the Bloch wave is that it is used in a small, perfect crystal. However, the time required for simulation is longer. On the other hand, the multi-slice method divides the specimen into weak phase objects, calculating the electron interaction for the individual slice. It works on crystalline and amorphous specimens. Multi-slice uses the FFT which reduces the simulation time compared to the Bloch wave method [114, 116]. The current project uses the multi-slice method.

F.3 Multi-slice method

In the TEM, the electron wave is a uniform plane wave, while the STEM (the incident wave) is a focused probe. When it passes through each slice in the multi-slice method, the electron wave propagates between the slices at a small angle; the outgoing wave (Fresnel diffraction). The thickness of each slice Δz is also the distance to the following slice [114]. Figure F.3 shows the electron wave passing through the slices in the multi-slice method.

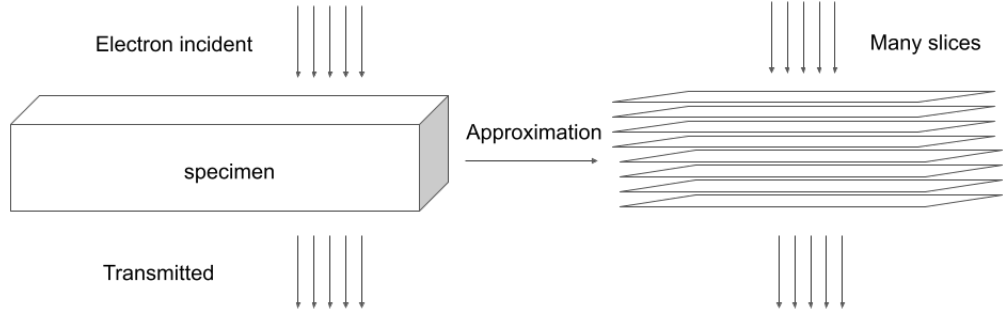

Fig. F.3: The process of electron waves passing through a specimen (left) and sliced into many thin slices (right).

When the electron wave travels through the specimen in the z-direction (along the optical axis), it follows the Schrödinger equation[83, 116]

$$\frac{\partial}{\partial z}\psi(x,y,z) = \left(\frac{-i\lambda}{4\pi}\Delta_{yx}^{2} + i\sigma V(x,y,z)\right)\psi(x,y,z) \qquad \text{(eq. F.8)}$$

Where: $\psi(x,y,z)$ is a wave function and defined as: $\psi_f(x,y,z) = \psi(x,y,z)$ $\exp(2\pi i\frac{z}{\lambda})$, the plane wave in the $z-$direction is $\exp(2\pi i\frac{z}{\lambda})$ and portion remain of wave function $\psi(x,y,z)$. λ is the wavelength of the incident electron. $\sigma e = 2\pi me\lambda/h^2$ is the interaction parameter, h is plank constant, m is electron mass, e is the electron charge. Δ_{yx}^{2} is the Laplace operator. $V(x,y,z)$ is the potential inside the specimen.

Equation (eq. F.8) can be solved using two methods: finite difference and formal operator.

Formal operator:
By inset wave-function into Eq. (eq. F.8), and taking the integration between z and $z+\Delta$, the solution is:

$$\Psi(x,y,z+\Delta z) = \exp\left(\frac{i\lambda}{4\pi}\Delta_z\Delta_{yx}^{2} + i\sigma\int_{z}^{z+\Delta} V(x,y,z^{'})dz^{'}\right)\psi(x,y,z) \qquad \text{(eq. F.9)}$$

Where Δz is slice thickness. From Eq. (eq. F.9), if Δz is a small slice, the solution for Eq. (eq. F.9) can be simplified as:

$$\psi(x,y,z+\Delta z) = \exp\left(\frac{i\lambda}{4\pi}\Delta_z\Delta_{yx}^{2} + i\sigma_e v_{\Delta z}(x,y,z)\right)\psi(x,y,z) \qquad \text{(eq. F.10)}$$

Where $v_\Delta\,(x,y,z)$ is positional inside the specimen that can be expressed as follows

$$v_{\Delta}\left(x,y,z\right)=\int^{z+\Delta_{z}} V(x,y,z^{'})dz^{'} \qquad \text{(eq. F.11)}$$

The exp (...) factor in Eq. (eq. F.10) must be considered operators, so rewriting exp $(\dots)$ in Eq. (eq. F.10) as an operator form gives:

$$\exp\left(A\epsilon+B\epsilon\right)=1+\left(A+B\right)\epsilon+\frac{1}{2!}\left(A^{2}+AB+BA+B^{2}\right)\epsilon^{2} \qquad \text{(eq. F.12)}$$

Where A and B are factors and ϵ is a small real number. In Eq. (eq. F.12), A and B are non-commuting operators or matrices.

By factoring the lowest order in Eq. (eq. F.12), the expected results are as follows.

$$\exp\left(A\epsilon+B\epsilon\right)=\exp(A\epsilon)\exp(B\epsilon)+\frac{1}{2}[B,A]\epsilon^{2}+O(\epsilon^{3}) \qquad \text{(eq. F.13)}$$

By applying the result of Eq. (eq. F.13) into Eq. (eq. F.10), the solution for multi-slice is:

$$\psi(x,y,z+\Delta z)=\exp\left(\frac{i\lambda}{4\pi}\Delta_{z}\Delta_{yx}^{2}\right)\exp[i\sigma_{e}v_{\Delta z}(x,y,z)]\psi(x,y,z)+O(\Delta z^{2})= \exp\left(\frac{i\lambda}{4\pi}\Delta_{z}\Delta_{yx}^{2}\right)t(x,y,z)\psi(x,y,z)+O(\Delta z^{2}) \qquad \text{(eq. F.14)}$$

Where $t(x,y,z)$ is the transmission function between z and $z+\Delta z$ for the portion of the sample which can be written as follow

$$t(x,y,z)=\exp\left(i\sigma_{e}\int^{z+\Delta_{z}} V(x,y,z^{'})dz^{'}\right) \qquad \text{(eq. F.15)}$$

For one slice between z and $z+\Delta z$, Eq. (eq. F.15) explains the difference between the incident beam and the weak phase object. However, the remaining factor in Eq. (eq. F.14) is a propagator function which is defined as:

$$p(x,y,\Delta z)\otimes=\exp\left(\frac{i\lambda}{4\pi}\Delta_{z}\Delta_{yx}^{2}\right) \qquad \text{(eq. F.16)}$$

The propagator function (Eq. eq. F.16) is based on Fresnel diffraction or real space for the distance between each slice (Δz). By inserting Eq. (eq. F.16) into Eq. (eq. F.14) with (Δz) and N slice $n=1,2,3...$, Eq. (eq. F.14) can be written as:

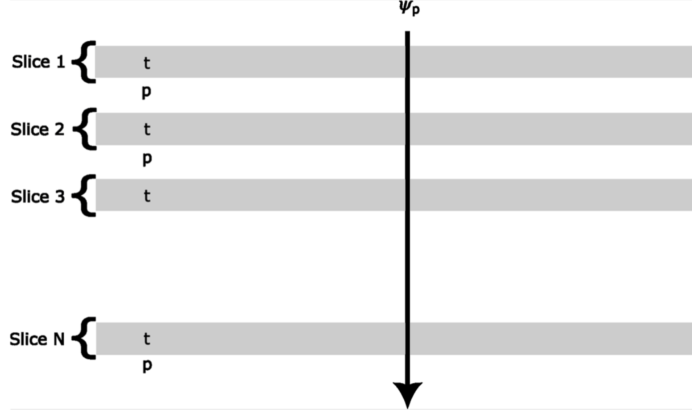

Fig. F.4: The process of the multi-slice method. $\psi_p$is the wave function transmitted (t) through the slice.

$$\psi(x, y, z + \Delta z) = p(x, y, \Delta z) \otimes t(x, y, z)\psi(x, y, z) + O(\Delta z^2) \quad \text{(eq. F.17)}$$

The mathematical explanation of the multi-slice method is shown in Eq. (eq. F.17). The first term explains the propagator function between each slice and the transmission function when the wave passes through each slice and the last term is the error term. Figure F.4 shows the multi-slice principle and indicates each term of Eq. (eq. F.17).

Appendix G

Image simulation results

G.1 Model II

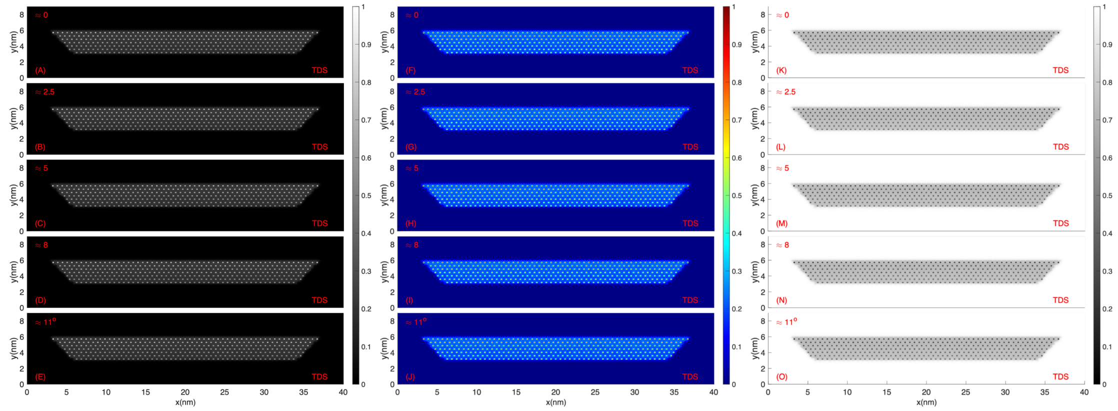

Fig. G.1: Multislice simulated Z-contrast images for model 34 nm of Fe_3O_4. Fe^{2+} columns correlate to high-intensity maxima, while Fe^{3+} columns correspond to low-intensity maxima.The angles diffidence are state in each image as $\beta = -\theta$. The 1st column(A,B,C,D,E) is dark field (DF) image. The 2nd column (F,G,H,I,J) is false-colored of DF image. The 3rd column (K,L,M,N,O)is the bright filed(BF).

G.2 Model III

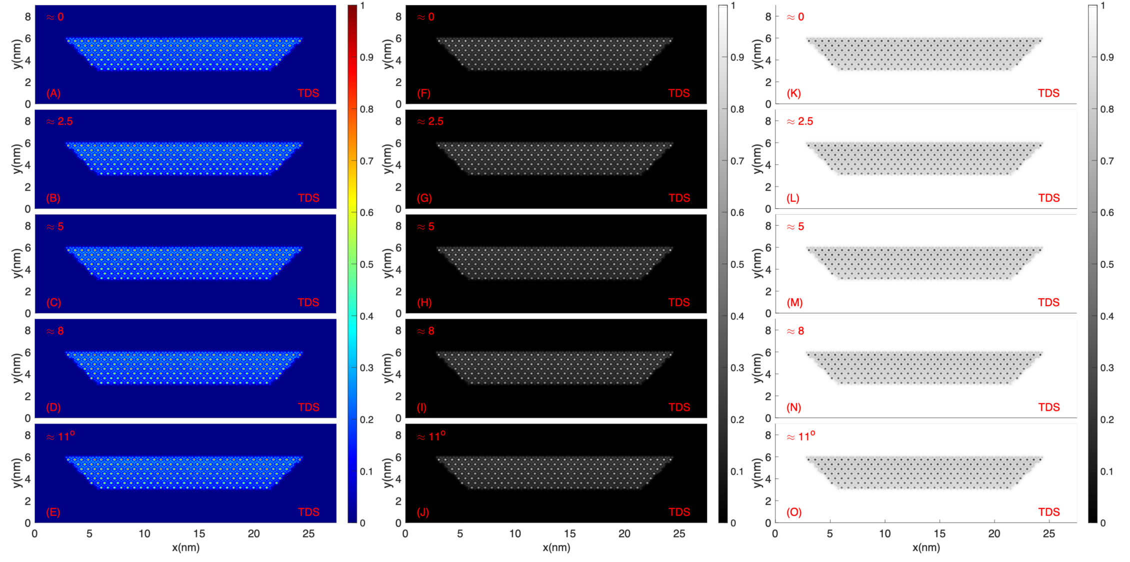

Fig. G.2: Multislice simulated Z-contrast images for model 21.5 nm of Fe_3O_4. Fe^{2+} columns correlate to high-intensity maxima, while Fe^{3+} columns correspond to low-intensity maxima.The angles diffidence are state in each image as $\beta = -\theta$. The 1st column(A,B,C,D,E) is dark field (DF) image. The 2nd column (F,G,H,I,J) is false-colored of DF image. The 3rd column (K,L,M,N,O)is the bright filed(BF).

G.3 Model IV

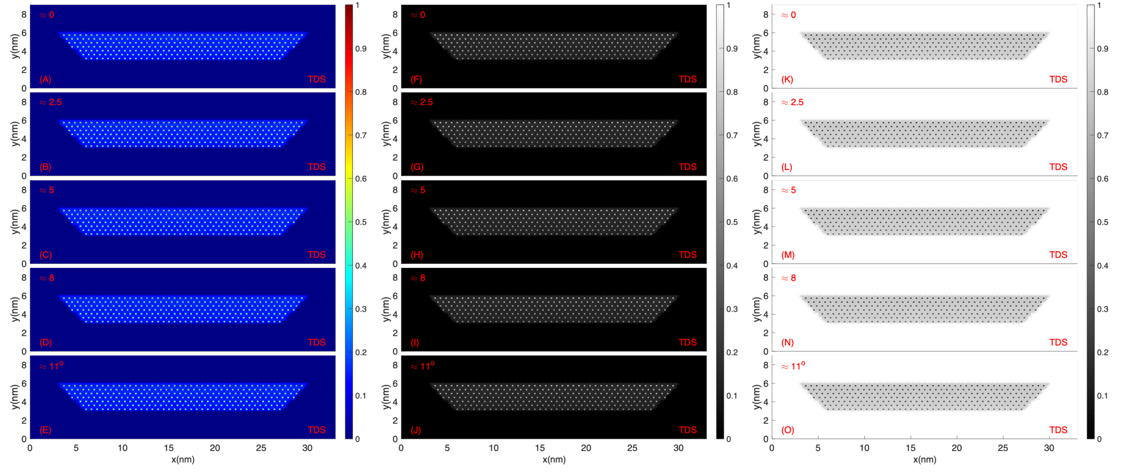

Fig. G.3: Multislice simulated Z-contrast images for model 27 nm of Fe_3O_4. Fe^{2+} columns correlate to high-intensity maxima, while Fe^{3+} columns correspond to low-intensity maxima.The angles diffidence are state in each image as $\beta = -\theta$. The 1st column(A,B,C,D,E) is dark field (DF) image. The 2nd column (F,G,H,I,J) is false-colored of DF image. The 3rd column (K,L,M,N,O)is the bright filed(BF).

Appendix H

Intensity profile for Model III and Model IV

H.1 Model III

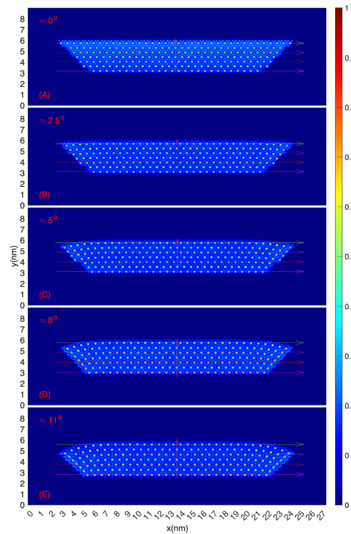

Fig. H.1: Multislice simulated Z-contrast images of Fe_3O_4 for 21.5 nm model. Fe^{2+} columns correlate to high-intensity maxima, while Fe^{3+} columns correspond to low-intensity maxima. The angles diffidence are state in each image as $\beta = -\theta$. (A) is non-displaced, (B) = 0.5 nm displacement, (C) is 1 nm displacement, (D) is 1.5 nm displacement and (E) is 2 nm displacement. The arrows direction is representing the line profile direction. The image simulation is a colored mapping of the DF images.

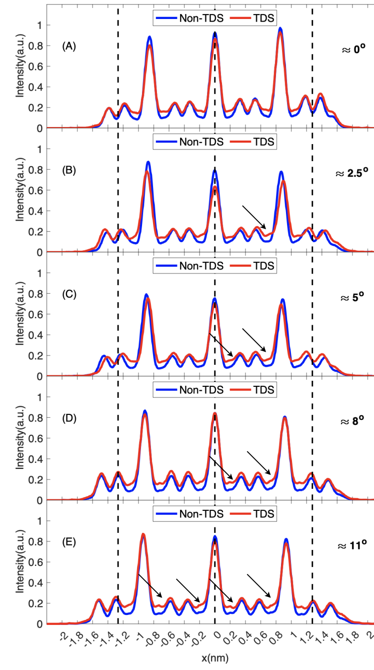

Fig. H.2: Line profile taken in y-axis direction as in red arrow in Fig. H.1. (A) shows the non-displaced model, while the other four line profile (show displaced model as shown in Table 4.3 (see chapter 4). The angles diffidence are stated in each plot as $\beta = -\theta$ as in Fig. 4.33 (see chapter 4). The black arrows point towards the shoulders of the maxima. The dashed line separates the model without displacement from the model with displacement.

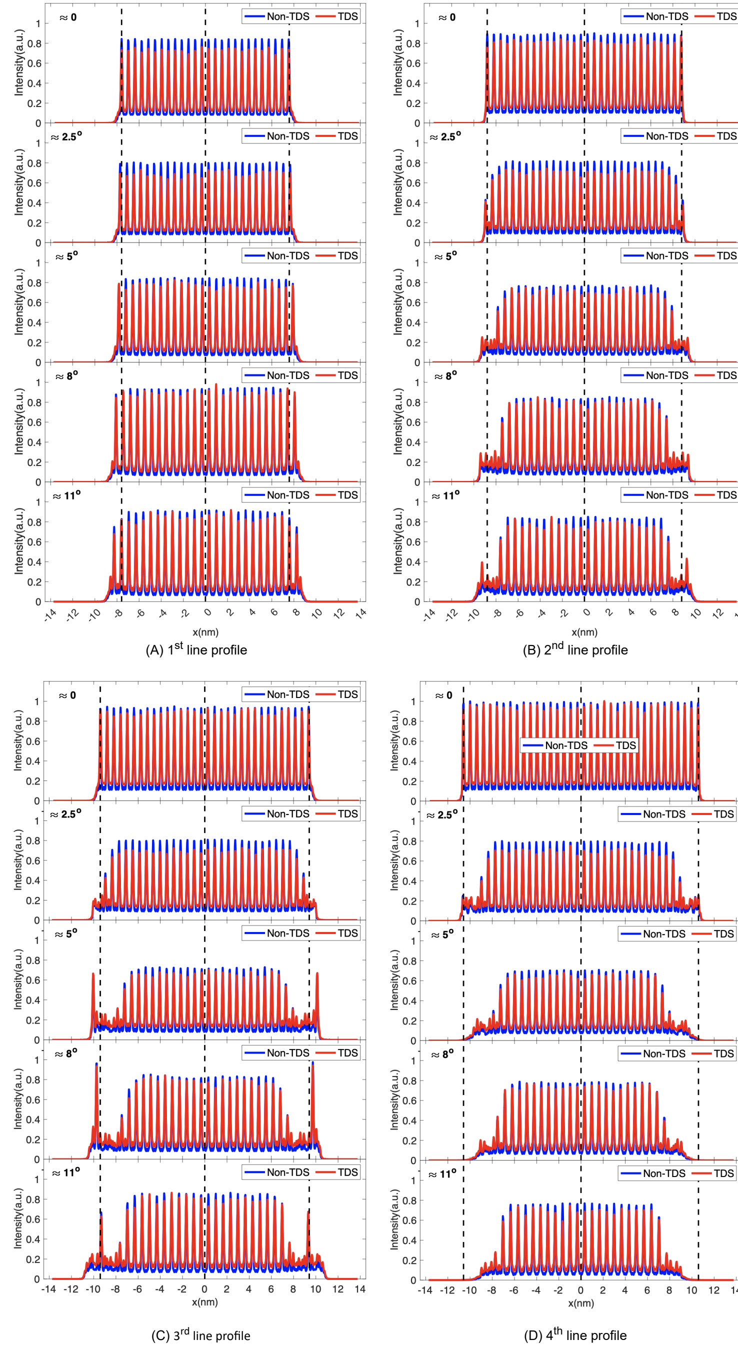

Fig. H.3: Four intensity profiles were taken in x-axis direction as shown in magenta, brown, purple and green arrows in Fig. H.1. The black dished line separate the non displaced column from displaced column. The zero angle is non-displaced column. The angles diffidence are state in each image as $\beta = -\theta$.

H.2 Model IV

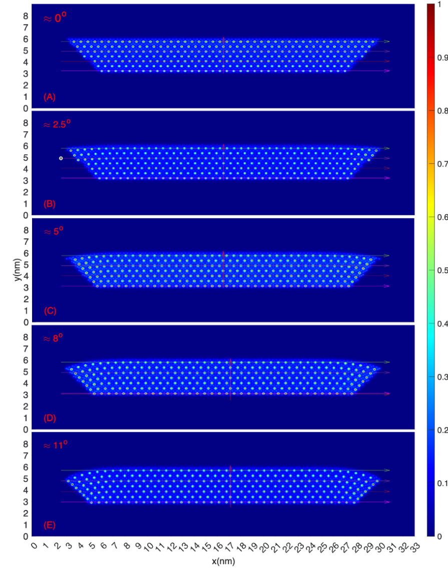

Fig. H.4: Multislice simulated Z-contrast images of Fe_3O_4 for 27 nm model. Fe^{2+} columns correlate to high-intensity maxima, while Fe^{3+} columns correspond to low-intensity maxima.The angles diffidence are state in each image as $\beta = -\theta$. (A) is non-displaced, (B) = 0.5 nm displacement, (C) is 1 nm displacement, (D) is 1.5 nm displacement and (E) is 2 nm displacement. The arrows direction is representing the line profile direction. The image simulation is a colored mapping of the DF images.

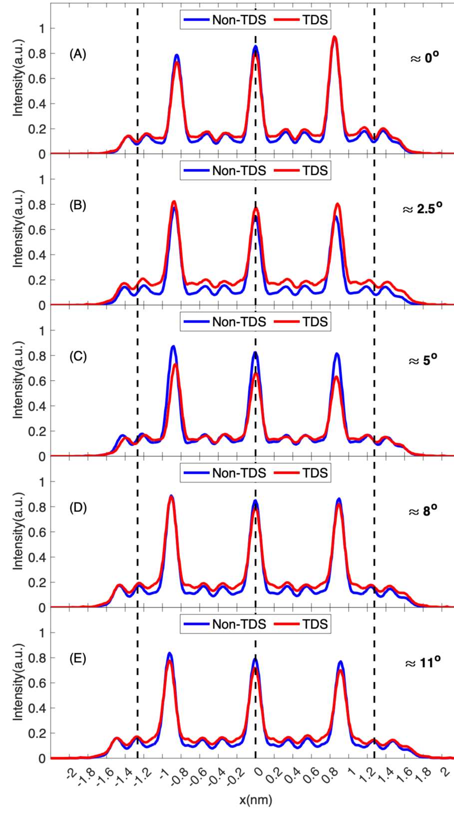

Fig. H.5: Line profile taken in y-axis direction as in red arrow in Fig. H.4. (A) shows the non-displaced model, while the other four line profile (show displaced model as shown in Table 4.3 (see chapter 4). The angles diffidence are state in each plot as $\beta = -\theta$ as in Fig. 4.33 (see chapter 4). The black arrows point towards the shoulders of the maxima. The dashed line separates the model without displacement from the model with displacement.

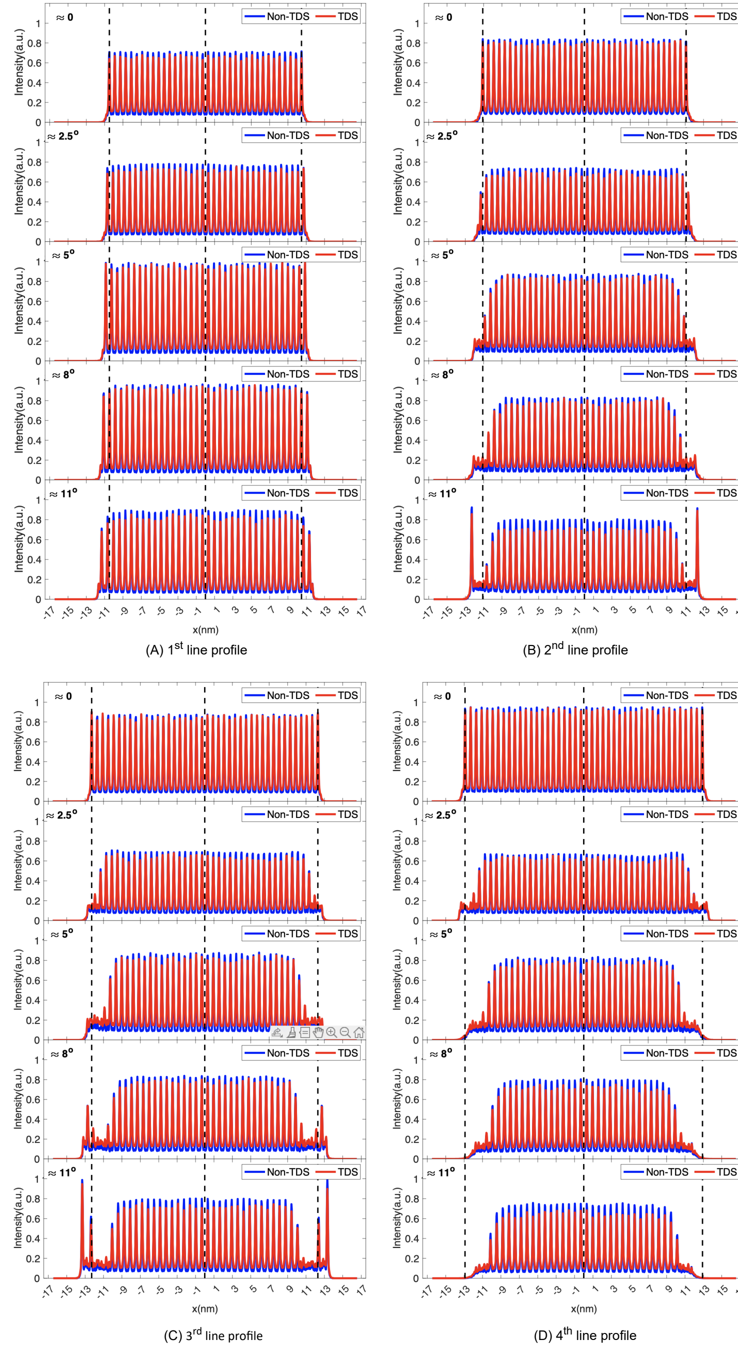

Fig. H.6: Four intensity profiles were taken in x-axis direction as shown in magenta, brown, purple and green arrows in Fig. H.4. The black dished line separate the non displaced column from displaced column. The zero angle is non-displaced column. The angles diffidence are state in each image as $\beta = -\theta$.

Appendix I

Displacement filed mapping

I.1 Model I

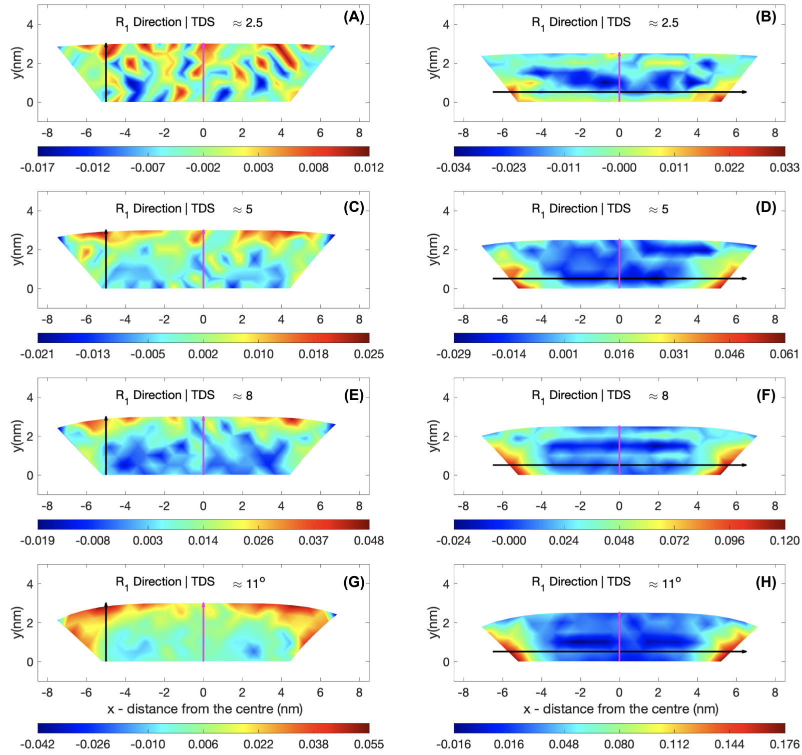

Fig. I.1: Displacement field mapping of model 15 nm. The displacement field mapping in R_1 direction is in (A,C,E,G) with 2.5^o, 5°, 8° and 11° angles, respectively. Displacement field in R_2 direction is in (B,D,F,H) with 2.5^o, 5°, 8° and 11° angles, respectively.

I.2 Model II

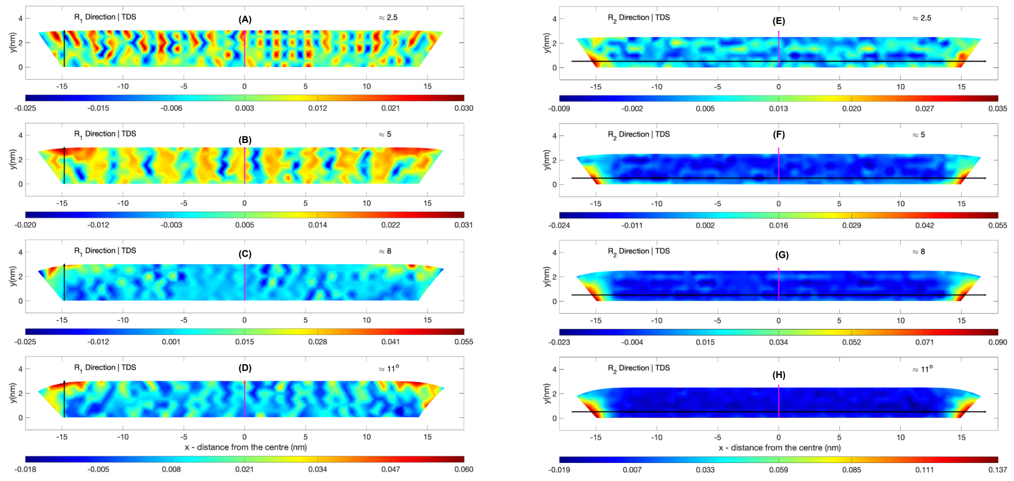

Fig. I.2: Displacement field mapping of model 34 nm. The displacement field mapping in R_1 direction is in (A,C,E,G) with 2.5^o, 5°, 8° and 11° angles, respectively. Displacement field in R_2 direction is in (B,D,F,H) with 2.5^o, 5°, 8° and 11° angles, respectively.

I.3 Model III

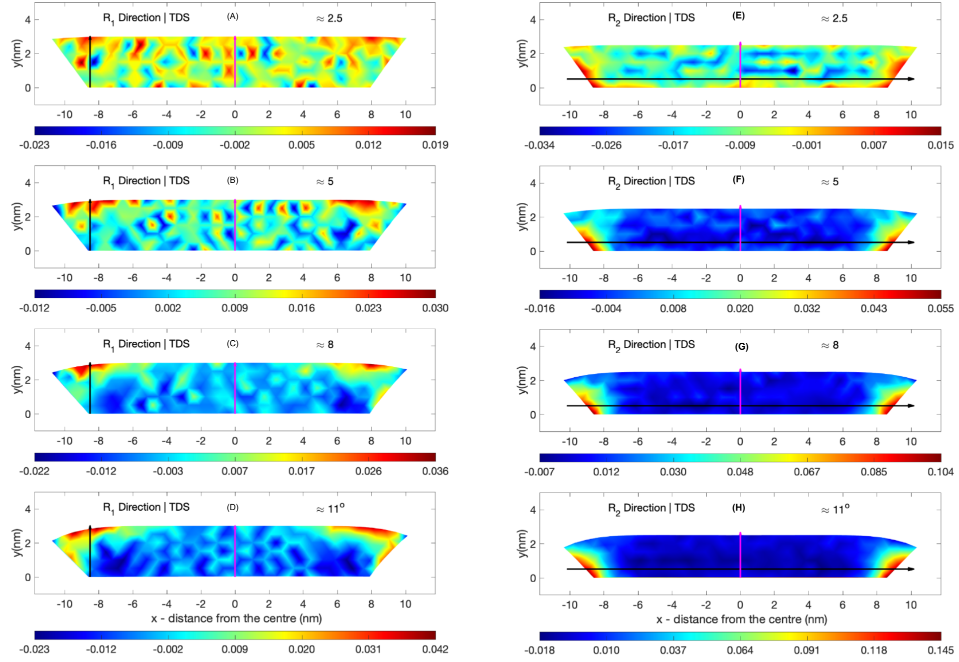

Fig. I.3: Displacement field mapping of model 21.5 nm. (A,C,E,G) with 2.5^o, 5°, 8° and 11° angles, respectively represent the displacement field mapping in R_1 direction. (B,D,F,H) with 2.5^o, 5°, 8° and 11° angles, respectively, display the displacement field in R_2 direction.

Table I.1: displacement field and parameter used for 21.5 nm model.

Model	$\approx L_i$ nm	$\approx L_b$ nm	$\approx L_f$ nm	$\approx$ d nm	$\approx$ angle
2	21	15.5	21.5	0.5	2.5
3	20.5	15.5	21.5	1	5
4	20	15.5	21.5	1.5	8
5	19.5	15.5	21.5	2	11

L_i is oxide segment top length model before the displacement field is applied, L_b is oxide segment bottom length where the core and shell meet, L_f is oxide segment top length model after the displacement field is applied, d is the displacement field, and the angle is the differences between the model without displacement and the model with displacement.

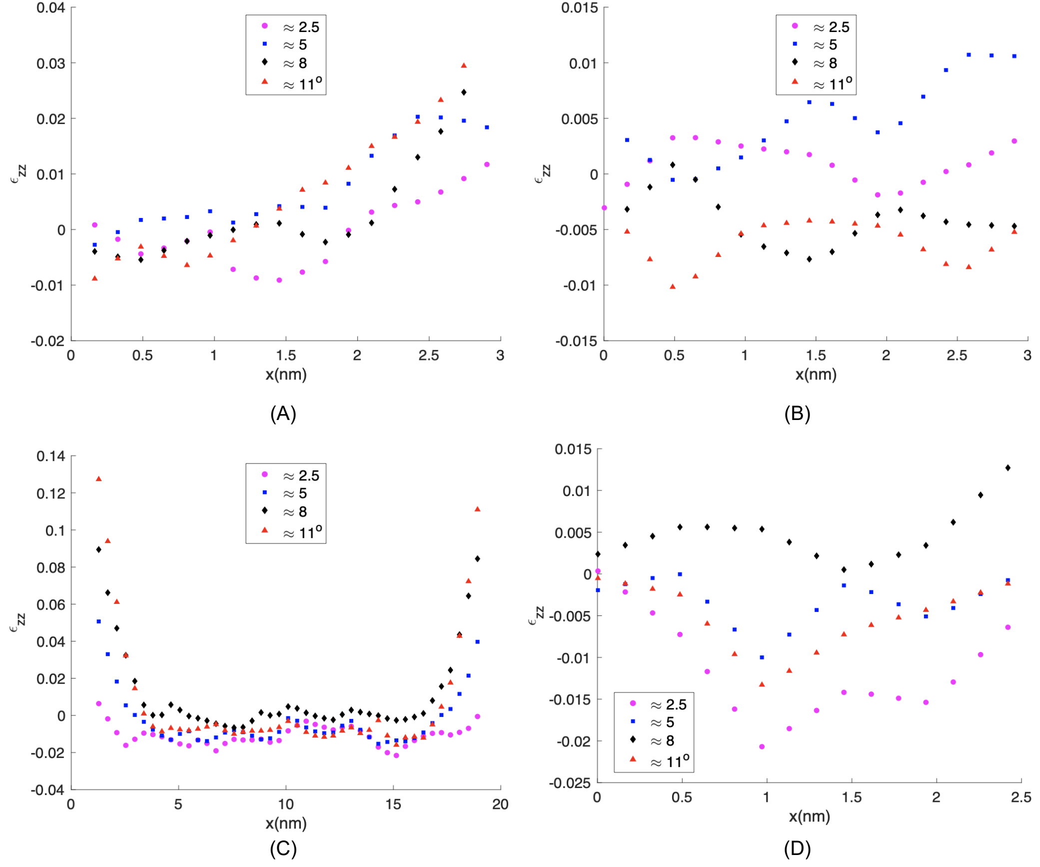

Fig. I.4: Line profile plot of model 21.5 nm. Two line profiles were conducted for different displacement field values applied to the model, as shown in Table I.1. (A) and (B): Data obtained from a line profile close to the edge and centre, as indicated by the solid black arrows and magenta arrows, respectively in the displacement field mapping in R_1, as shown in Fig. I.3 (A,B,C,D). Data obtained from a line profile in the displacement field mapping in R_2 are in (C) and (D). (C) line profile from the left to the right as in the black arrows and (D) line profile from the centre as in magenta arrows as in Fig. I.3 (E,F,G,H).

I.4 Model IV

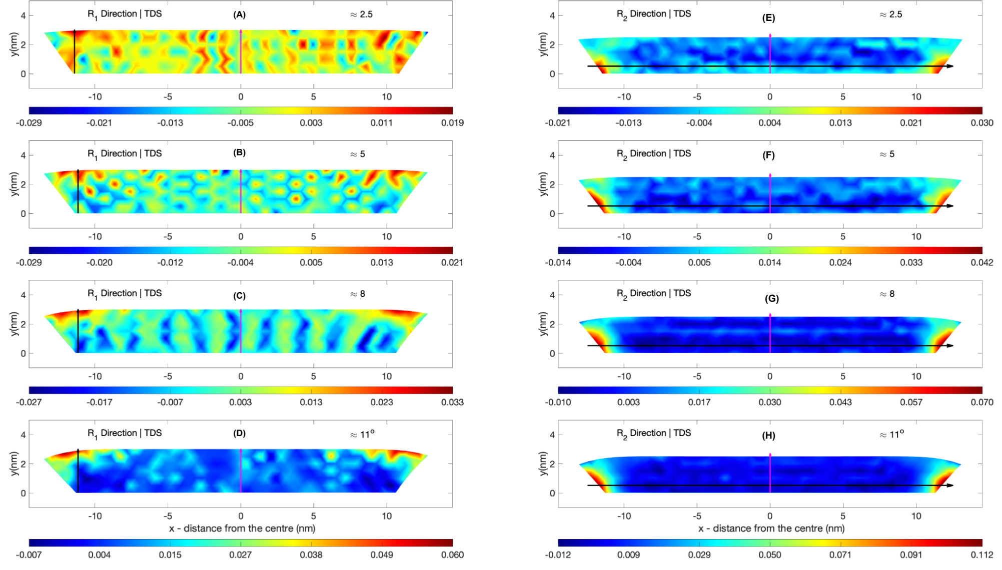

Fig. I.5: Displacement field mapping of model 27 nm. (A,B,C,D) with 2.5^o, 5°, 8° and 11° angles, respectively represent the displacement field mapping in R$_1$ direction. (E,F,G,H) with 2.5^o, 5°, 8° and 11° angles, respectively, display the displacement field in R$_2$ direction.

Table I.2: displacement field and parameter used for 27 nm model.

Model	$\approx L_i$ nm	$\approx L_b$ nm	$\approx L_f$ nm	$\approx$ d nm	$\approx$ angle
2	26.5	21	27	0.5	2.5
3	26	21	27	1	5
4	25.5	21	27	1.5	8
5	25	21	27	2	11

L_i is oxide segment top length model before the displacement field is applied, L_b is oxide segment bottom length where the core and shell meet, L_f is oxide segment top length model after the displacement field is applied, d is the displacement field, and the angle is the differences between the model without displacement and the model with displacement.

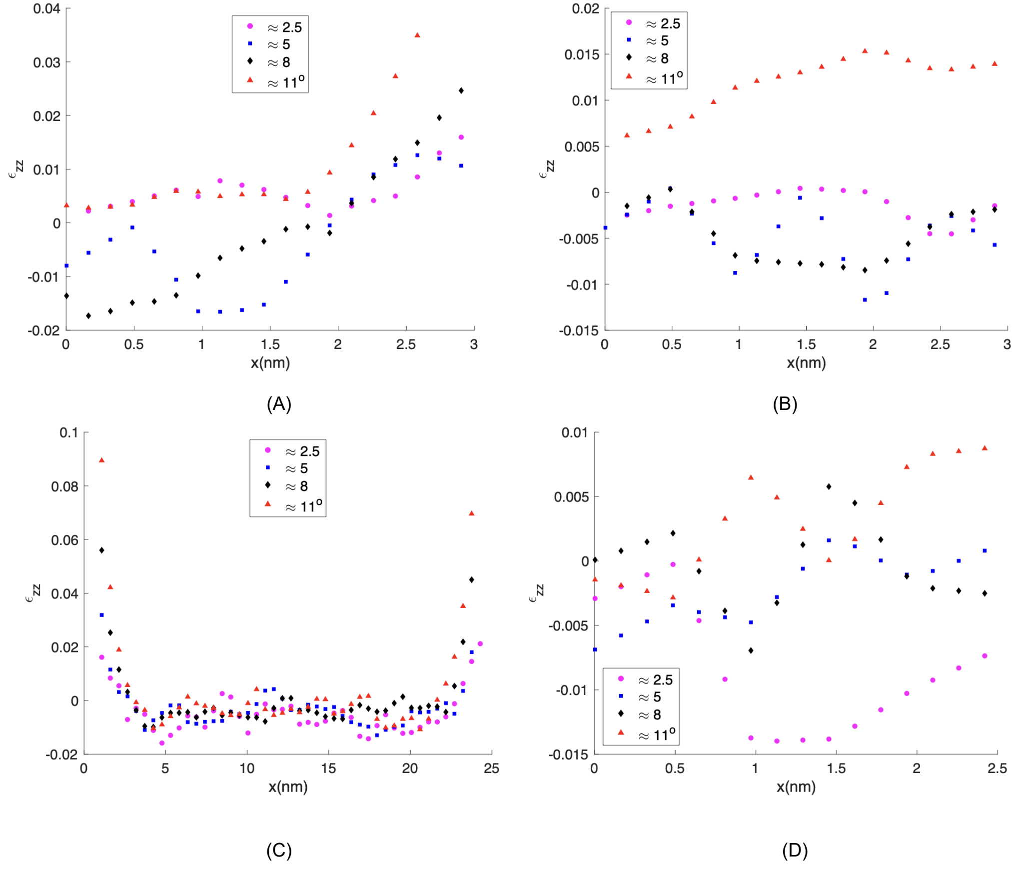

Fig. I.6: Line profile plot of model 27 nm. Two line profiles were conducted for different displacement field values applied to the model, as shown in Table I.2. (A) and (B): Data obtained from a line profile close to the edge and centre, as indicated by the solid black arrows and magenta arrows, respectively in the displacement field mapping in R_1, as shown in Fig. I.5 (A,B,C,D). Data obtained from a line profile in the displacement field mapping in R_2 are in (C) and (D). (C) line profile from the left to the right as in the black arrows and (D) line profile from the centre as in magenta arrows as in Fig. I.5 (E,F,G,H).

Bibliography

[1] Blake RL, Hessevick RE, Zoltai T, Finger LW. Refinement of the hematite structure. American Mineralogist. 1966;51:123-9. Available from: https://www.crystallography.net/cod/9000139.html.

[2] Pecharroman C, Gonzalez-Carreno T, Iglesias JE. The infrared dielectric properties of maghemite, gamma-Fe2O3, from reflectance measurement on pressed powders. Physics and Chemistry of Minerals. 1995;22:21-9.

[3] C OHS, Dollase WA. Crystal structures and cation distributions in simple spinels from powder XRD structural refinements: MgCr2O4, ZnCr2O4, Fe3O4 and the temperature dependence of the cation distribution in ZnAl2O4 Sample: Fe3O4, results from data collected at BGI (MoKalpha1) radiation. Physics and Chemistry of Minerals. 1994;20:541-55. Available from: https://www.crystallography.net/cod/9006189.html.

[4] Fjellvåg H, Hauback BC, Vogt T, Stølen S. Monoclinic nearly stoichiometric wüstite at low temperatures. American Mineralogist. 2002 02;87(2-3):347-9.

[5] Philibert JM. In: Atom Movements-Diffusion and Mass Transport in Solids. EDP Sciences; 2012. p. 1-30, 61-92.

[6] Pelleg J. In: Diffusion in ceramics. Springer; 2016. p. 3-20, 31-45.

[7] Mehrer H. In: Diffusion in Solids : Fundamentals, Methods, Materials, Diffusion-Controlled Processes. Springer; 2007. p. 95-104, 546-52, 533-82.

[8] Hoffrogge P, Barrales-Mora LA. Grain reconstruction and determination of grain attributes from MD data sets of FCC polycrystals; 2018. Accessed: 2023-12-13.

[9] Lejcek P. In: Grain boundary segregation in metals. vol. 136. Springer Science and Business Media; 2010. p. 1-12, 190-4.

[10] Herzig C, Mishin Y. In: Heitjans P, Kärger J, editors. Grain Boundary Diffusion in Metals. Berlin, Heidelberg: Springer Berlin Heidelberg; 2005. p. 337-66.

[11] Cabrera N, Mott NF. THEORY OF THE OXIDATION OF METALS. Reports on Progress in Physics. 1948 1;12:163-84.

[12] Brault P, Chamorro-Coral W, Chuon S, Caillard A, Bauchire JM, Baranton S, et al. Molecular dynamics simulations of initial Pd and PdO nanocluster growth in a magnetron gas aggregation source. Frontiers of Chemical Science and Engineering. 2019;13(2):324.

[13] Kirchenbuechler D, Mutsafi Y, Horowitz B, Levin-Zaidman S, Fass D, Wolf SG, et al. Cryo-STEM tomography of intact vitrified fibroblasts. AIMS Biophysics. 2015;2(3):259-73.

[14] Nellist PD. The principles of STEM imaging. In: Scanning Transmission Electron Microscopy. Springer; 2011. p. 91-115.

[15] Christoph TK. Determination of core structure periodicity and point defect density along dislocations; 2002.

[16] Javed Y, Ali K, Akhtar K, Jawaria, Hussain MI, Ahmad G, et al. TEM for Atomic-Scale Study: Fundamental, Instrumentation, and Applications in Nanotechnology. In: Sharma SK, editor. Handbook of Materials Characterization. Cham: Springer International Publishing; 2018. p. 147-216.

[17] Carter CB, Williams DB. In: Transmission electron microscopy: Diffraction, imaging, and spectrometry. Springer; 2016. p. 97, 122, 141-72, 371-88.

[18] Scherzer O. The theoretical resolution limit of the electron microscope. Journal of Applied Physics. 1949;20(1):20-9.

[19] Thomas J, Gemming T. In: Analytical transmission electron microscopy: an introduction for operators. Springer Science and Business; 2014. p. 115-327.

[20] Cornell RM, Schwertmann U. In: The Iron Oxides: Structure, Properties, Reactions, Occurrences and Uses. John Wiley and Sons; 2003. p. 1-38.

[21] Parkinson GS. Iron oxide surfaces. Surface Science Reports. 2016;71:272-365.

[22] Pratt A. Chapter 7 - Environmental Applications of Magnetic Nanoparticles. In: Binns C, editor. Nanomagnetism: Fundamentals and Applications. vol. 6 of Frontiers of Nanoscience. Elsevier; 2014. p. 259-307.

[23] Gudkov SV, Burmistrov DE, Serov DA, Rebezov MB, Semenova AA, Lisitsyn AB. Do Iron Oxide Nanoparticles Have Significant Antibacterial Properties? Antibiotics. 2021;10(7).

[24] Akbarzadeh A, Samiei M, Davaran S. Magnetic nanoparticles: preparation, physical properties, and applications in biomedicine. Nanoscale Research Letters. 2012;7:144.

[25] Zhou K, Zhou X, Liu J, Huang Z. Application of magnetic nanoparticles in petroleum industry: A review. Journal of Petroleum Science and Engineering. 2020;188:106943.

[26] Xu L, Liang HW, Yang Y, Yu SH. Stability and reactivity: positive and negative aspects for nanoparticle processing. Chemical reviews. 2018;118(7):3209-50.

[27] Chernavskii PA, Peskov NV, Mugtasimov AV, Lunin VV. Oxidation of metal nanoparticles: Experiment and model. Russian Journal of Physical Chemistry B. 2007;1:394-411.

[28] Taylor M. Investigation of Novel Nanoparticles for Biomedical Applications. University of York; 2018.

[29] Aktaş S, Thornton SC, Binns C, Lari L, Pratt A, Kröger R, et al. Control of gas phase nanoparticle shape and its effect on MRI relaxivity. Materials Research Express. 2015 1;2:35002.

[30] Pratt A, Lari L, Hovorka O, Shah A, Woffinden C, Tear SP, et al. Enhanced oxidation of nanoparticles through strain-mediated ionic transport. Nature materials. 2014;13(1):26-30.

[31] Gammer C, Richard MI, Eberl C. Measurement of local strain. MRS Bulletin. 2019;44:459-64.

[32] MATLAB. version(R2022a). The MathWorks Inc.; 2022.

[33] COMSOL. COMSOL: Multiphysics Software for Optimizing Designs, v5.6;. Available from: https://www.comsol.com/.

[34] Perovic DD, Rossouw CJ, Howie A. Imaging elastic strains in high-angle annular dark field scanning transmission electron microscopy. Ultramicroscopy. 1993;52:353-9.

[35] Phillips PJ, Graef MD, Kovarik L, Agrawal A, Windl W, Mills MJ. Atomic-resolution defect contrast in low angle annular dark-field STEM. Ultramicroscopy. 2012;116:47-55.

[36] Lee JL, Silcox J. Annular dark-field image simulation of the YBa2Cu3O7-δ/BaF2 interface. Ultramicroscopy. 2000;84:65-74.

[37] Yu Z, Muller DA, Silcox J. Study of strain fields at a-Si/c-Si interface. Journal of Applied Physics. 2004;95:3362-71.

[38] Wu X, Baribeau JM. Composition and strain contrast of Si 1- x Ge x (x= 0.20) and Si 1- y C y (y $\leq$ 0.015) epitaxial strained films on (100) Si in annular dark field images. Journal of Applied Physics. 2009;105(4):043517.

[39] Galindo PL, Kret S, Sanchez AM, Laval JY, Yáñez A, Pizarro J, et al. The Peak Pairs algorithm for strain mapping from HRTEM images. Ultramicroscopy. 2007 11;107:1186-93.

[40] Chen JS, Liu Y, Zhai Y, Fan TX. A new method to reliably determine elastic strain of various crystal structures from atomic-resolution images. Scientific Reports. 2019;9:16399.

[41] Gamler JTL, Leonardi A, Sang X, Koczkur KM, Unocic RR, Engel M, et al. Effect of lattice mismatch and shell thickness on strain in core@shell nanocrystals. Nanoscale Advances. 2020;2:1105-14.

[42] Béché A, Rouvière JL, Barnes JP, Cooper D. Strain measurement at the nanoscale: Comparison between convergent beam electron diffraction, nano-beam electron diffraction, high resolution imaging and dark field electron holography. Ultramicroscopy. 2013 8;131:10-23.

[43] De Wolf I, Senez V, Balboni R, Armigliato A, Frabboni S, Cedola A, et al. Techniques for mechanical strain analysis in sub-micrometer structures: TEM/CBED, micro-Raman spectroscopy, X-ray micro-diffraction and modeling. Microelectronic engineering. 2003;70(2-4):425-35.

[44] Rosenauer A. Transmission electron microscopy of semiconductor nanostructures: an analysis of composition and strain state. vol. 182. Springer Science and Business Media; 2003.

[45] Kret S, Ruterana P, Rosenauer A, Gerthsen D. Extracting Quantitative Information from High Resolution Electron Microscopy. physica status solidi (b). 2001 9;227:247-95.

[46] Tanaka N, Saitoh K. Chapter 3. In: Basics of STEM. World Scientific; 2014. p. 41-108.

[47] Ponchet A, Gatel C, Roucau C, Casanove MJ. Strain Analysis in Transmission Electron Microscopy: How Far can we go? Mechanical Stress on the Nanoscale: Simulation, Material Systems and Characterization Techniques. 2011:189-212.

[48] Hÿtch MJ, Snoeck E, Kilaas R. Quantitative measurement of displacement and strain fields from HREM micrographs. Ultramicroscopy. 1998;74:131-46.

[49] Bierwolf R, Hohenstein M, Phillipp F, Brandt O, Crook GE, Ploog K. Direct measurement of local lattice distortions in strained layer structures by HREM. Ultramicroscopy. 1993 2;49:273-85.

[50] Jouneau PH, Tardot A, Feuillet G, Mariette H, Cibert J. Strain mapping of ultrathin epitaxial ZnTe and MnTe layers embedded in CdTe. Journal of Applied Physics. 1994 6;75:7310-6.

[51] Seitz H, Seibt M, Baumann FH, Ahlborn K, Schröter W. Quantitative strain mapping using high-resolution electron microscopy. physica status solidi (a). 1995 8;150:625-34.

[52] Stenkamp D, Jäger W. Compositional and structural characterization of SixGe1-x alloys and heterostructures by high-resolution transmission electron microscopy. Ultramicroscopy. 1993;50:321-54.

[53] Fuhrhop JH, Wang T. Chapter 4: Iron. In: Metallic and Molecular Interactions in Nanometer Layers, Pores and Particles: New Findings at the Yoctolitre Level. The Royal Society of Chemistry; 2009. .

[54] Teja AS, Koh PY. Synthesis, properties, and applications of magnetic iron oxide nanoparticles. Progress in Crystal Growth and Characterization of Materials. 2009;55:22-45.

[55] Bhargava A, Elbaz Y, Sam Q, Smeaton MA, Kourkoutis LF, Caspary Toroker M, et al. Enhanced Li-ion diffusion and electrochemical performance in strained-manganese–iron oxide core–shell nanoparticles. The Journal of Chemical Physics. 2021;155(14).

[56] Mishin Y. In: Gupta D, editor. Atomistic Computer Simulation of Diffusion. Berlin, Heidelberg: Springer Berlin Heidelberg; 2005. p. 113-71.

[57] Callister WD, Rethwisch DG, et al. Materials science and engineering: an introduction. vol. 7. 7th ed. John wiley and sons New York; 2007.

[58] Pelleg J. In: Diffusion in the Iron Group L12 and B2 Intermetallic Compounds. Springer; 2016. p. 1-20.

[59] Wolfram Research I. Technical data for Oxygen;. Accessed: 2024-01-21. Available from: `https://periodictable.com/Elements/008/data.html`.

[60] Wolfram Research I. Technical data for Iron;. Accessed: 2024-01-21. Available from: `https://periodictable.com/Elements/026/data.html`.

[61] Shewmon PG. In: Diffusion in Solids. vol. Second edi. Springer; 2016. p. 53-68, 189-93.

[62] Meijerink MJ, de Jong KP, Zečević J. Assessment of oxide nanoparticle stability in liquid phase transmission electron microscopy. Nano Research. 2019;12:2355-63.

[63] Balakrishnan V. Theory of the Gorsky effect for low interstitial concentrations. Pramana. 1978;11:389-409.

[64] Sinning HR. The intercrystalline Gorsky effect. Materials Science and Engineering: A. 2004;370(1-2):109-13.

[65] Vystavel T, Palasantzas G, Koch SA, Hosson JTMD. Nanosized iron clusters investigated with in situ transmission electron microscopy. Applied Physics Letters. 2003;82:197-9.

[66] D'Addato S, Spadaro MC. Low pressure bottom-up synthesis of metal@ oxide and oxide nanoparticles: Control of structure and functional properties. Physica Scripta. 2018;93.

[67] Qiang Y, Duscher G, Wang CM, Antony J, Thomas LE, Baer DR, et al. Void formation during early stages of passivation: Initial oxidation of iron nanoparticles at room temperature. Journal of Applied Physics. 2005;98:094308.

[68] Zhdanov VP. Kinetic model of oxidation of metal nanoparticles: Cabrera-Mott and Kirkendall effects. Surface Science. 2019;684:24-7.

[69] Yin Y. Formation of Hollow Nanocrystals Through the Nanoscale Kirkendall Effect. Science. 2004 1;304:711-4.

[70] Fromhold Jr AT, Fromhold RG. An overview of metal oxidation theory. Comprehensive Chemical Kinetics. 1984;21:1-117.

[71] Mott NF. The theory of the formation of protective oxide films on metals.—III. Transactions of the Faraday Society. 1947;43:429-34.

[72] Ermoline A, Dreizin EL. Equations for the Cabrera–Mott kinetics of oxidation for spherical nanoparticles. Chemical Physics Letters. 2011 1;505:47-50.

[73] Atkinson A. Transport processes during the growth of oxide films at elevated temperature. Reviews of Modern Physics. 1985 4;57:437-70.

[74] Morin F, Beranger G, Lacombe P. Limits of application for Wagner's oxidation theory. Oxidation of Metals. 1972;4:51-62.

[75] Tang J, Myers M, Bosnick KA, Brus LE. Magnetite Fe3O4 nanocrystals: spectroscopic observation of aqueous oxidation kinetics. The Journal of Physical Chemistry B. 2003;107:7501-6.

[76] Wegner K, Piseri P, Tafreshi HV, Milani P. Cluster beam deposition: a tool for nanoscale science and technology. Journal of Physics D: Applied Physics. 2006 1;39:R439-59.

[77] Dexter K. Novel Magnetic Nanoparticles for Medical Applications; 2018.

[78] Aktas S. Gas phase preparation of magnetic nanoparticle hydrosols; 2014.

[79] De Toro JA, Normile PS, Binns C. 3. In: Types of Cluster Sources. John Wiley and Sons, Ltd; 2017. p. 39-55.

[80] Hébert C, Alexander D. Transmission electron microscopy for materials science; 2019. Available from: https://www.coursera.org/learn/microscopy/home/info.

[81] Reimer L. In: Transmission electron microscopy: physics of image formation and microanalysis. vol. 36. Springer; 2013. p. 21.

[82] www numis northwestern edu. Z-contrast STEM Config. http://www.numis.northwestern.edu/;. Accessed: 18-12-2023. Available from: http://www.numis.northwestern.edu/360/Notes/STEM_2023.pdf.

[83] Kirkland EJ. In: Advanced Computing in Electron Microscopy. Springer Nature; 2020. p. 9-36, 81-98, 143-95.

[84] Super-STEM website;. Accessed:2022-12-11. Available from: https://www.superstem.org/.

[85] Tey CM. Advanced transmission electron microscopy studies of III-V semiconductor nanostructures.; 2006.

[86] Pennycook S, Nellist P. Z-contrast scanning transmission electron microscopy. Impact of electron and scanning probe microscopy on materials research. 1999:161-207.

[87] Yacamán MJ, Santiago U, Mejía-Rosales S. In: Deepak FL, Mayoral A, Arenal R, editors. Aberration-Corrected Electron Microscopy of Nanoparticles. Cham: Springer International Publishing; 2015. p. 1-29.

[88] Watanabe K. Chapter 5. In: Theory for HAADF-STEM and its Image Simulation. World Scientific; 2014. p. 179-216.

[89] A Muller D, Edwards B, J Kirkland E, Silcox J. Simulation of thermal diffuse scattering including a detailed phonon dispersion curve. Ultramicroscopy. 2001;86(3):371-80.

[90] Brydson R. In: Aberration-corrected analytical transmission electron microscopy. Wiley Online Library; 2011. p. 8, 55-87, 271.

[91] Grillo V. Quantitative evaluation of strain effects in STEM HAADF contrast. Microscopie. 2009 3;11:61-8.

[92] Saitoh K. Appendice 9. In: Frozen Phonon Method for TDS Calculation in STEM Image Simulation. World Scientific; 2014. p. 531-41.

[93] Right triangle definition - Math Open Reference;. Accessed: 29-08-2022. Available from: `https://www.mathopenref.com/righttriangle.html`.

[94] Kröger R. Nanocarver; (2020). Email: roland.kroger@york.ac.uk.

[95] Vajdi M, Moghanlou FS, Sharifianjazi F, Asl MS, Shokouhimehr M. A review on the Comsol Multiphysics studies of heat transfer in advanced ceramics. Journal of Composites and Compounds. 2020;2(2):35-43.

[96] The Solid Mechanics Interface;. Accessed: 21-07-2022. Available from: `https://doc.comsol.com/5.5/doc/com.comsol.help.sme/sme_ug_solid.07.02.html`.

[97] COMSOL. Finite Element Method; 2016. Accessed: 06-08-2023. Available from: https://www.comsol.com/multiphysics/finite-element-method?parent=physics-pdes-numerical-042-62.

[98] Stationary;. Accessed: 21-07-2022. Available from: https://doc.comsol.com/5.5/doc/com.comsol.help.comsol/comsol_ref_solver.27.015.html#1432247.

[99] Li SX, Ren DB, Jia WP, Chen CR, Li XW, Wang ZG. On the stress distribution around a triple junction. Philosophical Magazine A. 2000 8;80:1729-41.

[100] Chicot D, Mendoza J, Zaoui A, Louis G, Lepingle V, Roudet F, et al. Mechanical properties of magnetite (Fe3O4), hematite (α-Fe2O3) and goethite (α-FeO·OH) by instrumented indentation and molecular dynamics analysis. Materials Chemistry and Physics. 2011;129:862-70.

[101] COMSOL. Prescribed Displacement;. Accessed: 18-07-2022. Available from: https://doc.comsol.com/5.5/doc/com.comsol.help.sme/sme_ug_solid.07.47.html.

[102] COMSOL. Deformation Measures;. Accessed: 2022-01-31. Available from: https://doc.comsol.com/5.5/doc/com.comsol.help.sme/sme_ug_theory.06.08.html.

[103] Kittel C, McEuen P. Introduction to Solid State Physics. 8th ed. John Wiley & Sons;.

[104] Interpolate 2-D or 3-D scattered data - MATLAB - MathWorks United Kingdom;. Available from: https://uk.mathworks.com/help/matlab/ref/scatteredinterpolant.html.

[105] Viking - University of York Research Computing Cluster - Research Computing Support - York Wiki Service;. Accessed: 18-12-2023. Available from: https://www.york.ac.uk/it-services/services/viking-computing-cluster/.

[106] York JEOL Nanocentre - York JEOL Nanocentre, University of York;. Available from: https://www.york.ac.uk/nanocentre/.

[107] Yao Y. Thermal diffuse scattering: elastic and coherent. arXiv preprint arXiv:230103430. 2023.

[108] Wang HB, Ma F, Li QQ, Dong CZ, Ma DY, Wang HT, et al. Synthesis and stress relaxation of ZnO/Al-doped ZnO core–shell nanowires. Nanoscale. 2013;5:2857-63.

[109] Scarisoreanu ND, Craciun F, Birjega R, Ion V, Teodorescu VS, Ghica C, et al. Joining Chemical Pressure and Epitaxial Strain to Yield Y-doped BiFeO3 Thin Films with High Dielectric Response. Scientific Reports. 2016 May;6(1):25535.

[110] www purdue edu. General State of Stress and Strain; 2023. Accessed: 19-09-2022. Available from: https://www.purdue.edu/freeform/me323/animations-and-demonstrations/general-state-of-stress-and-strain/.

[111] Zheng CL, Etheridge J. Measurement of chromatic aberration in STEM and SCEM by coherent convergent beam electron diffraction. Ultramicroscopy. 2013;125:49-58.

[112] Gonzalez RC, Woods RE, Eddins SL. In: Digital Image Processing Using MATLAB. 2nd ed. Gatesmark Publishing;. p. 1-12.

[113] Leis J. In: Digital signal processing using MATLAB for students and researchers. Wiley Online Library; 2011. p. 203-69.

[114] Kirkland EJ. Image simulation in transmission electron microscopy. Cornell University, Ithaca, NY, USA. 2006:1-14.

[115] Stadelmann P. Introduction to HRTEM image simulation;. Accessed: 2021-04-21. Available from: https://www.jems-swiss.ch/Home/Docs/PDF/IntroImageSimulation.pdf.

[116] Pirmin K. Quantitative Scanning Transmission Electron Microscopy for III-V Semiconductor Heterostructures Utilizing Multi-Slice Image Simulations. Philipps-Universität Marburg; 2019.